

DISSERTATION  
SUBMITTED TO THE  
COMBINED FACULTIES OF THE NATURAL SCIENCES AND  
MATHEMATICS  
OF THE RUPERTO-CAROLA-UNIVERSITY OF HEIDELBERG, GERMANY  
FOR THE DEGREE OF  
DOCTOR OF NATURAL SCIENCES

PUT FORWARD BY

MASTER PHYS. ANA LUCÍA URIBE URIBE  
BORN IN: BOGOTÁ (COLOMBIA)

ORAL EXAMINATION: FEBRUARY 1st, 2012



---

## Zusammenfassung

Die Doktorarbeit präsentiert eine numerische Studie zur Wechselwirkung zwischen Planeten und zirkumstellaren Scheiben. Wir benutzen den hydrodynamischen/magneto-hydrodynamischen Code PLUTO (Mignone et al., 2007) zur Simulation von zirkumstellaren Akkretionsscheiben. Ein Modul zur Beschreibung des Planeten wurde in den Code eingebaut. Wir untersuchen zwei entscheidende Aspekte in der Theorie der Planetenentstehung: die Migration von Planeten aufgrund des Gravitationstorque der Scheibe und die Akkretion von Gas der umliegenden Scheibe auf die Planeten. Zuerst untersuchen wir diese Gesichtspunkte für massereiche Planeten ( $M_p \approx M_{Jup}$ ) in der Entwicklungsphase einer Gaslücke in der Scheibe. Sobald die Gaslücke erzeugt wird ( $\Sigma_{gap} < 0.1\Sigma_0$ ), findet man eine lineare Abhängigkeit zwischen der Oberflächendichte innerhalb der Gaslücke und der Migration und Gasakkretionsrate. Der Torque welcher auf den Planeten wirkt, hängt stark von dem Material innerhalb der Hill-Sphäre ab sobald die lokale Scheibenmasse die Planetenmasse übersteigt. Die Entleerung der Hill-Sphäre aufgrund eines akkretierenden Planeten kann die Migrationszeitskala aus der linearen Abschätzung bis zu einer Größenordnung erhöhen. Zweitens untersuchen wir die Migration und Gasakkretion in turbulenten Scheiben, generiert von der Magneto-Rotations Instabilität (MRI). In schwach magnetisierten turbulenten Scheiben dominiert die Migration von Planeten mit geringer Masse durch stochastische Dichtefluktuationen welche mithilfe einer gegebenen Amplitude und Korrelationszeit charakterisiert werden kann. Aufgrund der Ungesättigtheit des Korotationstorque von der turbulenten Advektion und Diffusion des Gases in der "horseshoe" Region können schwerere Planeten eine langsamere oder sogar eine umgekehrte Migration erfahren. Die magnetische Turbulenz ist im Falle von Riesenplaneten, welche eine Gaslücke öffnen, stark unterdrückt. Zusätzlich akkretieren Planeten mit Jupitermasse in turbulenten Scheiben weniger als vom global-gemittelten internen Stress in der Scheibe erwartet wird. Unsere Ergebnisse können direkt in ein Planeten-Populations Model eingebaut werden um die Eigenschaften der beobachteten Populationen von extrasolaren Planeten besser zu verstehen.

## Abstract

This thesis presents a numerical study on the interaction between planets and circumstellar disks. We use the hydrodynamics/magnetohydrodynamics code PLUTO (Mignone et al., 2007) to simulate the circumstellar accretion disk. A module to include embedded planets was incorporated into the code. We study two critical aspects for planet formation theory: the migration of planets due to gravitational disk torques and the accretion of gas onto planets from the surrounding disk. These two aspects are critical in any planet formation model as they will determine the final mass and the orbital separation. We first investigate these aspects for massive planets ( $M_p \approx M_{Jup}$ ) in the evolutionary phase when a gap has been cleared in the disk. It is found that when a gap has been opened ( $\Sigma_{gap} < 0.1\Sigma_0$ ), the migration and gas accretion rate is linearly dependent on the surface density inside the gap. The torques exerted on the planet depend strongly on the material inside the Hill sphere when the local disk mass exceeds the planet mass. The depletion of the Hill sphere due to an accreting planet can increase migration timescales up to an order of magnitude of the linear estimate. Secondly, we investigate migration and gas accretion in turbulent disks, where the turbulence is generated by the magneto-rotational instability (MRI). In weakly magnetized and turbulent disks, low-mass planet migration is dominated by stochastic density perturbations that can be characterized with a given amplitude and correlation time. More massive planets can undergo slower or reversed migration due to the unsaturation of the corotation torque by turbulent advection and diffusion of gas into the horseshoe region. Magnetic turbulence is greatly suppressed by giant planets that open a gap in the disk. Additionally, Jupiter-mass planets in turbulent disks are found to accrete less than expected from the global-averaged internal stresses in the disk. Our results can be directly implemented in planet population synthesis studies in order to better understand the nature of the observed population of extrasolar planets.



*Para mis padres.*

---

# Contents

<b>List of Figures</b>	<b>vii</b>
<b>List of Tables</b>	<b>xiii</b>
<b>1 Introduction</b>	<b>1</b>
1.1 Context . . . . .	1
1.2 Planet formation and evolution: concepts, theory and simulations . . . . .	2
1.3 About this thesis . . . . .	8
<b>2 Planet-disk gravitational interactions</b>	<b>11</b>
2.1 Migration Regimes . . . . .	12
2.1.1 Type I: Low-mass planet migration . . . . .	12
2.1.2 Type II: Gap-opening planets . . . . .	13
2.1.3 Type III: Intermediate cases . . . . .	14
2.2 Migration in non-isothermal disks . . . . .	14
2.3 Corotation Torques . . . . .	15
<b>3 Type II migration and gas accretion onto planets in disks with uniform constant mass accretion</b>	<b>17</b>
3.1 Introduction . . . . .	18
3.2 Gap opening and type II migration . . . . .	19
3.3 Description of the setup of the simulations . . . . .	20
3.3.1 Disk profile and planet setup . . . . .	21
3.3.1.1 Parameters of the simulations . . . . .	22
3.3.2 Test of the viscous evolution of the disk . . . . .	22
3.4 Results . . . . .	22
3.4.1 Dependence of migration on surface density . . . . .	22
3.4.1.1 Fixed orbit planet . . . . .	23
3.4.1.2 Free moving planet: Effect of the Hill sphere . . . . .	24
3.4.2 Dependence of migration on the power law exponent . . . . .	26

## CONTENTS

---

3.4.3	Dependence of migration on disk viscosity . . . . .	27
3.4.4	Accretion of gas onto planets . . . . .	28
3.4.5	Mass flow through gaps . . . . .	30
3.5	Discussion and conclusions . . . . .	32
<b>4</b>	<b>3D MHD Simulations of Planet Migration in Turbulent Stratified Disks</b>	<b>37</b>
4.1	Introduction . . . . .	38
4.2	Simulation Setup . . . . .	40
4.2.1	Disk and Planet Models . . . . .	41
4.2.2	Magnetic Field Configuration . . . . .	42
4.2.2.1	Zonal flows and pressure bumps . . . . .	43
4.3	Results . . . . .	44
4.3.1	Disk torques and migration . . . . .	44
4.3.1.1	Low Mass Planets ( $q = 5 \times 10^{-6}$ and $q = 1 \times 10^{-5}$ ) . . . . .	45
4.3.1.2	Intermediate Mass Planets ( $q = 5 \times 10^{-5}$ , $q = 1 \times 10^{-4}$ and $q = 2 \times 10^{-4}$ ) . . . . .	47
4.3.1.3	Large Mass Planet ( $q = 10^{-3}$ ) . . . . .	52
4.4	Discussion and conclusions . . . . .	54
4.5	Summary . . . . .	60
<b>5</b>	<b>Accretion of gas onto giant planets and envelope structure in magnetized turbulent disks</b>	<b>63</b>
5.1	Introduction . . . . .	64
5.1.1	Modeling planet accretion . . . . .	64
5.2	Computational setup . . . . .	66
5.2.1	Boundary conditions . . . . .	67
5.2.2	Initial conditions, gap opening and viscosity . . . . .	67
5.2.3	Accretion prescription . . . . .	67
5.3	Results . . . . .	69
5.3.1	Structure of the envelope and mass inflow . . . . .	69
5.3.2	Gas accretion rates . . . . .	69
5.3.3	Gas inflow and magnetic pressure . . . . .	72
5.4	Discussion and conclusions . . . . .	75
5.5	Summary . . . . .	77
<b>6</b>	<b>Conclusions</b>	<b>79</b>
6.1	Future research . . . . .	81
<b>A</b>	<b>Stochastic gravitational torque on low-mass planets</b>	<b>83</b>

Bibliography

87

## CONTENTS

---

# List of Figures

1.1	Minimum mass vs. orbital period of exoplanets. The color represents the orbital eccentricity of the planets. [Figure produced with the exoplanets.org plotter]	3
1.2	Left: Disk fraction (as JKHL excess) vs. mean age for seven young clusters [figure taken from Haisch et al. (2001)]. On average, half of the disks are gone after 3 Myr. Right: Inwards migration timescale vs. planet mass [figure taken from Bate et al. (2003)]. Analytical estimates for Type I and II migration are overplotted. Planets more massive than $0.01M_{Jup}$ migrate their initial semi-major axis distance in less than 1 Myr.	9
3.1	Disk mass accretion rate measured in the simulations. The analytical estimate $\dot{M} = -3\pi\Sigma\nu$ is shown in the dashed line.	23
3.2	Cumulative average torques on the planet for varying surface density (where $\Sigma=\Sigma_0$ ) for $\epsilon = 0.3$ (left) and $\epsilon = 0.06$ (right). From dark to light curves, $\Sigma_0 = 5 \times 10^{-6}, 1 \times 10^{-5}, 5 \times 10^{-5}, 1 \times 10^{-4}, 5 \times 10^{-4}, 1 \times 10^{-3}$ and $3 \times 10^{-3}$ , respectively. This corresponds to $B = (\pi r_p^2)\Sigma/M_p = 0.017, 0.035, 0.17, 0.35, 1.76, 3.53$ and $10.6$ .	24
3.3	Surface density after 500 orbits for $\epsilon = 0.3$ (left) and $\epsilon = 0.06$ (right). Initial densities are $\Sigma_0 = 5 \times 10^{-6}, 1 \times 10^{-5}, 5 \times 10^{-5}, 1 \times 10^{-4}, 5 \times 10^{-4}, 1 \times 10^{-3}$ and $3 \times 10^{-3}$ .	25
3.4	Density after 500 orbits for $\epsilon = 0.3$ (left) and $\epsilon = 0.06$ (right). The initial density is $\Sigma_0 = 5 \times 10^{-4}$ for both cases.	26
3.5	Dependence of the cumulative average torque on the $B = (\pi r_p^2\Sigma)/M_p$ parameter (where $\Sigma=\Sigma_0$ ) for $\epsilon = 0.3$ (left) and $\epsilon = 0.06$ (right). The dashed line shows the analytical expression $\Gamma = -(3/4)\nu_0\Omega_p$ (Eq. 3.4). The dash-dotted line shows the analytical expression $\Gamma = -(3/2\pi)\nu_0\Omega_p B$ (Eq. 3.6).	27

## LIST OF FIGURES

---

- 3.6 Cumulative average torques on the planet for varying surface density, excluding (left) and including (right) the contribution of the Hill sphere on the orbital evolution. From dark to light curves,  $\Sigma_0 = 5 \times 10^{-6}, 1 \times 10^{-5}, 5 \times 10^{-5}, 1 \times 10^{-4}, 5 \times 10^{-4}, 1 \times 10^{-3}$  and  $3 \times 10^{-3}$ , respectively. This corresponds to  $B = (\pi r_p^2) \Sigma / M_p = 0.017, 0.035, 0.17, 0.35, 1.76, 3.53$  and  $10.6$ . . . . . 28
- 3.7 Planet position for varying surface density, excluding (left) and including (right) the contribution of the Hill sphere on the orbital evolution. From dark to light curves,  $\Sigma_0 = 5 \times 10^{-6}, 1 \times 10^{-5}, 5 \times 10^{-5}, 1 \times 10^{-4}, 5 \times 10^{-4}, 1 \times 10^{-3}$  and  $3 \times 10^{-3}$ , respectively. This corresponds to  $B = (\pi r_p^2) \Sigma / M_p = 0.017, 0.035, 0.17, 0.35, 1.76, 3.53$  and  $10.6$ . . . . . 29
- 3.8 Dependence of the cumulative average torque on the  $B = (\pi r_p^2 \Sigma) / M_p$  parameter, excluding (left) and including (right) the contribution of the Hill sphere on the orbital evolution. The dashed line shows the analytical expression  $\Gamma = -(3/4)\nu_0\Omega_p$  (Eq. 3.4). The dash-dotted line shows the analytical expression  $\Gamma = -(3/2\pi)\nu_0\Omega_p B$  (Eq. 3.6). . . . . 30
- 3.9 Left: Dependence of the cumulative average torque (taking last value at 1500 orbital periods) on the surface density exponent  $a$  parameter (where  $\Sigma = \Sigma_0 r^{-a}$  and  $\nu = \nu_0 r^a$ ), for two different values of the surface density constant  $\Sigma_0$ . Right: Surface density after 1500 orbital periods of the planet for each profile. . . . . 31
- 3.10 Left: Cumulative average torques on the planet for varying viscosity ( $\nu = 1 \times 10^{-6}, 1 \times 10^{-5}, 1 \times 10^{-4}$  and  $1 \times 10^{-3}$ ). Right: Torques vs kinematic viscosity  $\nu$ . . . . . 32
- 3.11 Left: Accretion rate of gas onto the planet for different disk surface densities. Right: Cumulative mass accreted by the planet. From dark to light curves,  $\Sigma_0 = 5 \times 10^{-6}, 1 \times 10^{-5}, 5 \times 10^{-5}, 1 \times 10^{-4}, 5 \times 10^{-4}, 1 \times 10^{-3}$  and  $3 \times 10^{-3}$ , respectively. . . . . 33
- 3.12 Accretion rates onto the planet as a function of surface density. . . . . 33
- 3.13 Left: Cumulative torques vs time for different densities. From dark to light curves,  $\Sigma_0 = 5 \times 10^{-6}, 1 \times 10^{-5}, 5 \times 10^{-5}, 1 \times 10^{-4}, 5 \times 10^{-4}, 1 \times 10^{-3}$  and  $3 \times 10^{-3}$ , respectively. Right: Dependence of the cumulative average torque on the  $B = (\pi r_p^2 \Sigma) / M_p$  parameter for an accreting planet. The dashed line shows the analytical expression  $\Gamma = -(3/4)\nu_0\Omega_p$  (Eq. 3.4). The dash-dotted line shows the analytical expression  $\Gamma = -(3/2\pi)\nu_0\Omega_p B$  (Eq. 3.6). . . . . 34

---

LIST OF FIGURES

3.14	Mass flux $\rho(r_p)v_r(r_p)$ , averaged in time and in the azimuthal direction at the position of the planet. The mass flux is shown for simulations with a fixed orbit planet ( <i>stars</i> ), a free moving planet ( <i>diamonds</i> ) and a free moving and accreting planet ( <i>crosses</i> ). The blue symbols denote positive values of the mass flux. . . . .	35
4.1	Initial radial distribution of the time, azimuthally and vertically averaged stress parameter (before the addition of the potential of the planet). The dashed and dashed-dot lines show the Reynolds $T_{Rey}$ and Maxwell $T_{Max}$ stresses respectively, normalized by the initial pressure. The solid line shows the total effective $\alpha$ parameter. . . . .	43
4.2	Time evolution of $B_\phi$ , $B^2/B_0^2$ and $\alpha$ for a run without a planet. The dashed and dashed-dotted lines show the Reynolds $T_{Rey}$ and Maxwell $T_{Max}$ stresses respectively, normalized to the initial pressure. The solid line shows the total effective $\alpha$ parameter. . . . .	44
4.3	<i>Top figure</i> : Time-averaged thermal and magnetic pressure in the mid-plane (black line) and one scale height above the mid-plane (red line). The profiles have been normalized to take out the radial variation. <i>Bottom figure</i> : Azimuthal velocity perturbation (with respect to Keplerian speed) in the mid-plane (black line) and one scale height above the mid-plane (red line). This is from a simulation with no planet included. . . . .	45
4.4	Logarithm of the disk density in the mid plane (top row) and in an azimuthal cut at the position of the planet (bottom row) for runs R2 (left, $q = 10^{-5}$ ), R5 (middle, $q = 10^{-4}$ ) and R9 (right, $q = 10^{-3}$ ). . . . .	47
4.5	Cumulative average torque for run R1 for $q = 5 \times 10^{-6}$ . The red and blue lines show the torque exerted by the inner and outer disk respectively. . . .	48
4.6	Cumulative average torque for runs R2 and R3, for $q = 10^{-5}$ , where the planet is located at $r_p = 3.3$ and $r_p = 5.0$ respectively. The red and blue lines show the torque exerted by the inner and outer disk, respectively. . .	48
4.7	Power spectrum of the surface density, averaged in time and azimuthally, from MHD simulation ( <i>stars</i> ). We compare with the power spectrum that results from the turbulent model of <a href="#">Baruteau and Lin (2010)</a> used in HD simulations, with ( <i>triangles</i> ) and without ( <i>crosses</i> ) the cutoff of the modes with $m > 6$ , and with effective $\alpha \sim 10^{-3}$ . . . . .	49
4.8	Cumulative average torque for run R4 for $q = 5 \times 10^{-5}$ . The red and blue lines show the torque exerted by the inner and outer disk respectively. . . .	52
4.9	Cumulative average torque for runs R5 and R6, for $q = 10^{-4}$ , where the planet is located at $r_p = 3.3$ and $r_p = 5.0$ respectively. The red and blue lines show the torque exerted by the inner and outer disk, respectively. . .	53

## LIST OF FIGURES

---

4.10	Cumulative average torque for run R7 for $q = 10^{-4}$ , for the planet located at $r_p = 4.0$ , initially at the right side of a pressure bump. The red and blue lines show the torque exerted by the inner and outer disk respectively. . . .	54
4.11	Cumulative average torque for run R8 for $q = 2 \times 10^{-4}$ . The red and blue lines show the torque exerted by the inner and outer disk respectively. . . .	55
4.12	Surface density at different times in the simulation. Top, middle and bottom plot show the surface density for runs R2, R5 and R9 respectively. The vertical lines shows the position of the planet and the extent of the Hill radius. . . . .	56
4.13	Time evolution of the stresses in a disk with an embedded planet. Top, middle and bottom plot show the stresses for runs R2, R5 and R9, respectively. The dashed and dashed-dotted lines show the Reynolds $T_{Rey}$ and Maxwell $T_{Max}$ stresses, respectively, normalized to the initial pressure. The solid line shows the total effective $\alpha$ parameter. . . . .	57
4.14	Cumulative average torque for run R9 for $q = 10^{-3}$ . The red and blue lines show the torque exerted by the inner and outer disk respectively. The torque coming from the Hill sphere has been excluded from the calculation.	58
4.15	Radial distribution of the time, azimuthally and vertically averaged stress parameter for run R9. The dashed and dashed-dot lines show the Reynolds $T_{Rey}$ and Maxwell $T_{Max}$ stresses respectively, normalized by the initial pressure. The solid line shows the total effective $\alpha$ parameter. . . . .	59
4.16	Gap comparison for run R9 ( $q = 10^{-3}$ ) and run 10, an equivalent HD simulation with $\alpha = 2 \times 10^{-3}$ . . . . .	60
4.17	Specific torque as a function of $q = M_p/M_s$ . The black symbols correspond to simulations R1, R2, R4, R5, R8 and R9, where the position of the planet is $r_p = 5.0$ . The red symbols correspond to simulations R3 and R6, where the position of the planet is $r_p = 3.3$ . In the $q = 5 \times 10^{-6}$ to $q = 2 \times 10^{-4}$ mass range, we overplot the analytical estimates for the torque, taking into account only the Lindblad contribution $\Gamma_{tot} = \Gamma_{Lind}$ (dotted line) and both the Lindblad plus the unsaturated horseshoe drag $\Gamma_{tot} = \Gamma_{Lind} + \Gamma_{HS}$ (dash-dotted line), for both positions (i.e. local surface density profiles) of the planet, $r_p = 5.0$ (black line) and $r_p = 3.3$ (red line). For the analytical expressions of the torque, we take the half-width of the horseshoe region to be 5% larger than its analytical estimate. The dashed line corresponds to the constant Type II migration rate, given by the viscous transport in the disk, using $\alpha = 2 \times 10^{-3}$ . Error bars represent the standard deviation of the torque time distribution. . . . .	61

---

**LIST OF FIGURES**

5.1	Initial conditions before the planet starts accreting for the laminar disk simulations and the MHD simulation. The gap in the MHD simulation is found to be wider as compared to all the viscous simulations. . . . .	68
5.2	Density in the surface of the Hill sphere for the viscous laminar runs with $\alpha = 2 \times 10^{-3}$ (left) and $\alpha = 2 \times 10^{-4}$ (right). The density is shown in units of $2 \times 10^{-10} \text{grcm}^{-3}$ . The center of the ellipse corresponds to the point in the Hill sphere that is most distant from the star and points away in the radial direction. . . . .	70
5.3	Density in the surface of the Hill sphere for the viscous laminar run with $\alpha = 2 \times 10^{-5}$ (left) and for the turbulent run(right). The density is shown in units of $2 \times 10^{-10} \text{grcm}^{-3}$ . The center of the ellipse corresponds to the point in the Hill sphere that is most distant from the star and points away in the radial direction. . . . .	70
5.4	Mass flux through the surface of the Hill sphere for the viscous laminar runs with $\alpha = 2 \times 10^{-3}$ (left) and $\alpha = 2 \times 10^{-4}$ (right). The mass flux is given in units of $M_{Jyr}^{-1}S^{-1}$ , where quantity $S$ is the area of the grid cell given by $S = r_h^2 \Delta\theta_{RH} \Delta\phi_{RH}$ . The center of the ellipse corresponds to the point in the Hill sphere that is most distant from the star and points away in the radial direction. . . . .	71
5.5	Mass flux through the surface of the Hill sphere for $\alpha = 2 \times 10^{-5}$ (left) and for the turbulent run(right). The mass flux is given in units of $M_{Jyr}^{-1}S^{-1}$ , where quantity $S$ is the area of the grid cell given by $S = r_h^2 \Delta\theta_{RH} \Delta\phi_{RH}$ . The center of the ellipse corresponds to the point in the Hill sphere that is most distant from the star and points away in the radial direction. . . . .	71
5.6	Vertical structure of the mass inflow $\rho v_{inflow}$ into the Hill sphere. The coordinate $\theta_{RH}$ refers to the polar angle in the frame of the planet. The quantity $\rho v_{inflow}$ has been azimuthally averaged (with respect to the Hill sphere). The quantity $S$ is the area of the grid cell given by $S = r_h^2 \Delta\theta_{RH} \Delta\phi_{RH}$ . . . . .	72
5.7	Mass accretion rate for the three viscous simulations and the magnetized simulation. The red line corresponds to $\alpha = 2 \times 10^{-5}$ , green line to $\alpha = 2 \times 10^{-4}$ , and black line to $\alpha = 2 \times 10^{-3}$ . The yellow line shows the MHD case. The colored dashed lines show the mean value of each simulation. . . . .	73
5.8	Cumulative mass accreted by the planet for the three viscous simulations and the magnetized simulation. The solid line corresponds to $\alpha = 2 \times 10^{-3}$ , dotted line to $\alpha = 2 \times 10^{-4}$ , and dashed line to $\alpha = 2 \times 10^{-5}$ . The dash-dotted line shows the MHD case. . . . .	74
5.9	Left: Radial mass flux for the different runs. Right: Pressure for the different runs. The dashed line shows the magnetic pressure (multiplied by a factor of 150) for the magnetized case. . . . .	75

**LIST OF FIGURES**

---

5.10 Left: Density (in units of  $10^{-12}grcm^{-3}$ ) in the mid-plane for the laminar viscous simulation with  $\alpha = 2 \times 10^{-3}$ . Right: Radial velocity (in units of  $v_k(1AU)$ ) in the mid-plane for the same simulation. The overplotted vector field shows the velocity field in the mid-plane. . . . . 75

5.11 Left: Density (in units of  $10^{-12}grcm^{-3}$ ) in the mid-plane for the MHD simulation. Right: Radial velocity (in units of  $v_k(1AU)$ ) in the mid-plane for the MHD simulation. The overplotted vector field shows the velocity field in the mid-plane. . . . . 76

5.12 Magnetic pressure in the mid-plane for the MHD simulation. The overplotted vector field shows the velocity field in the mid-plane. . . . . 76

5.13 Mass accretion rates by the planet for different values of  $\alpha$ (crosses) and the turbulent run (square and dotted line). The diamond symbols show the accretion rate  $\dot{M} = 3\pi\nu\Sigma$  calculated using the unperturbed density, while the triangle symbols show the accretion rate calculated using the mean density inside the gap region. . . . . 78

A.1 Left: Semi-major axis vs time for 50 massless particles (position signaled by color). Right: Fractional change in semi-major axis vs time. Particles undergo a diffusion process in small scales. . . . . 85

A.2 Left: Cumulative torque on the 50 massless particles. Right: Histogram of the cumulative torque at the end of the simulation (after 150 orbits). . . . 85

# List of Tables

3.1	Simulations parameters and measured gas accretion rates onto the planet. .	30
4.1	Simulation Parameters . . . . .	42

## LIST OF TABLES

---

# 1

## Introduction

### 1.1 Context

The natural history of the earth and the origin and formation of our solar system are two of the most fundamental scientific questions of modern times. Tremendous progress and understanding has been achieved in this field in the last century. Improbable and incorrect theories of solar system formation have given way to a mature and comprehensive theory of planet formation by accretion of solid material and eventually gas, in a circumstellar disk of gas and dust revolving around an early accreting Sun.

The field of planet formation, which has had its main focus on the solar system, has become much more exciting and complex, as hundreds of new planetary systems were discovered in the last decade, and new ones are constantly being added to the list (see Figure 1.1). Preconceived ideas were challenged with the great diversity of systems observed, with the discovery of Jupiter mass planets closer to their parent star than Mercury is to the Sun, of tightly packed multi-planet systems, of free-floating giant planets, of bloated giants and super Earths. Focus shifted to a theory of planet formation that is capable of explaining such diversity, and why the solar system is similar, or why it differs from other planetary systems.

Any theory that attempts to explain the observed diversity in systems has to include many different elements such as the possibility of gaseous planet formation by gravitational instability in the outer parts of massive disks, or the excitation of eccentricity and inclination of close-in planets in systems with an outer massive companion due to the Kozai mechanism, or a history of planet migration that produces Jupiter-mass planets at small separations. These elements might not have been all present in the formation of the solar system, but they have become much more relevant in explaining a great number of the observed extrasolar planets.

Ultimately, a comprehensive theory of planet formation must be linked to stellar formation

## 1. INTRODUCTION

---

history and must be able to explain features of individual systems as well as general population characteristics, where diversity in outcome results from a diversity in initial conditions.

While currently the general structure of such a theory is in place, focus has shifted from the idea of a grand theory, to explaining and describing in detail the multiple processes involved in the formation of planetary systems. There are many unresolved key issues along the way, due to the complexity and scales involved. These include the centimeter and meter barrier to planetesimal formation, the fast inwards migration of planets, the source of accretion in disks, and the size distribution and composition of dust grains, among others. It is not theoretically or computationally feasible to form a planetary system from beginning to end, although methods like planet population synthesis are capable of gathering a number of elements, and study the interplay of these and the evolution of planetary systems during Gyrs timescales. Additionally, global three-dimensional numerical simulations of protoplanetary disks have reached unprecedented resolutions, making it possible to elucidate the nature of important non-linear processes and instabilities that might be present in disks, such as the baroclinic instability, the well studied magneto-rotational instability, or the nature of planet-disk interactions.

### 1.2 Planet formation and evolution: concepts, theory and simulations

Early theories of solar system formation considered many different scenarios. One branch of early theories postulated a disjunct formation of the Sun and the planets (Jeans, 1931). In this branch, the Sun was proposed to be formed and established in its current main sequence state before the formation of the planets (Lissauer, 1993; Ter Haar, 1967; Williams and Cremin, 1968).

One possibility was the formation of the planets out of solid and gas material ejected from the Sun as a result of a perturbation by a near-by passing star (Chamberlin, 1901; Jeans, 1931; Jeffreys and Moulton, 1929; Moulton, 1905). The ejected solid material was called planetesimals and is the origin of the terminology used currently. Filaments of stellar material would be tidally formed around the Sun, followed by the condensation of the filaments into the planets at different separations from the Sun. This theory was later discarded when it was demonstrated that the terrestrial planets were not massive enough to condense out of filament material, and the timescales for formation of the giant planets were of the order the lifetime of the solar system, due to very large cooling timescales (Lyttleton, 1940; Nölke, 1932; Spitzer, 1939).

Another possibility was the formation of the planets out of a captured interstellar cloud by the Sun, that later condensed into planets (Berlage, 1968). The cloud was a priori

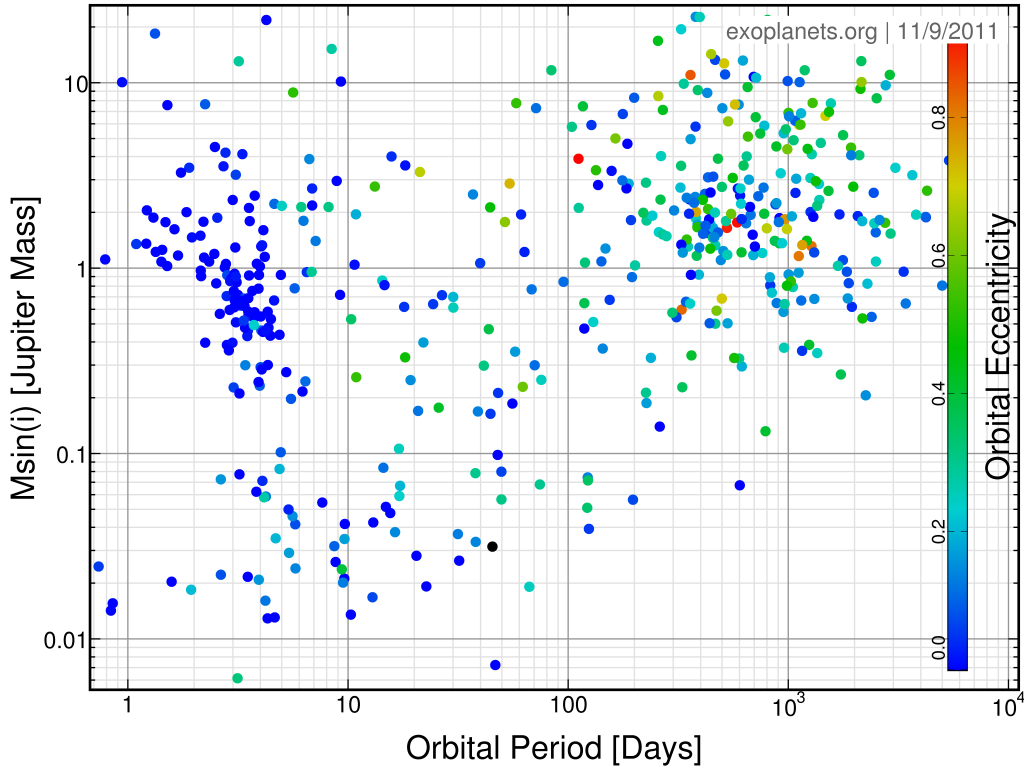


**Figure 1.1:** Minimum mass vs. orbital period of exoplanets. The color represents the orbital eccentricity of the planets. [Figure produced with the exoplanets.org plotter]

assumed to have the right angular momentum to match the solar system distribution and it would form ringed structures as a result of dissipative processes, which would later condense into planets. The rings were also predicted to be distributed according to the Titus-Bode law. The difference in composition was attributed solely to the difference in temperature in the nebula. In the inner hotter regions only non-volatile material could condense, forming the terrestrial planets (Ter Haar, 1948, 1950).

Theories of cloud capture were later abandoned as the problem of the angular momentum distribution of the solar system remained unsolved. No mechanism was provided to remove angular momentum from the Sun, and the angular momentum distribution was always imposed as an initial condition in the cloud, rather than being a result of physical evolution. Additionally, condensation timescales of the planets by gravitational instability seemed comparable to the lifetime of the solar system.

Theories where the Sun co-formed with the planets effectively out of the same interstellar material slowly gained more acceptance and popularity. Circumstellar disks were recognized as natural by-products of the formation of stars out of the collapse of a rotating molecular cloud and conservation of angular momentum (Cameron, 1962; Hoyle, 1960;

## 1. INTRODUCTION

---

Terebey et al., 1984). The excess of infrared luminosity in the spectra of low-mass stars was attributed to heated circumstellar material (dust grains) emitting thermal reprocessed stellar light (Geisel, 1970; Lada and Adams, 1992; Mendoza V., 1968). These young stellar objects represented the first stages of star formation. In the circumstellar envelope composed of gas and dust and arranged in a flattened disk structure, planetesimals and planets could form out of the solid material.

Edgeworth (1949) already postulated an accretion disk around the Sun, where angular momentum was carried away from the Sun by viscous processes, slowing down the rotation of the Sun. The source of viscosity was the boundary layer between disk material and the solar surface. However it was not clear if this provided enough viscosity to support accretion and carry the necessary amount of angular momentum outwards (Edgeworth, 1962).

With the possibility of grain growth by coagulation and competitive accretion (Baines and Williams, 1965; Donn and Sears, 1963), timescales for terrestrial planet formation decreased by orders of magnitude, as compared to the case where condensation from a gas sub-cloud was assumed. The accretion of small particles and grains into a protoplanet with an atmosphere also allowed for the possibility of energy release by interaction with particles and of dispersal of light materials (McCrea and Williams, 1965).

The growth of dust particles into aggregates and macroscopic bodies, and their effect on disk properties has been studied extensively (Alexander, 2008; Birnstiel et al., 2010, 2011; Dullemond and Monnier, 2010; Güttler et al., 2010; Juhász et al., 2010; Williams and Cieza, 2011). Dust grows by collisional sticking into larger aggregates, that then become compactified (Dominik and Tielens, 1997). Evidence for grain growth in envelopes of young stellar objects can be seen in the change in shape of the spectral energy distribution at long wavelengths (millimeter and sub-millimeter) (Bouwman et al., 2008; Mannings and Emerson, 1994; Sicilia-Aguilar et al., 2007; Throop et al., 2001). This change is usually associated with an evolutionary sequence. However, other physical configurations in the disk, such as a steady state of growth and fragmentation due to turbulent stirring, can produce a constant supply of small and large grains in long timescales (millions of years) (Dullemond and Dominik, 2005; Schräpler and Henning, 2004; Weidenschilling, 1984). Turbulence and composition of the disk will critically affect the processing of heavy elements such as silicates, iron and PAHs, therefore affecting the optical properties in the disk (Bouwman et al., 2008; Henning and Meeus, 2009; Henning and Stognienko, 1996; Hughes and Armitage, 2010; Juhász et al., 2009). Dust growth will depend on factors such as sticking efficiency, relative velocities and electric charge. Growth is significantly hindered for charged grains (Okuzumi, 2009). Additionally, turbulence creates high relative velocities which disrupts aggregates due to collisional fragmentation (Brauer et al., 2008; Zsom et al., 2010).

Another possibility to form macroscopic bodies are gravitational instabilities of the sedi-

## 1.2 Planet formation and evolution: concepts, theory and simulations

---

mented mid-plane layer of dust (Schräpler and Henning, 2004). However, this requires an enhancement of solids with respect to cosmic values of factors of 2 to 10 (Youdin and Shu, 2002). Furthermore, radial drift has the effect of quickly depleting the disk of small dust particles, so that a fraction of the primordial material might be left for aggregation and planet formation (Brauer et al., 2008). These factors exemplify the many uncertainties and barriers that have yet to be overcome in order to fully understand the formation process of rocky and icy planets, or of the cores of gas planets.

The formation mechanism of the giant gaseous planets has been a subject of much debate. Models of giant planet formation by gravitational instability need a very massive disk that can cool effectively on timescales of a few local orbital periods (Boss, 1997; Durisen et al., 2007; Mayer et al., 2002; Rafikov, 2005). Additionally, the planet needs a large reservoir of gas that can only be provided by the outer parts of the disk. These factors make the formation of giant planets inside  $10AU$  very improbable. Close in planets may also be susceptible to tidal disruption by the star, depending on their mass (Wetherill, 1980). It is possible that gravitational instability can form planets in the outer parts of disks. Once a planet has formed out of an unstable clump of gas and dust, it can accrete solid material from the circumstellar disk. Solids can sediment inwards and form a rocky core (Boss, 1997).

In the inner parts of disks, gas giants can form as a result of core formation by planetesimal accretion followed by formation of the gas envelope by gas accretion. Using numerical simulations of core accretion and envelope evolution, Pollack et al. (1996) distinguished three phases in the formation of planets. A first phase marked by the fast accretion of solids onto a core until the feeding zone of the planet is mostly evacuated (Stevenson, 1982); a second phase where gas and solids accretion is low and constant; finally, a third phase where the core mass equals the envelope mass, the envelope contracts and runaway gas accretion proceeds (Mizuno, 1980). Migration of the planet might allow for an extension of the feeding zone, while gap formation might lead to a mass limit for gap opening planets (Alibert et al., 2005).

While planets form and evolve, mass flows from the accretion disk towards the star, bringing most of the mass into the central object, while depositing most of the angular momentum in the planets and outer parts of the disk. Keplerian disks have been found to be hydrodynamically -linearly and non-linearly- stable (Goldreich and Lynden-Bell, 1965; Papaloizou and Pringle, 1984, 1985), and hydrodynamic turbulence has been shown to be inefficient for mass transport at the required rates (Ji et al., 2006). The source of accretion in circumstellar disks is still not known, although there are different candidate instabilities that could generate turbulence in the disk given different conditions (e.g. the baroclinic instability (Klahr and Bodenheimer, 2003)).

The most promising at present is the magnetorotational instability (MRI): an instability of ionized Keplerian disks under the action of a weak magnetic field (Balbus and Hawley,

## 1. INTRODUCTION

---

1991, 1998). The MRI is active when the field is well coupled to the gas, so it requires a minimum degree of ionization. This makes the development of the instability dependent on factors like the distance from the star and from the mid-plane, the temperature and chemical composition, and external sources of ionization such as cosmic rays (Sano et al., 2000; Turner and Sano, 2008; Turner et al., 2007). The characteristics of the MRI-dead zone therefore depend on these factors. In general the upper layers and the outer parts of the disk will be MRI-active, therefore turbulent, while the mid-plane will remain stable (Dzyurkevich et al., 2010; Fleming and Stone, 2003; Machida et al., 2000).

The development of new numerical methods and codes (Mignone et al., 2007; Stone et al., 2008; Stone and Norman, 1992), along with access to supercomputers, has allowed an enormous amount of work to arise using numerical MHD simulations of magnetized disks. In particular, the linear growth and saturation level of the instability have been studied extensively (Davis et al., 2010; Fleming and Stone, 2003; Flock et al., 2011; Fromang and Papaloizou, 2007; Fromang et al., 2007; Guan et al., 2009; Hawley et al., 1995, 1996; Sano et al., 2004; Sharma et al., 2006; Stone et al., 1996; Stone and Pringle, 2001; Wardle, 1999), along with the characterization of the dead zone using resistive simulations that calculate a self-consistent ionization profile (Sano et al., 2000; Turner and Sano, 2008).

Of particular interest to planet formation are the studies on dust stirring above the mid-plane by turbulent eddies and high relative velocities that hinder coagulation (Johansen and Klahr, 2005; Turner et al., 2010, 2007). Also relevant is dust trapping in the edge of the dead zone that could provide a place for rapid particle accumulation (Dzyurkevich et al., 2010; Kretke and Lin, 2007). MHD structures in an MRI-turbulent flow can also increase the effectiveness of particle trapping in regions of over pressure (Johansen et al., 2006, 2007, 2009)

As cores are formed in these turbulent accretion disks, there is a point where the mass of the planet is large enough so that gravitational forces between the disk and the planet become important. The theory of periodical perturbations in disks (such as the potential of an orbiting planet) had been developed in the field of galaxy spiral arms long before it had its application in planet-disk interactions (Goldreich and Tremaine, 1979; Lin and Shu, 1966; Shu, 1970). The planet excites density waves in the disk that propagate away from itself. Due to gravitational torques exerted on the planet by the gas, the planet can move radially. The speed and direction of motion depend on the planet mass and on disk properties like the surface density and viscosity (Bate et al., 2003; Papaloizou and Lin, 1984; Tanaka et al., 2002; Ward, 1997). For standard disk parameters, migration leads to a fast reduction of the separation between planet and star (Tanaka et al., 2002). Planets comparable to Earth or more massive migrate inwards in timescales that are comparable to the disk lifetime (see Figure 1.2). However, many mechanisms have been put forward to prevent or slow down rapid inwards migration (Masset, 2002; Masset et al., 2006b; Paardekooper and Papaloizou, 2009a; Thommes and Murray, 2006).

## 1.2 Planet formation and evolution: concepts, theory and simulations

---

Models of planet formation processes were put to the test as hundreds of new extrasolar planets were discovered in the last decade (see Figure 1.1). The radial velocity method provided the first large population of discovered planets: close in massive giants that produce large RV signals in the spectra of the parent star, allowing for estimation of orbital parameters and a minimum value of the planet mass (Marcy et al., 2005; Santos et al., 2003; Udry and Santos, 2007). Giant planets were found to be common around stars with higher metallicities (for solar type stars)(Udry and Santos, 2007; Vauclair, 2004), suggesting a possible signature of a more efficient formation by core accretion (Johnson et al., 2010). Massive planets were found to clump at short separations, with periods around 3 days, pointing to a history of inwards migration and a common stopping mechanism close to the star, such as the stellar magnetosphere boundary or an inner cavity in the disk (Cumming et al., 1999; Udry et al., 2003). However, in-situ formation of close in planets has been found to be possible in some cases (Bodenheimer et al., 2000).

A big surprise was the large range of eccentricities in the population of exoplanets (see Figure 1.1). Contrary to the solar system, exoplanets were found to have a almost a full range of eccentricities, similar to the one found in stellar multiple systems (Shen and Turner, 2008; Udry and Santos, 2007). Planet-planet scattering has been proposed to explain highly eccentric planets, as it would dominate the dynamics after the gas is no longer present (since the gas tends to damp eccentricity) and therefore shape the final configuration of a system (Ford and Rasio, 2008). Small-period solid planets (rock plus ice) in close-in orbits are predicted to have low eccentricities due to tidal circularization (Jurić and Tremaine, 2008; Nagasawa et al., 2008; Rasio and Ford, 1996).

Another detection technique, the transit method, brings the possibility of obtaining the radius of the planet, by studying the dimming of the stellar brightness due to a planet passing in front of the star through the line of sight (Borucki and Summers, 1984). Together with the RV method, candidates can be confirmed and the mean density of the planet can be obtained with the mass and radius information. Hundreds of candidates have been found by the KEPLER (Koch et al., 1998) and COROT (Léger et al., 2009) space missions, which include many Neptune analogs and super earths, possibly in the habitable zone of their parent star (Batalha et al., 2011; Gilliland et al., 2010; Howard et al., 2010).

The transit of planets provides the unique opportunity to study the absorption spectra of the atmosphere of a planet or the presence of moons (Ballester et al., 2007; Charbonneau et al., 2005; Pont et al., 2008; Richardson et al., 2007). Additionally, the Rossiter-MacLaughlin effect (the displacement of the stellar spectral lines due to stellar rotation during a transit) makes it possible to obtain the inclination of the orbit of the transiting planet, a parameter that provides much insight into the formation mechanism (Fabrycky and Winn, 2009; Gaudi and Winn, 2007).

An interesting subset of the exoplanet population are the so called bloated giants, which

## 1. INTRODUCTION

---

are unusually high-up in the mass-radius diagram of planets; planet structure models predict smaller radii for planets of equivalent masses (Howard et al., 2010). Tidal heating has been proposed as the main inflating mechanism (Ibgui and Burrows, 2009; Miller et al., 2009; Ogilvie and Lin, 2004), although tidal effects are not sufficient for explaining the largest of the inflated planets (Leconte et al., 2010). Magnetic effects such as Ohmic dissipation could account for a fraction of the necessary thermal energy to produce the inflation in radius (Batygin and Stevenson, 2010).

Other planet detection methods like microlensing or direct imaging can detect planet in previously unexplored parts of the planetary mass-separation diagram, although with much lower yield compared to the RV or transit method. Microlensing is capable of finding very low-mass planets, but follow up and characterization are not possible (Beaulieu et al., 2006; Bennett and Rhie, 1996; Gould and Loeb, 1992; Mao and Paczynski, 1991). Direct imaging can detect large period, young planets in the infrared thermal light, although it is an extremely challenging method due to the typical contrast of over six orders of magnitude between the star and the planet (Angel, 1994; Kalas et al., 2005; Lafrenière et al., 2008; Thalmann et al., 2009). However, both of these methods provide interesting testing grounds for formation models in the outer parts of the disk, specially of planets formed by gravitational instability (Veras et al., 2009).

Making sense of the multitude of data of extrasolar planets and comparing to theoretical models is a difficult task. Planet population synthesis models combine observational constraints with theoretical elements to create synthetic populations of individual planets forming and evolving in individual disks with diverse initial conditions (Mordasini et al., 2009a). These simulations usually include disk evolution through evaporation, planet accretion of planetesimals and gas, planet migration, and an adapted stellar structure model for the planet core and atmosphere. Although planet population synthesis brings together the uncertainties of each of its elements, it is a powerful tool to understand the interplay of processes and timescales of formation. Population synthesis has been able to reproduce key elements of the observed planet population like the metallicity relation and the presence of close-in giants due to Type II migration. It has also shed light on runaway accretion processes and their relation to clumps in the mass distribution of exoplanets (Alibert et al., 2004; Benz et al., 2008; Ida and Lin, 2004; Mordasini et al., 2009b).

### 1.3 About this thesis

It can be inferred from the population of discovered exoplanets that many systems underwent migration in their evolutionary history. The fact that migration timescales are in general shorter or on the order of the disk mean lifetime presents a problem for the formation of planetary systems; in theory planet embryos would fall into the central star as

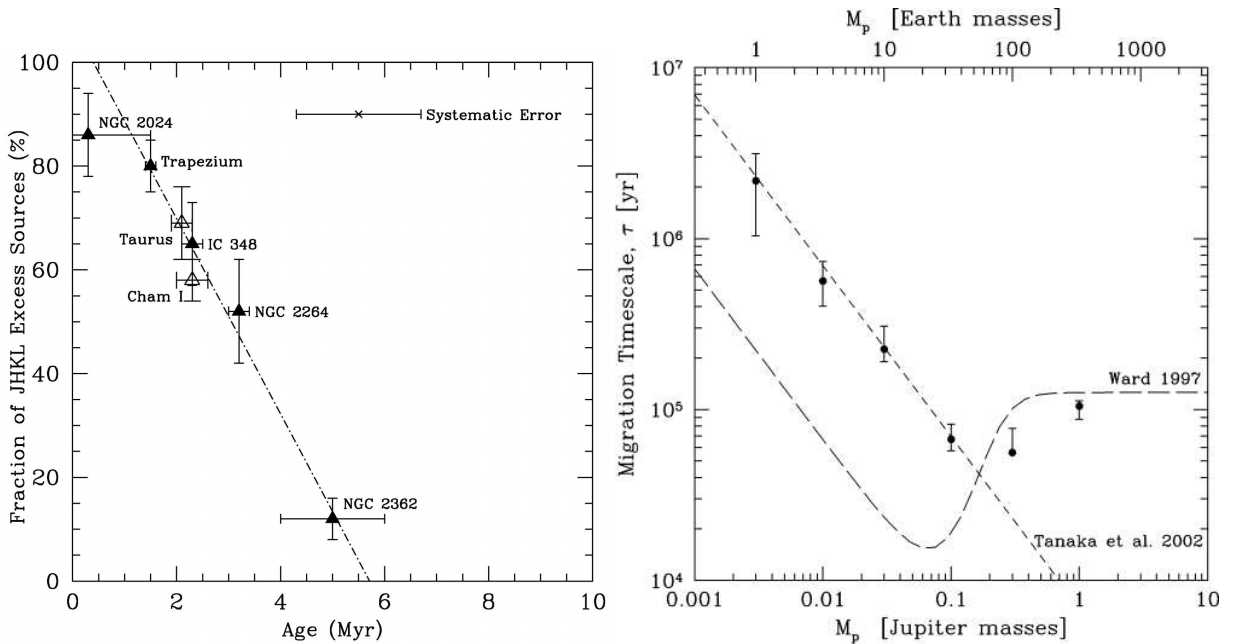


**Figure 1.2:** Left: Disk fraction (as JHKL excess) vs. mean age for seven young clusters [figure taken from Haisch et al. (2001)]. On average, half of the disks are gone after 3 Myr. Right: Inwards migration timescale vs. planet mass [figure taken from Bate et al. (2003)]. Analytical estimates for Type I and II migration are overplotted. Planets more massive than  $0.01M_{Jup}$  migrate their initial semi-major axis distance in less than 1 Myr.

long as there is enough gas present in the disk. However, we know that there are planets that survive migration and that the surviving systems are not only the lucky remaining embryos after the gas has disappeared. There must be different stopping mechanisms and a diversity in conditions in disks that prevents migration from being as effective as it was originally conceived.

The validity of the estimates for migration can only be tested indirectly through planet population synthesis models. In other words, population synthesis requires estimates of migration rates for a wide variety of planet/disk properties in order to be able to explain and predict the observed population of exoplanets. These migration estimates must come from theory and hydrodynamical simulations. It is equally important to have models of gas accretion by planets, as this is a fundamental parameter for modeling the formation of giant gaseous planets. Current planet population synthesis models have to reduce the Type I migration rates to 1% of the theoretical value in order to partially match observational results (Benz et al., 2008; Ida and Lin, 2008; Mordasini et al., 2009a,b). There is clearly a need to provide better estimates of migration rates.

In this thesis we present a numerical study of orbital migration and gas accretion onto planets embedded in protoplanetary disks. In Chapter 3, we focus on Type II migra-

## 1. INTRODUCTION

---

tion of gap opening planets. Similar studies have been performed to study the migration and gas accretion of gap opening planets. [Edgar \(2007\)](#) studied migration as a function of surface density and viscosity. However, no comparison with analytical estimates was done and they did not present the estimations of the torque as a function of the studied parameters. Additionally, their results overlap between the gap opening regime and partial gap opening. [Masset and Papaloizou \(2003\)](#) concentrated on studying runaway Type III migration, and covered a good range of the parameter space. We perform a dedicated study of Type II migration as a function of a variety of parameters and provide a comparison with analytical estimates. We also study the relation between migration and accretion onto planets, which is critical to obtain the correct migration rates. Our results are directly applicable to planet population synthesis models

In Chapters 4 and 5, we turn to the more complex problem of migration in turbulent disks. In most previous numerical and analytical studies, the disk turbulence is included as an effective viscosity. The disk, however, is technically laminar. One possibility that has been explored is modeling of the turbulence itself using a perturbing potential. In this case, the actual stochastic perturbations are reproduced in the density ([Adams and Bloch, 2009](#); [Baruteau and Lin, 2010](#); [Laughlin et al., 2004](#)). Simulations of turbulent disks where turbulence is generated by weak magnetic fields through the magneto-rotational instability (MRI) have been performed, under the approximation of a local shear flow, or a cylindrical geometry ([Nelson and Papaloizou, 2003, 2004](#); [Oishi et al., 2007](#); [Papaloizou and Nelson, 2003](#); [Papaloizou et al., 2004](#)).

We study migration in turbulent disks, with MRI-induced turbulence, in global stratified disk simulations. This is useful for two reasons. It provides a check for the previous simulations that have been performed with other approximations, and it provides parameters derived from "real" MHD turbulence that can be used in population synthesis models and semi-analytical models. We also study the accretion of gas onto giant planets in MRI-turbulent disks, which has never been studied in the literature before.

## 2

# Planet-disk gravitational interactions

Young planets orbiting around a star and embedded in a circumstellar disk will interact gravitationally with the gas and the dust present in the disk. The dust component is typically a small fraction (0.01) of the gas component, therefore the dynamics of migration can be understood in terms of the interaction between circumstellar gas and planet. The effect of the gas on the planet will be to change its separation to the star at a certain rate and direction, while the planet will modify the density in the disk linearly or non-linearly depending on the planet mass.

This process will depend on a number of factors: the gravitational torque exerted on the planet and the gas, the viscous diffusion in the disk, the thermal properties of the disk and the disk density structure. These factors in turn introduce relevant timescales which will determine the importance of each factor: the migration timescale  $\tau_{mig}$ , the viscous timescale  $\tau_\nu$ , the cooling timescale  $\tau_{cool}$ , the orbital timescale  $\tau_{orb}$  and finally the libration  $\tau_{lib}$  and U-turn timescales  $\tau_{uturn}$  associated with material near corotation <sup>1</sup>.

The evolution of the gas under the action of the planet is given by (neglecting magnetic fields and self-gravity and energy transport)

$$\frac{\partial \rho}{\partial t} - \nabla \cdot (\rho \mathbf{v}) = 0 \quad (2.1)$$

$$\frac{\partial \mathbf{v}}{\partial t} + (\mathbf{v} \cdot \nabla) \mathbf{v} = -\frac{1}{\rho} \nabla p - \nabla \Phi_p - \nabla \Phi_{star} + \mathbf{f}_\nu \quad (2.2)$$

$$(2.3)$$

where  $\Phi_p$  and  $\Phi_{star}$  are the planet and stellar gravitational potential respectively and  $\mathbf{f}_\nu$  is the viscous stress tensor. The gas pressure relates to the density through an equation of state  $p = p(\rho, T)$ . The stellar potential is given by  $\Phi_{star}(r) = -GM_{star}/r$ , while the

---

<sup>1</sup>All these being relevant within the gas disk lifetime

## 2. PLANET-DISK GRAVITATIONAL INTERACTIONS

---

planet potential is given by

$$\Phi_p(r) = -\frac{GM_p}{|\mathbf{r} - \mathbf{r}_p|}. \quad (2.4)$$

The torque exerted by the disk on the planet is determined at any moment in time by the detailed structure of the density resulting from solving system Eq 2.2, and is given by

$$\mathbf{\Gamma}(\mathbf{r}) = GM_p \int \rho(\mathbf{r}) \frac{\mathbf{r}_p \times \mathbf{r}}{|\mathbf{r} - \mathbf{r}_p|^3} dV. \quad (2.5)$$

Torque exerted on the planet leads to a change in angular momentum  $\mathbf{\Gamma} = d\mathbf{L}/dt$ . In particular, vertical torque leads to a change in orbital angular momentum  $\Gamma_z = dL_z/dt = d(M_p r_p v'_p)/dt$ , where  $v'_p$  is the velocity of the planet in the orbital plane, equal to the Keplerian speed  $v'_p = v_{Kep} = \sqrt{GM_p/r_p}$ . Using this expression, the vertical torque  $\Gamma_z$  is related to the change in separation  $\dot{r}_p$  by

$$\Gamma_z = \frac{M_p v_k}{2\dot{r}_p}. \quad (2.6)$$

A natural timescale for migration is  $\tau_m = r_p/\dot{r}_p$ .

### 2.1 Migration Regimes

#### 2.1.1 Type I: Low-mass planet migration

If a planet doesn't significantly perturb the disk, the steady state density structure can be estimated through linear perturbation analysis. Let  $v_0$  and  $p_0$  be the unperturbed velocity and pressure. The orbiting planet introduces perturbations  $v_1$  and  $p_1$  such that  $v_1 \ll v_0$  and  $p_1 \ll p_0$ . It is possible to define the enthalpy perturbation as  $\eta = p_1/\rho_0$ . The perturbed velocity, pressure, enthalpy and gravitational potential of the planet are fourier-decomposed as

$$X = \sum_m Re[X_m e^{im(\phi - \Omega_p t)}], \quad (2.7)$$

where spherical coordinates  $(r, \theta, \phi)$  are used. Solving Eqs. 2.2 and 2.3, for the fourier amplitudes  $X_m$  of perturbed velocities and enthalpy results in a wave equation for  $\eta_m$ . The amplitude of the enthalpy wave  $\eta_m$  is found to diverge for two cases: when  $4B\Omega - m^2(\Omega - \Omega_p)^2 = 0$  and when  $\Omega - \Omega_p = 0$ . The first case occurs at positions  $r_m$  in the disk where  $4B\Omega(r_m) = m^2(\Omega(r_m) - \Omega_p)$ , where  $B$  is the Oort's constant. These locations are referred to as Lindblad resonances, and are located inside and outside the orbit of the planet, moving asymptotically towards  $r_p$  as  $m$  increases to infinity. The second divergent case occurs at the position  $r_c$  where  $\Omega(r_c) = \Omega_p$ , which is the corotation resonance. Due to the pressure gradient, the corotation resonance is offset from the position of the planet (Lin and Papaloizou, 1986; Tanaka et al., 2002; Ward, 1997).

The angular momentum flux carried by the waves, can be approximated as

$$F_w = \int_0^{2\pi} \int_{-\infty}^{\infty} d\phi dz r^2 \rho_0 v_{1,\phi} v_{1,r}, \quad (2.8)$$

which by conservation of angular momentum, will be given to/by the planet in terms of orbital angular momentum. The effective torque felt by the planet due to this angular momentum flux is given by

$$\Gamma_I = -(2.340 - 0.099a + 0.418b) \left( \frac{q}{h_p} \right)^2 \Sigma_p r_p^4 \Omega_p^2, \quad (2.9)$$

where  $q = M_p/M_{star}$  and  $h_p$  is the pressure scale height of the disk. This is the Type I migration regime for low-mass planets (Tanaka et al., 2002). This is valid in locally isothermal disks with power law density profiles, where  $\Sigma = \Sigma_0 r^{-a}$  and  $b$  is the power law exponent of the temperature profile.

### 2.1.2 Type II: Gap-opening planets

As the mass of the planet increases above a certain limit, the perturbations on the disk density become highly non-linear. The planet opens a partial or full cavity in the disk density around its orbit, pushing material away from corotation. The limiting mass for gap opening can be expressed in terms of two criteria: the viscous and the pressure criteria. In the first case, a condition for gap opening is that the angular momentum transported by the waves  $F_w$  matches or exceeds the angular momentum transported by viscous processes in the disk  $F_\nu$ . Taking a gaussian profile for the density in the vertical direction, and writing the dynamic viscosity  $\eta$  in terms of the surface density  $\Sigma = \int \rho dz$ , the viscous angular momentum flux is

$$F_\nu = 3\pi\Sigma r^2\Omega. \quad (2.10)$$

Letting  $q = M_p/M_{star}$ , and equating  $F_w = F_\nu$ , results in a lower limit for the mass of the planet given by

$$q > \frac{40\nu}{\Omega r^2}. \quad (2.11)$$

The viscosity can be modelled as a turbulent viscosity parameterized by  $\alpha$ , where  $\nu = \alpha\Omega_k H^2$  and  $H = c_s/\Omega_k$ . In this case, the viscous criteria can be expressed as the maximum value of  $\alpha$  that allows for gap opening

$$\alpha < \frac{q}{40} \left( \frac{r}{H} \right)^2. \quad (2.12)$$

## 2. PLANET-DISK GRAVITATIONAL INTERACTIONS

---

As a second condition for the planet to open a gap, the Hill radius of the planet must exceed the pressure scale height  $r_h = (q/3)^{1/3} > H$ . This can be expressed as a condition on the mass of the planet

$$q > 3 \left( \frac{H}{r} \right)^3. \quad (2.13)$$

As opposed to the migration of low-mass planets, where the planet angular momentum flux can never match the viscous flux in the disk, a large-mass planet that satisfies Eq 2.12 and Eq 2.13 can be in a position in the disk where the wave torque is cancelled out. This means the planet is stationary in the frame moving radially with the disk at the viscous rate. In this case, the effective torque on the planet is given by

$$\Gamma_{II} = -\frac{2\pi}{M_p} \left( \frac{3}{2} r_p^2 \Omega_p \nu \Sigma \right) \quad (2.14)$$

This is Type II migration regime for gap opening planets (Bryden et al., 1999; Crida et al., 2006). The timescale for migration is then the viscous accretion timescale  $\tau_\nu = (2r^2)/(3\nu)$ .

### 2.1.3 Type III: Intermediate cases

An interesting migration case occurs for intermediate-mass planets (sub-Saturns to Jupiters) that open a partial gap in the disk. If the disk is massive enough and the gas mass in the coorbital region is comparable or larger to the mass of the planet, the planet can migrate inwards in a runaway process. The torque coming from the corotation region can have a negative contribution due to open streamlines that go from the inner disk to the outer disk, passing the planet. This torque scales with the radial drift rate of the planet and is proportional to the mass located in the corotation region (Masset and Papaloizou, 2003).

## 2.2 Migration in non-isothermal disks

In the case of adiabatic disks, or disks where the temperature structure is allowed to vary according to the evolution of the density and the stellar flux, low-mass planets can migrate outwards in certain conditions. A component of the corotation torque that scales with the entropy gradient (which is not present in locally isothermal disks) can be present in cases of high opacities or a fully adiabatic disk. This component is positive and can overcome the negative wave torque, making the planet drift outwards. This effect will usually saturate (i.e. the torque will go to zero in short timescales) as the entropy gradient is removed by motions in the horseshoe region. Similar to the vortensity-related corotation torque that can remain un-saturated due to viscosity, the entropy-related corotation torque can remain un-saturated due to fast local cooling (Baruteau and Masset, 2008; Kley et al., 2009).

## 2.3 Corotation Torques

From a frame of reference moving with the planet at an angular frequency  $\Omega_p$ , gas particles within a certain distance of  $r_p$  move on horseshoe orbits around the position of the planet. These gas particles orbit in trajectories that follow equipotential surfaces defined by the two body-problem, around Lagrangian points. On the side trailing the planet, particles move radially inwards, while on the leading side they move radially outwards. Each time a particle executes a U-turn as it makes its closest approach to the planet, its angular momentum changes. The change in angular momentum with time will determine the torque exerted on the planet due to particles in horseshow orbits [Masset \(2002\)](#); [Paardekooper and Papaloizou \(2009a,b\)](#).

The corotation torque can be estimated by calculating the change in angular momentum of gas particles that move from the outer(inner) disk to the inner(outer) disk, at the trailing(leading) side of the planet. Assuming particles are matched symmetrically to either part of the planet as they execute a U-turn, and the half-width  $x_s$  to be the same at each side, the total change in angular momentum can be given as a integral over the half-width of the horseshoe region. For the trailing side, this is given by

$$\Delta L_t = \int_{r_p+x_s}^{r_p} (f(2r_p - r) - f(r))dr, \quad (2.15)$$

while for the leading side this is given by

$$\Delta L_l = \int_{r_p-x_s}^{r_p} (f(2r_p - r) - f(r))dr. \quad (2.16)$$

Here  $f(r)$  is the angular momentum of a gas particle at  $r$ , and is equal to  $f(r) = \Sigma(r)v(r)r$ . The net change in angular momentum is then  $\Delta L_t + \Delta L_l$ . The torque can be shown to scale with the gradient of the vortensity  $(d/dr)(\Sigma/w)$ , where  $w$  is the vorticity. This effect will usually saturate (i.e. the torque will go to zero in short timescales) as the vortensity gradient is removed by motions in the horseshoe region, unless a sufficiently high viscosity is present ([Masset, 2002](#); [Paardekooper and Papaloizou, 2009a,b](#))

## 2. PLANET-DISK GRAVITATIONAL INTERACTIONS

---

### 3

# Type II migration and gas accretion onto planets in disks with uniform constant mass accretion

*Using two-dimensional hydrodynamical simulations, we study the orbital migration and gas accretion of a free-moving planet of mass  $M_p = 2M_{Jup}$  purely in the stage where a gap has been cleared in the disk by the planet. The viscosity in the disk is chosen to obtain a constant mass accretion rate through the entire disk, independent of time and radial position. We study the effects of various parameters like the surface density, density power-law exponent, gravitational softening and viscosity. We find that the torque of the planet is best approximated by the expression  $\Gamma = -\frac{3}{2q}r^2\nu\Omega_p\Sigma$ , for a wide range of disk densities. When the local disk mass is around 10 times the planet mass, we observe runaway migration and the planet migrates inwards much faster than the analytical estimate. Only when the Hill sphere material is not taken into account in the orbital evolution, or when the planet is accreting, the migration of the planet is slowed down if it is in the regime where the local disk mass is larger than the planet mass. The torques exerted on the planet do not depend on the steepness of the density profile. We also study the accretion of gas onto the planet, and find that the accretion rate measured in the simulations is a fraction of the disk accretion rate, and is given by  $\dot{M}_p = 3\pi\nu\Sigma_{gap} \approx (0.1)3\pi\nu\Sigma_0$ .*

### 3. TYPE II MIGRATION AND GAS ACCRETION ONTO PLANETS IN DISKS WITH UNIFORM CONSTANT MASS ACCRETION

---

#### 3.1 Introduction

The migration of giant planets due to disk torques is one of the mechanisms that can partially explain the population of giant exoplanets orbiting at small separations from the central star (Alibert et al., 2004, 2005; Benz et al., 2008; Currie, 2009; Ida and Lin, 2008; Mordasini et al., 2009b). An exoplanet belonging to this population of Hot Jupiters ( $M_p \approx M_{jup}$  and  $a \approx 0.1AU$ ) cannot form in situ, either by the standard core accretion formation scenario or by disk gravitational instability and collapse. At such small separations, the disk temperature is too high and the disk doesn't carry enough solid and gas material to form a planet with a mass close to a Jupiter mass.

The gravitational torques by the gas disk provide a mechanism to move a planet that formed in the outer parts of the disk to very small separations, where then it can be stopped by the presence of an inner disk cavity or other mechanisms (Crida and Morbidelli, 2007). It is well known from analytical calculations (Lin and Papaloizou, 1986; Ward, 1997) and extensive numerical studies (Crida et al., 2006; de Val-Borro et al., 2006; Masset et al., 2006a; Nelson et al., 2000) that planets in the Jupiter mass range open a gap in the disk, pushing material away from its orbit due to tidal torques. The depth of the gap depends on the ratio of the planet mass to the primary mass and on the disk viscosity and pressure scale height at the position of the planet. As a planet opens a gap in the disk, it is said to be migrating in the Type II regime.

Quite a number of analytical studies have been done studying Type II migration. Lin and Papaloizou (1986) studied gap opening and migration as a function of the viscosity as compared to the tidal forces, and as a function of the ratio of disk to planet mass. It was found that for planets with a small mass compared to the disk mass, migration was dominated by the viscous evolution of the disk. In the interior parts of the disk, the planet will migrate inwards, while after a given radial position in the disk, the planet will migrate outwards where the disk is viscously spreading outwards as it receives the angular momentum transferred from the inner accreting disk. A planet that is very massive compared to the disk mass has no significant orbital evolution.

Crida et al. (2006) modelled the tidal torque exerted by the planet in terms of a torque component that is locally deposited in the disk, while another component that is carried away by waves supported by pressure. They described the evolution of the surface density of the disk using an semi-analytic model and correctly predict the evolution of the gap profile and provide a criteria for gap opening (Crida and Morbidelli, 2007). Modeling the viscous evolution of the disk following Lynden-Bell and Pringle (1974), Type II migration has been divided in regimes separated by that dominated by the planet (planet more massive than disk) and that dominated by the disk (disk more massive than planet). In the planet dominated regime, migration rates is dependent on disk and planet masses, while in the disk dominated regime, migration is determined by the disk accretion speed,

---

### 3.2 Gap opening and type II migration

which significantly slows down migration as compared to Type I rates or Type II in the planet dominated regime (Armitage, 2007a,b; Syer and Clarke, 1995).

Three-dimensional hydrodynamics calculations have shown that the surface density of the disk can be correctly modelled using two-dimensional simulations with proper gravitational potential smoothing. The mass of the disk present inside the Roche lobe of the planet is also critical for the torque determination and can in some cases reverse inwards migration. Jupiter-mass planets have also been found to be able to accrete very efficiently through gaps, as compared to the disk mass accretion, although this might depend on the numerical algorithm used to model planet accretion in a grid numerical code. Additionally as the planet mass increases above a Jupiter-mass, accretion efficiency decreases. (Bate et al., 2003; Bryden et al., 1999; Lubow et al., 1999).

Crida and Morbidelli (2007) performed two-dimensional hydrodynamical simulations of Type II migration coupled with a one-dimensional simulation of a viscously spreading disk, in order to correctly model the global viscous evolution of the disk. They observed the effects of the corotation torque for planets that open a partial gap when the disk has enough viscosity to maintain the torque corotation torque unsaturated. This effect can in principle slow down or reverse the inwards migration of planets that open partial gaps (D'Angelo et al., 2005). Edgar (2007) performed a study of migration as a function of disk mass and viscosity and obtained interesting results on the discrepancy between analytical estimates of migration in the Type II range and two-dimensional numerical simulations. In this chapter we revisit the issue of the dependence of Type II migration rates on the disk mass, and on the disk surface density gradient. We focus on how different numerical set ups can yield very different results, and how migration rates derived from numerical simulations compare with analytical models. We also provide estimates of migration rates in the Type II regime, directly obtained from simulations, that can be used in planet population synthesis models to more accurately estimate the migration of giant planets. This chapter is organized as follows. In section 2, we summarize the analytical expressions for the Type II torque. Section 3 describes the set up of the simulations, the parameters used and the initial conditions. We also show a test of the numerical scheme to verify the correct viscous evolution in the disk. In Section 4 we present our results for various numerical set ups and parameters. Finally, the conclusions of the study are presented in Section 5.

### 3.2 Gap opening and type II migration

Planets migrate in the Type II regime when they open a gap in the disk around their orbit. In this case, the density perturbations induced by the planet can no longer be treated as linear since the disk density is drastically modified in the gap region. The transition into

### 3. TYPE II MIGRATION AND GAS ACCRETION ONTO PLANETS IN DISKS WITH UNIFORM CONSTANT MASS ACCRETION

---

this regime is approximately given by the conditions that

$$(M_p/M_s)(1/(3h_p^3)) > 1, \quad (3.1)$$

and

$$M_p/M_s > 40\nu/r_p^2\Omega_p, \quad (3.2)$$

meaning that the planet has to be able to overcome both the pressure gradient and the viscous transport at its given position in the disk (Crida and Morbidelli, 2007; Lin and Papaloizou, 1986).

After the gap has opened, the torques on the planet cannot consistently move the planet in the disk, since it can take an equilibrium position inside the gap where the total net torque is zero instantaneously. This effectively means that the planet is stationary in a frame moving with the disk, at the viscous rate. One can assume that the giant planet now moves at the radial velocity given by the equations for the viscous evolution of the disk,  $v_r = -3\nu/2r$  (Lynden-Bell and Pringle, 1974). This in turn can be integrated to give the radius of the planet as a function of time

$$r(t) = (r_0^2 - 3\nu t)^{1/2}, \quad (3.3)$$

where  $r_0$  is the initial position of the planet at  $t = 0$ . The torque felt by the planet at a given location,  $\Gamma(r) = rv_r\Omega_p/2$ , is then given by

$$\Gamma = -\frac{3}{4}\nu\Omega_p. \quad (3.4)$$

However this expression is not correct for a broad range of disk to planet mass ratios. The expression can be modified to take into account this variation. In this case, the radial velocity of the planet is given by  $v_r = -(M_s/M_p)3\nu\Sigma r$ , which can be integrated to give the position of the planet as a function of time

$$r(t) = r_0 e^{-3\nu\Sigma t/q}, \quad (3.5)$$

which is valid for  $a = 0$  only. Here  $q = M_p/M_s$  and  $r_0$  is the initial position of the planet. The time-averaged torque exerted by the disk at a given radial position is then given by

$$\Gamma = -\frac{3}{2q}r^2\nu\Omega_p\Sigma. \quad (3.6)$$

### 3.3 Description of the setup of the simulations

We performed the simulations using the Hydrodynamics module of the Godunov code PLUTO (Mignone et al., 2007). In the code, time stepping is done using a second order

### 3.3 Description of the setup of the simulations

---

Runge Kutta integrator, while space interpolation is done with the second order linear TVD approximation. For computing the fluxes through the cell interfaces, we use the HLLC approximate Riemann solver. We work in polar geometry  $\mathbf{r} = (r, \phi)$ , where the computational domain is given by  $r \in [0.4, 4.0]$  and  $\phi \in [0, 2\pi]$ . The resolution in the radial and azimuthal direction is  $(N_r, N_\phi) = (128, 256)$  and the grid is uniform.

#### 3.3.1 Disk profile and planet setup

The initial surface density profile of the disk is given by

$$\Sigma = \Sigma_0 r^{-a}. \quad (3.7)$$

The equation of state of the disk is given by  $p = c_s \Sigma$ , where  $c_s$  is the sound speed. The disk is assumed to be locally isothermal, so that the temperature drops radially as  $T \propto r^{-1}$  and is constant in time. Hence, the sound speed is given by  $c_s = c_0 r^{-0.5}$  and the effective pressure scale height of the disk is set to the standard value of  $c_s = h = 0.05$ . The initial azimuthal velocity is equal to the Keplerian value corrected by the pressure contribution

$$v_\phi = \sqrt{\frac{GM_s}{r} (1 - c_s^2(a + 1))}. \quad (3.8)$$

The gravitational potential felt by the disk at a location  $\mathbf{r}$  includes the stellar and planetary contributions, and is given by

$$\Phi_g(\mathbf{r}) = -\frac{GM_s}{|\mathbf{r} - \mathbf{r}_s|} - \frac{GM_p}{(|\mathbf{r} - \mathbf{r}_p|^2 + \epsilon^2)^{1/2}}, \quad (3.9)$$

where  $\mathbf{r}$ ,  $\mathbf{r}_s$  and  $\mathbf{r}_p$ , are the positions of the gas, star and planet respectively, measured from the center of mass of the star-planet system. Also,  $\epsilon = kr_{hill}$  is the softening parameter of the potential, to avoid divergent forces on the disk near the planet. The constant  $k$  is less than one. The ratio between the planet mass and the stellar mass is given by  $q = M_p/M_s = 2 \times 10^{-3}$ . The initial position of the planet is set to  $r_p = 1.5$ . The planet is free to migrate and its equations of motion are integrated using a leap frog integrator. The simulations are run for 500 or 1500 periods of the planet.

The  $z$  component of the torque  $\Gamma$  exerted by the disk on the planet is given by

$$\Gamma_z = GM_p \int \Sigma(\mathbf{r}) \frac{(\mathbf{r}_p \times \mathbf{r})_z}{(|\mathbf{r} - \mathbf{r}_p|^2 + \epsilon^2)^{3/2}} dA, \quad (3.10)$$

where  $(\mathbf{r}_p \times \mathbf{r})_z = (\mathbf{r}_p \times \mathbf{r}) \cdot \hat{e}_z$ , with  $\hat{e}_z$  being the cartesian unit vector in the  $z$  direction. The torque is calculated for every timestep of the hydro code. We work in normalized units, where  $GM_s = 1$  and positions and velocities are normalized to  $r_0 = 1$  and  $v_k(r_0) = 1$ . We

### 3. TYPE II MIGRATION AND GAS ACCRETION ONTO PLANETS IN DISKS WITH UNIFORM CONSTANT MASS ACCRETION

---

*note that all torques in the following sections are negative quantities presented as absolute values*

The kinematic viscosity  $\nu$  is in general radially varying with a power law and is given by  $\nu = \nu_0 r^a$ , where  $a$  is the radial exponent of the surface density in Equation 3.7. We take this form of the viscosity so that for all of the simulations, the disk mass accretion rate  $\dot{M} \sim 3\pi\nu\Sigma$  is radially constant.

#### 3.3.1.1 Parameters of the simulations

We study migration rates both as a function of the radial exponent  $a$  of the surface density (where  $\nu = \nu_0 r^a$ ) and as a function of surface density and viscosity. In simulations that vary the radial exponent, the surface density is constant  $\Sigma_0 = 1 \times 10^{-4}$ . The radial exponent is varied for the values  $a = 0.0, 0.5, 1.0$  and  $1.5$ . In simulations that vary the surface density, we choose values in a large range, from local disk mass very small compared to the planet mass, to local disk mass larger than planet mass. Here the radial exponent is fixed to  $a = 0$ . The surface density constant is varied for the values  $\Sigma_0 = 5 \times 10^{-6}, 1 \times 10^{-5}, 5 \times 10^{-5}, 1 \times 10^{-4}, 5 \times 10^{-4}, 1 \times 10^{-3}$  and  $3 \times 10^{-3}$ .

#### 3.3.2 Test of the viscous evolution of the disk

Since migration speeds of gap-opening planets are critically dependent on the disk viscous evolution, it's necessary to correctly model this evolution numerically. Figure 3.1 shows the mass accretion rate measured in simulations with no planet included, for different values of the surface density and  $a = 0$ . We have implemented boundary conditions that set the velocity of the flow at each radial boundary to that determined by the analytical expression for the constant mass accretion rate for each value of the surface density. This ensures a constant flow of mass through the disks that matches well with the expected value resulting from theory. The density profile is not modified up to more than a few percent of its initial value (only close to the boundaries) and the disk achieves a steady state.

### 3.4 Results

#### 3.4.1 Dependence of migration on surface density

In this section, we study the Type II migration regime of giant planets for a range of disks density. First we present the results for the case when the planet is not allowed to migrate, and then the results in the case when the planet is allowed to move radially.

For a planet mass of  $q = M_p/M_s = 2 \times 10^{-3}$ , we followed the evolution of the orbital elements and the torque experienced by the planet over 1500 orbits (or 500 orbits for a

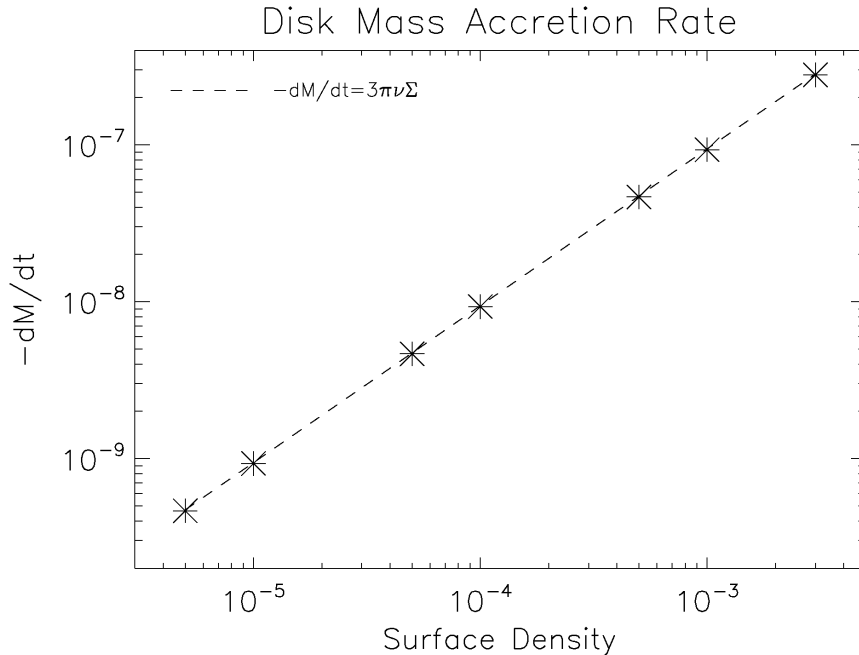


**Figure 3.1:** Disk mass accretion rate measured in the simulations. The analytical estimate  $\dot{M} = -3\pi\Sigma\nu$  is shown in the dashed line.

fixed-orbit planet). This was done for different values of the surface density, (equivalently the  $B = (\pi r_p^2)\Sigma/M_p$  parameter), such as to cover the regime when the planet is more massive than the disk  $B < 1$ , to where the local disk mass is more massive than the planet  $B > 1$ . The local disk mass is taken to be  $M_{disk} = \pi r_p^2 \Sigma$ .

#### 3.4.1.1 Fixed orbit planet

For the case in which the planet is not a fixed orbit, at  $r_p = 1.5$ , Figure 3.2 shows the evolution of the cumulative torque exerted on the planet, for different values of the surface density (colored lines) and for two values of the gravitational softening. The gravitational softening parameter  $\epsilon$  is used in the expression for the gravitational potential (see Eq. 3.9) to avoid the divergence at the position of the planet, and near it where the potential grows fast. We study how the choice of the parameter and the inclusion/exclusion of the Hill sphere material affects the torque felt by the planet. Figure 3.2 shows that the evolution of the torques is slightly different in the two cases. The case with the smaller value  $\epsilon = 0.06$  converges faster and to slightly higher values than the case with the larger value  $\epsilon = 0.3$ . The material moving around the planet has a negative contribution to the torque (making the torque larger), meaning that the planet will drift inwards slightly faster. Figure 3.2 also shows that the dependence of the torque on the surface density is

### 3. TYPE II MIGRATION AND GAS ACCRETION ONTO PLANETS IN DISKS WITH UNIFORM CONSTANT MASS ACCRETION

---

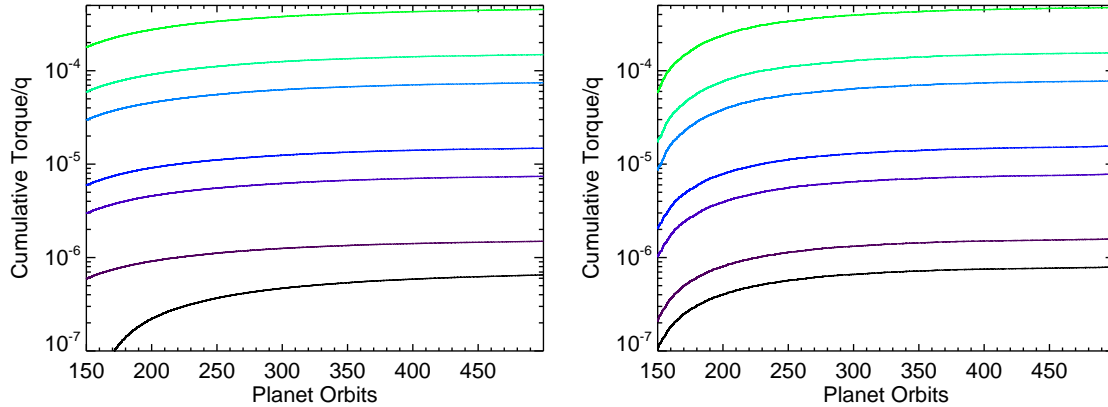


**Figure 3.2:** Cumulative average torques on the planet for varying surface density (where  $\Sigma=\Sigma_0$ ) for  $\epsilon = 0.3$  (left) and  $\epsilon = 0.06$  (right). From dark to light curves,  $\Sigma_0 = 5 \times 10^{-6}, 1 \times 10^{-5}, 5 \times 10^{-5}, 1 \times 10^{-4}, 5 \times 10^{-4}, 1 \times 10^{-3}$  and  $3 \times 10^{-3}$ , respectively. This corresponds to  $B = (\pi r_p^2) \Sigma / M_p = 0.017, 0.035, 0.17, 0.35, 1.76, 3.53$  and  $10.6$ .

linear as is expected from Eq. 3.6.

The shape of the gap is also affected by the choice of gravitational softening parameter, as is seen in Figure 3.3. The gaps are deeper for  $\epsilon = 0.06$  since the pressure gradient and viscous torque in the gap wall has to overcome a larger gravitational torque pushing the material inwards/outwards, putting the equilibrium position (the gap edge) farther away. The gaps are also wider for the smallest  $\epsilon$ , specially for the disk with larger densities. Additionally, more material accumulates around the planet for  $\epsilon = 0.06$  (see Figure 3.4).

Figure 3.5 shows the average cumulative torque as a function of surface density (or B parameter) for both values of  $\epsilon$ . We find agreement with the analytical expression for the torque for all disk densities. In general, the runs with smaller softening match the estimate better and resolve the potential around the planet in a more accurate way. The torques with the larger softening, systematically underestimate the torque, if the Hill sphere is not taken into account. Provided with sufficient resolution, the choice of smaller softening models the potential better, although it might lead to numerical issues (very fast velocities and short timesteps) close to the planet.

#### 3.4.1.2 Free moving planet: Effect of the Hill sphere

We now turn to the case where the planet is allowed to migrate according to the disk gravitational pull. We study two cases. One where we take into account the full disk to calculate the planet's acceleration, and another case where material from the Hill sphere is excluded from this calculation.

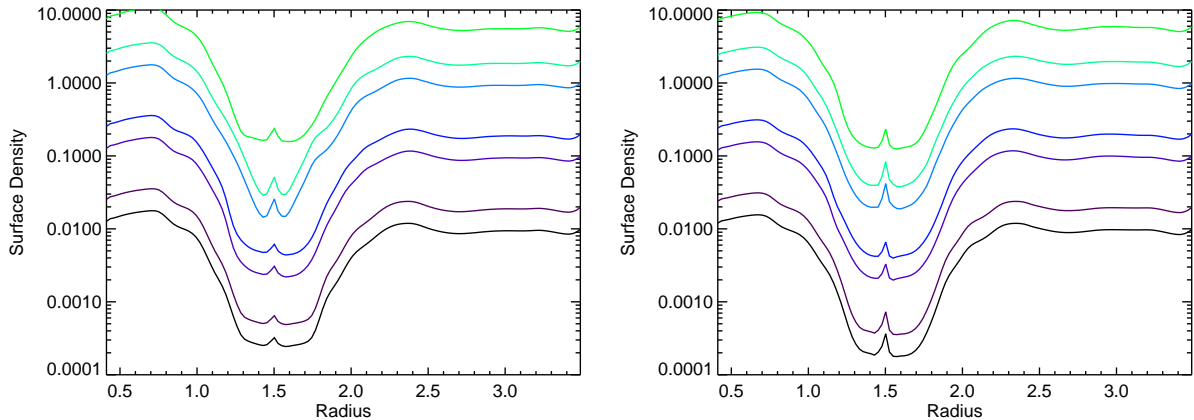


**Figure 3.3:** Surface density after 500 orbits for  $\epsilon = 0.3$  (left) and  $\epsilon = 0.06$  (right). Initial densities are  $\Sigma_0 = 5 \times 10^{-6}$ ,  $1 \times 10^{-5}$ ,  $5 \times 10^{-5}$ ,  $1 \times 10^{-4}$ ,  $5 \times 10^{-4}$ ,  $1 \times 10^{-3}$  and  $3 \times 10^{-3}$ .

Figure 3.6 shows the evolution of the cumulative torque exerted on the planet, for different values of the surface density. In the left(right) plot, we excluded(included) the Hill sphere when calculating the acceleration of the planet. Figure 3.7 shows the evolution of the semi-major axis of the planet for the same simulations. When excluding the Hill sphere, the planets in the most massive disks migrate slower as compared to the planet that is moving under the influence of the entire disk. The material in the Hill sphere accelerates the planet inwards towards the central star. For the simulations shown on the plots in the right side, the planets reach the boundary of the domain in less than 400 orbital periods, and for the higher density case, the planet migrates 1AU in less than 50 orbital periods. Some runs are cut before the planet reaches the boundary due to numerical instabilities. The dependence of the cumulative average torque with respect to the surface density is shown in Figure 3.8<sup>1</sup>. Two analytical estimates for the torque are overplotted. The first estimate is given by the torque resulting from simply taking the radial velocity of the planet to be equal to the radial velocity of the viscously evolving disk. This is independent of surface density. The second estimate is given by a similar migration rate, corrected by a factor proportional to the ratio of the local disk mass to the planet mass (the  $B$  parameter, see Eq. 3.5). This is a linear function of  $B$ .

The migration of the planet never reaches the  $\Sigma$ -independent expression, which means the radial velocity of the planet is in general not the same as the mean radial velocity of the gas. For the higher values of the density, the local disk mass is larger than the planet and the planet migrates slower if one does not include the Hill sphere material in the torque calculation. The planet in the more massive disk for the case including the

<sup>1</sup>The value of the torque in this plot corresponds to the cumulative average at the end of the simulation, averaging the torque only after the first 200 orbits of the planet.

### 3. TYPE II MIGRATION AND GAS ACCRETION ONTO PLANETS IN DISKS WITH UNIFORM CONSTANT MASS ACCRETION

---

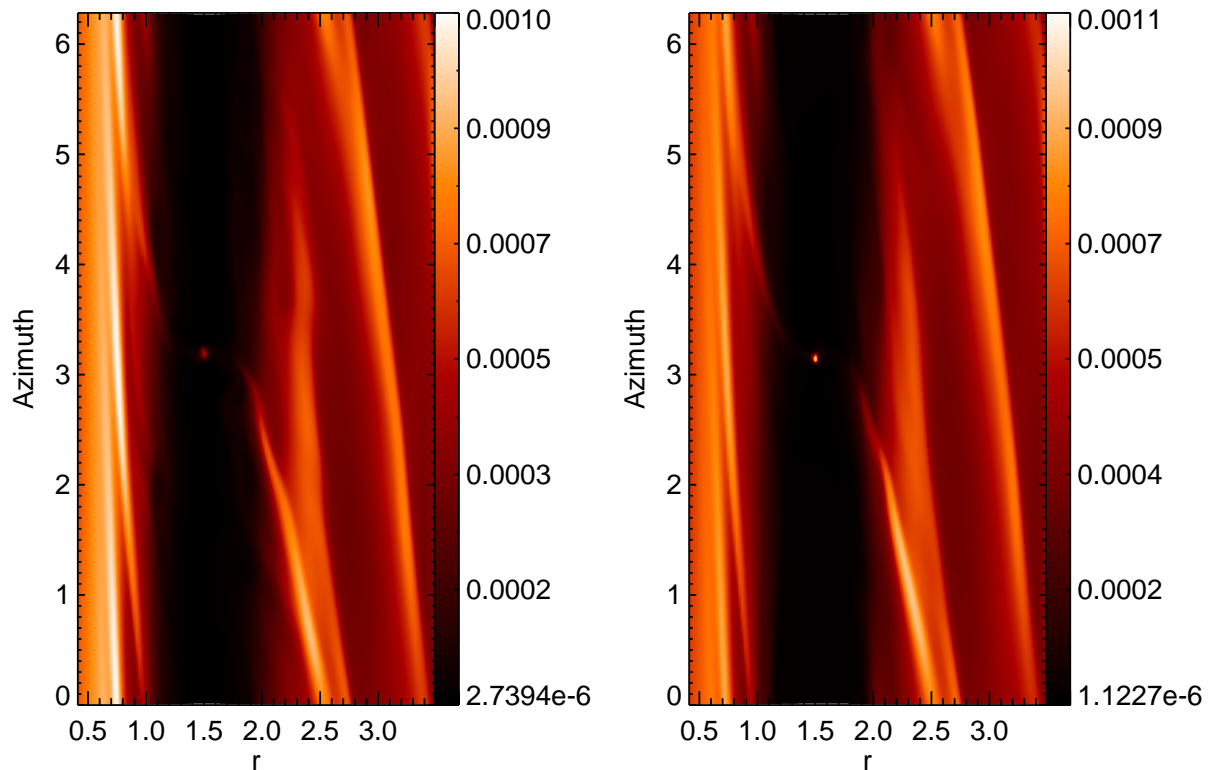


**Figure 3.4:** Density after 500 orbits for  $\epsilon = 0.3$  (left) and  $\epsilon = 0.06$  (right). The initial density is  $\Sigma_0 = 5 \times 10^{-4}$  for both cases.

Hill sphere (Figure 3.8, right plot), migrates significantly faster than the rate given by the viscous evolution of the disk  $\Gamma = -\frac{3}{2q}r^2\nu\Omega_p\Sigma$ . The planet reaches the inner boundary of the computational domain in the first 50 orbits.

#### 3.4.2 Dependence of migration on the power law exponent

We performed simulations testing the dependence of the migration rates on the exponent of the surface density  $\Sigma = \Sigma_0 r^{-a}$ . In this case the viscosity profile was chosen to be

$$\nu = \nu_0 r^a, \quad (3.11)$$

so as to produce an approximately constant mass accretion rate through the disk. The simulations were done for the surface density  $\Sigma_0 = 1 \times 10^{-4}$ . The power law exponent  $a$  was varied to take values of  $a = 0, 0.5, 1.0,$  and  $1.5$ . Figure 3.9 shows the dependence

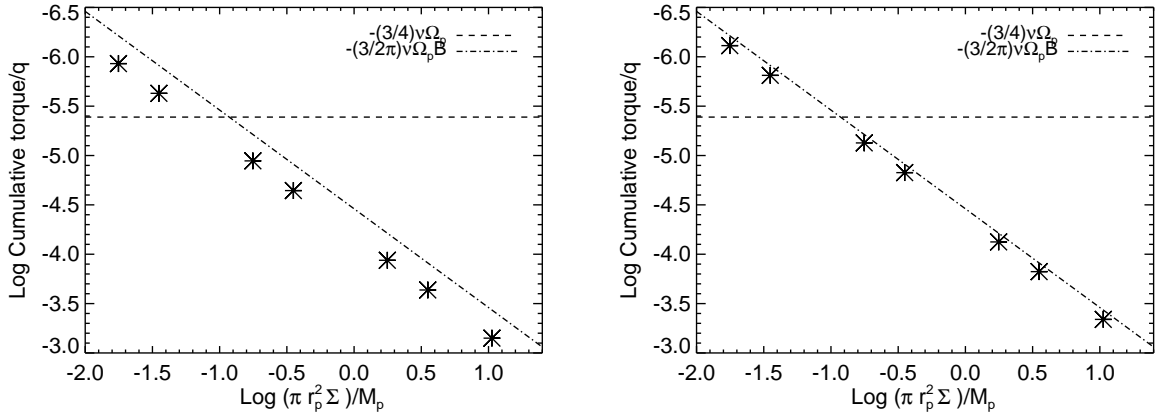


**Figure 3.5:** Dependence of the cumulative average torque on the  $B = (\pi r_p^2 \Sigma)/M_p$  parameter (where  $\Sigma = \Sigma_0$ ) for  $\epsilon = 0.3$  (left) and  $\epsilon = 0.06$  (right). The dashed line shows the analytical expression  $\Gamma = -(3/4)\nu_0\Omega_p$  (Eq. 3.4). The dash-dotted line shows the analytical expression  $\Gamma = -(3/2\pi)\nu_0\Omega_p B$  (Eq. 3.6).

of the cumulative average torque on  $a$  and the density profile after 1500 orbital periods have elapsed.

We find that the torque is independent of the surface density profile. This is true even as the planet migrates and changes position radially, thus in principle increasing the surface density that it "sees" locally. There was no measurable difference in the torque, either due to the change in radius during the 1000 orbits evolution, or due to the planet moving to parts of the disk where the density is higher ( $a > 0$ ).

### 3.4.3 Dependence of migration on disk viscosity

To study the dependence of the torque exerted on the planet as a function of viscosity, we run four different simulations with a flat density profile and different viscosities. The kinematic viscosity is set to  $\nu = 1 \times 10^{-6}$ ,  $1 \times 10^{-5}$ ,  $1 \times 10^{-4}$  and  $1 \times 10^{-3}$ . The cumulative torque as a function of time, and viscosity is shown in Figure 3.10. We see that the expression  $\Gamma = -\frac{3}{2q}r^2\nu\Omega_p\Sigma$  does not correctly match the simulated torque for different viscosities. For the lowest viscosity  $\nu = 1 \times 10^{-6}$ , the torque is found to be equal to the case when  $\nu = 1 \times 10^{-5}$ . This means that the code is not capable of handling such lower viscosities and the limit of the numerical viscosity has been reached. For values of the viscosity larger than  $\nu = 1 \times 10^{-5}$ , the torques are considerably lower than the analytical estimate. For  $\nu = 1 \times 10^{-3}$ , the simulated torque is more than one order of magnitude lower. In this case, the gap depth is only 10% of the initial density, and the corotation torque is influenced by viscosity. In the case where  $\nu = 1 \times 10^{-4}$ , almost a full gap is opened, but migration is still slowed down due to the torque exerted by the

### 3. TYPE II MIGRATION AND GAS ACCRETION ONTO PLANETS IN DISKS WITH UNIFORM CONSTANT MASS ACCRETION

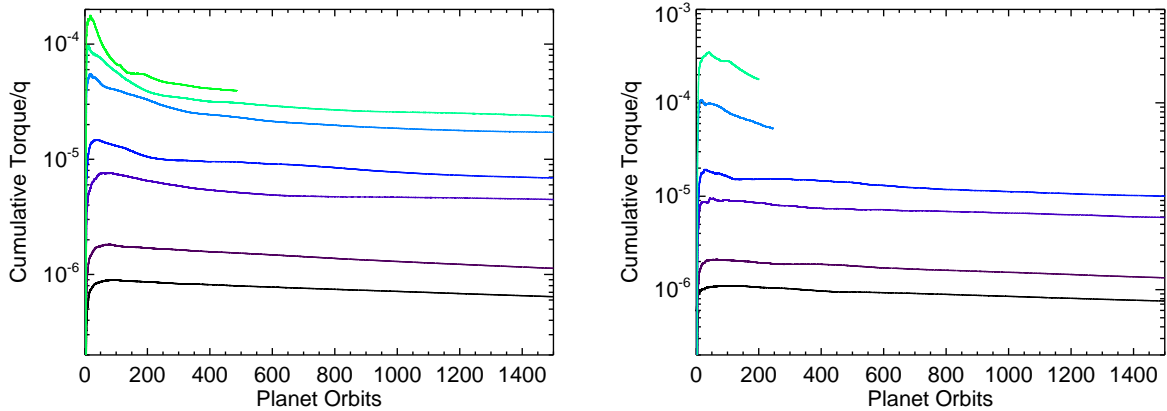


**Figure 3.6:** Cumulative average torques on the planet for varying surface density, excluding (left) and including (right) the contribution of the Hill sphere on the orbital evolution. From dark to light curves,  $\Sigma_0 = 5 \times 10^{-6}$ ,  $1 \times 10^{-5}$ ,  $5 \times 10^{-5}$ ,  $1 \times 10^{-4}$ ,  $5 \times 10^{-4}$ ,  $1 \times 10^{-3}$  and  $3 \times 10^{-3}$ , respectively. This corresponds to  $B = (\pi r_p^2) \Sigma / M_p = 0.017, 0.035, 0.17, 0.35, 1.76, 3.53$  and  $10.6$ .

remaining co-orbital material, since in this case the viscosity is high enough to maintain the corotation torque unsaturated (see [Masset \(2002\)](#)).

#### 3.4.4 Accretion of gas onto planets

In this section we present results on the accretion rates of gas onto the planet. The planet mass is the same as in the previous simulations,  $M_p = 2M_{Jup}$ . The accretion is modelled by removing a fraction of the mass inside the Hill sphere at each time step. At each timestep the new density  $\rho'$  is given by

$$\rho'(\mathbf{r}) = \left(1 - \frac{\Delta t}{t_a}\right) \rho(\mathbf{r}). \quad (3.12)$$

The accreted mass in timestep  $\Delta t$  is  $\Delta M = (\rho(\mathbf{r})t_a^{-1}\Delta t)rdrd\phi$ . The accretion rate for timestep  $\Delta t$  is calculated as the accreted mass divided by the timestep  $\Delta M/\Delta t$ . The factor  $t_a$  represents the accretion timescale in which the Hill sphere is emptied if there was no replenishing of gas. This is chosen to be  $t_a = 2$  inside the inner half of the Hill sphere (this corresponds to about 0.3 orbital periods at 1AU). The accretion rate has been shown to be dependent on the accretion radius (the distance from the planet up to which mass is removed) and on the accretion timescale parameter  $t_a$ . [Tanigawa and Watanabe \(2002\)](#) showed that the accretion radius should be small ( $\approx 0.1r_h$ ) and the accretion timescale should be on the order of the orbital period, in order to obtain converged results. Because of our lower resolution, we take most of the mass from within

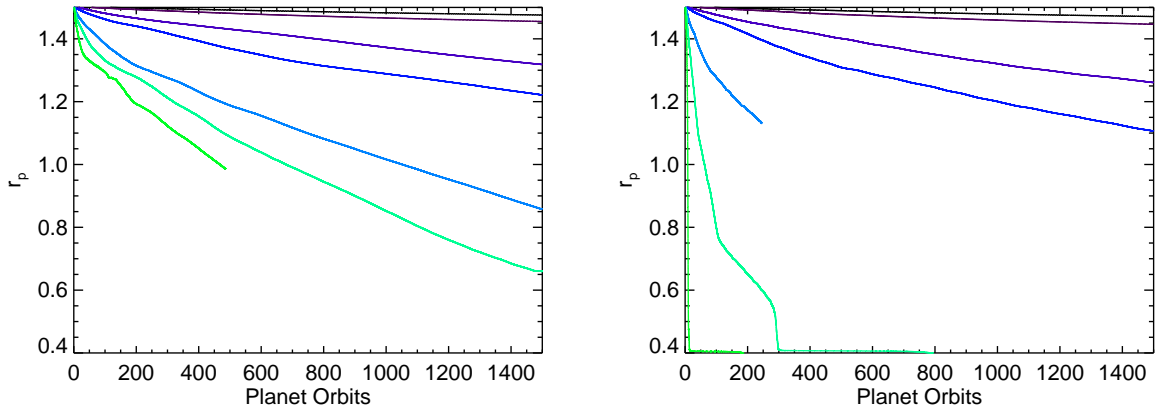


**Figure 3.7:** Planet position for varying surface density, excluding (left) and including (right) the contribution of the Hill sphere on the orbital evolution. From dark to light curves,  $\Sigma_0 = 5 \times 10^{-6}$ ,  $1 \times 10^{-5}$ ,  $5 \times 10^{-5}$ ,  $1 \times 10^{-4}$ ,  $5 \times 10^{-4}$ ,  $1 \times 10^{-3}$  and  $3 \times 10^{-3}$ , respectively. This corresponds to  $B = (\pi r_p^2) \Sigma / M_p = 0.017, 0.035, 0.17, 0.35, 1.76, 3.53$  and  $10.6$ .

the inner half of the Hill sphere. This prescription has also been used in previous studies of gas accretion and migration by giant planets (Kley et al., 2001).

Our results are originally in code units. We scale all of the results so that the disk with  $\Sigma_0 = 10^{-4}$  has a total mass of  $M_{disk} = 0.01 M_{solar}$  (inside the computational domain). The resulting disk masses and accretion rates measured in the simulations are shown in Table 3.1. The accretion rate and cumulative mass accreted as a function of time are shown in Figure 3.11. The resulting mean accretion rates as a function of the B parameter ( $B = (\pi r_p^2) \Sigma / M_p$ ) are shown in Figure 3.12. We find very good agreement with the expression  $\dot{M} = 3\pi\nu\Sigma_{gap}$ . We stress that the reduced density in the gap must be used to obtain the correct results for the accretion rate onto the planet. Table 3.1 shows the growth time  $\tau_{grow} = M_p / \dot{M}$  for the different simulations.

It is interesting to note that for the most massive disk ( $\Sigma = 3 \times 10^{-3}$ ), the planet migrates out of the grid extremely fast in the case where there was no accretion (as is seen in Figure 3.7, right plot). In that case, the entire disk was taken into account in calculating the acceleration of the planet. The simulations with accretion onto the planet use the same setup. However, we find that the planet in the most massive disk no longer undergoes runaway migration when it is accreting mass from the disk. Figure 3.13 shows the torques on the accreting planet. The torques are similar to what was found when excluding the Hill sphere material in the orbital evolution of the planet. As the planet accretes, it removes mass from its sphere of influence and for very massive disks this results in a slower inwards migration. Note that the planet is still migrating faster than the radial drift rate of the disk.

### 3. TYPE II MIGRATION AND GAS ACCRETION ONTO PLANETS IN DISKS WITH UNIFORM CONSTANT MASS ACCRETION

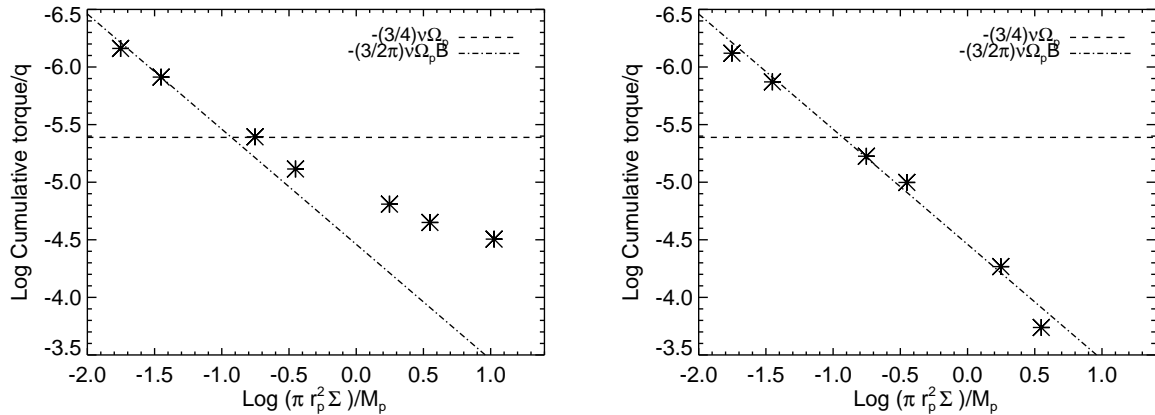


**Figure 3.8:** Dependence of the cumulative average torque on the  $B = (\pi r_p^2 \Sigma)/M_p$  parameter, excluding (left) and including (right) the contribution of the Hill sphere on the orbital evolution. The dashed line shows the analytical expression  $\Gamma = -(3/4)\nu_0\Omega_p$  (Eq. 3.4). The dash-dotted line shows the analytical expression  $\Gamma = -(3/2\pi)\nu_0\Omega_p B$  (Eq. 3.6).

$\Sigma_0$	$5 \times 10^{-6}$	$1 \times 10^{-5}$	$5 \times 10^{-5}$	$1 \times 10^{-4}$	$5 \times 10^{-4}$	$1 \times 10^{-3}$	$3 \times 10^{-3}$
$M_{disk}[code]$	$1.4 \times 10^{-4}$	$2.8 \times 10^{-4}$	$1.4 \times 10^{-3}$	$2.8 \times 10^{-3}$	$1.4 \times 10^{-2}$	$2.8 \times 10^{-2}$	$8.5 \times 10^{-2}$
$M_{disk}[M_\odot]$	$5 \times 10^{-4}$	$1 \times 10^{-3}$	$5 \times 10^{-3}$	$1 \times 10^{-2}$	$5 \times 10^{-2}$	$1 \times 10^{-1}$	$3 \times 10^{-1}$
$dM/dt[M_{Jup}/yr]$	$9.5 \times 10^{-8}$	$1.9 \times 10^{-7}$	$9.5 \times 10^{-7}$	$1.8 \times 10^{-6}$	$7.5 \times 10^{-6}$	$3.3 \times 10^{-5}$	$6.8 \times 10^{-5}$
$\tau_{grow}[yr]$	$2 \times 10^7$	$1 \times 10^7$	$2 \times 10^6$	$1 \times 10^6$	$2.6 \times 10^5$	$6 \times 10^4$	$3 \times 10^4$

**Table 3.1:** Simulations parameters and measured gas accretion rates onto the planet.

#### 3.4.5 Mass flow through gaps

An interesting question is that of how much gas is able to pass by the planet when there is a gap present. We calculate this for three different sets of simulations: the case when the planet is on a fixed orbit (presented in Section 3.4.1.1), the case when the planet is allowed to migrate (presented in Section 3.4.1.2), and the case when the planet is allowed to migrate and to accrete gas (presented in Section 3.4.4). For each case, the surface density varies as before where  $\Sigma_0 = 5 \times 10^{-6}$ ,  $1 \times 10^{-5}$ ,  $5 \times 10^{-5}$ ,  $1 \times 10^{-4}$ ,  $5 \times 10^{-4}$ ,  $1 \times 10^{-3}$  and  $3 \times 10^{-3}$ .

Figure 3.14 shows the mass flux, calculated as  $\rho(r_p)v_r(r_p)$ , and averaged in time and in the azimuthal direction. This represents the mass per unit time that passes through the orbit of the planet (i.e. per  $2\pi r_p$ ). The density  $\rho$  has been multiplied by an additional factor of  $hr_p$  to compare to the analytical expression involving the surface density. The blue symbols in Figure 3.14 denote positive values of the mass flux, which means flow of gas from the inner to the outer disk.

For the fixed orbit case, the net mass flux is negative (radially inwards), and is exactly the

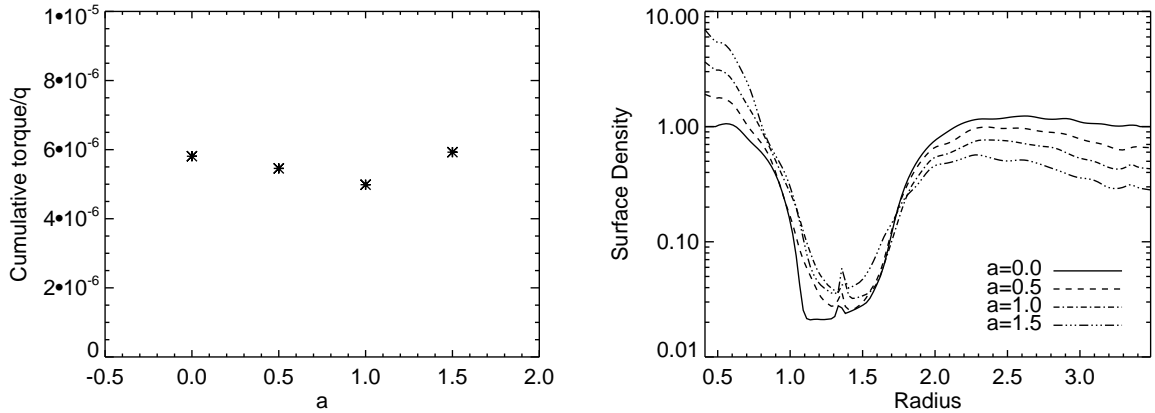


**Figure 3.9:** Left: Dependence of the cumulative average torque (taking last value at 1500 orbital periods) on the surface density exponent  $a$  parameter (where  $\Sigma = \Sigma_0 r^{-a}$  and  $\nu = \nu_0 r^a$ ), for two different values of the surface density constant  $\Sigma_0$ . Right: Surface density after 1500 orbital periods of the planet for each profile.

one expected by the viscous mass accretion rate of the disk, but taking the density at the gap region. This is equal to  $\approx -3\pi\nu\Sigma_{gap}$ . This is expected, since in this case the planet is not able to equilibrate the torque by moving into an equilibrium position with respect to the disk.

For the case where the planet is allowed to move radially according to the disk torques, the net mass flow across the gap is now positive, which means that gas is flowing from the inner to the outer disk. In this case, the planet is now migrating faster than the gas is accreting through the disk. It is interesting that in the cases with very fast migration (for the highest  $\Sigma$ ), gas flows by the planet at a rate where the mass flux is almost two orders of magnitude higher than the inwards accreting flow of the disk. The faster the planet migrates, the larger the mass flux, hence the larger negative torque on the planet due to passing by fluid elements. This is a runaway process that produces the fast migrator discussed in Section 3.4.1.2.

For the case where the planet is moving and accreting gas, we find a similar behavior as the non-accreting case, except that the outwards mass flux through the planet is reduced. Additionally we find that there is no runaway migration if the planet is allowed to accrete gas from the disk, since the Hill sphere is depleted of gas and doesn't contribute the same amount of torque. In this case it is possible that a fraction of the fluid that previously passed by the planet is now accreted as it moves into the Hill sphere.

### 3. TYPE II MIGRATION AND GAS ACCRETION ONTO PLANETS IN DISKS WITH UNIFORM CONSTANT MASS ACCRETION

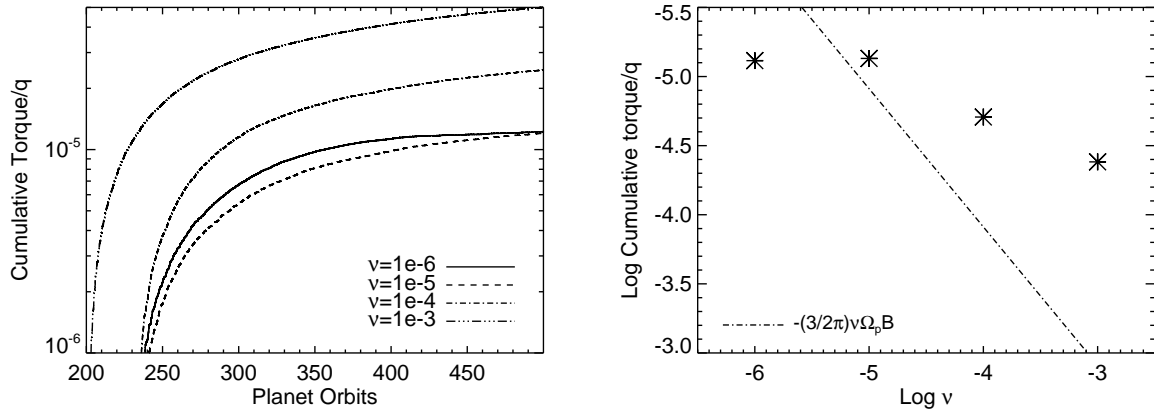


**Figure 3.10:** Left: Cumulative average torques on the planet for varying viscosity ( $\nu = 1 \times 10^{-6}$ ,  $1 \times 10^{-5}$ ,  $1 \times 10^{-4}$  and  $1 \times 10^{-3}$ ). Right: Torques vs kinematic viscosity  $\nu$ .

### 3.5 Discussion and conclusions

We have studied the migration of giant planets that open a gap in viscous disks. As a condition in all the simulations, the disk mass accretion rate is constant and is radially uniform. This implies that if  $\Sigma = \Sigma_0 r^{-a}$ , then  $\nu = \nu_0 r^a$ . We have performed simulations studying the dependence of migration and torques on variables like the surface density, density profile, viscosity, acceleration terms and gravitational softening. Additionally, we study the mass accretion rates of gas onto the planet purely in the phase when the gap has been opened.

In the case of planets migrating in very massive disks, where the local disk mass is around 10 times the planet mass, runaway inwards migration takes place due to corotation torques. In this case, the material left in the gap is still comparable to the planet mass and will influence migration critically. This scenario has been discussed by [Masset and Papaloizou \(2003\)](#); [Pepliński et al. \(2008\)](#). [Lin and Papaloizou \(2010\)](#) also studied fast inwards migration of Jupiters and Saturns in low viscosity disks. In their simulations, the planet scatters large vortices formed in the disk, losing angular momentum in the process. However, in our simulations we find that no vortices are excited. The fast inwards migration instead relates to the large amount of material left in the corotation region, even after 500 orbital periods. The material that originally performs closed horseshoe orbits is forced instead to follow an open orbit from the inner to the outer disk, transferring angular momentum as it passes by the planet. This is a runaway process that was described by [Masset and Papaloizou \(2003\)](#). Our simulations with  $h = 0.05$  and the most massive density  $\Sigma_0 = 3 \times 10^{-3}$  fall within the range where runaway migration is expected. We also find that performing this simulation with a fixed orbit planet or neglecting the Hill

### 3.5 Discussion and conclusions

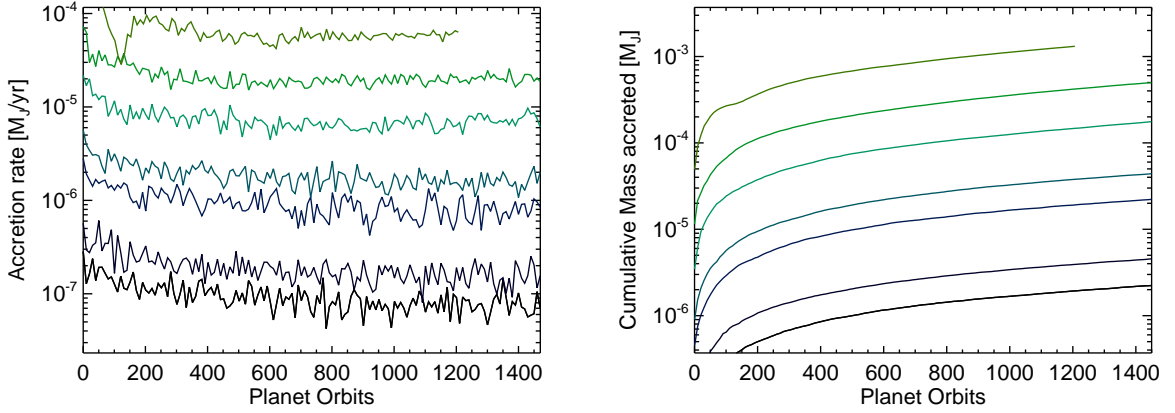


**Figure 3.11:** Left: Accretion rate of gas onto the planet for different disk surface densities. Right: Cumulative mass accreted by the planet. From dark to light curves,  $\Sigma_0 = 5 \times 10^{-6}$ ,  $1 \times 10^{-5}$ ,  $5 \times 10^{-5}$ ,  $1 \times 10^{-4}$ ,  $5 \times 10^{-4}$ ,  $1 \times 10^{-3}$  and  $3 \times 10^{-3}$ , respectively.

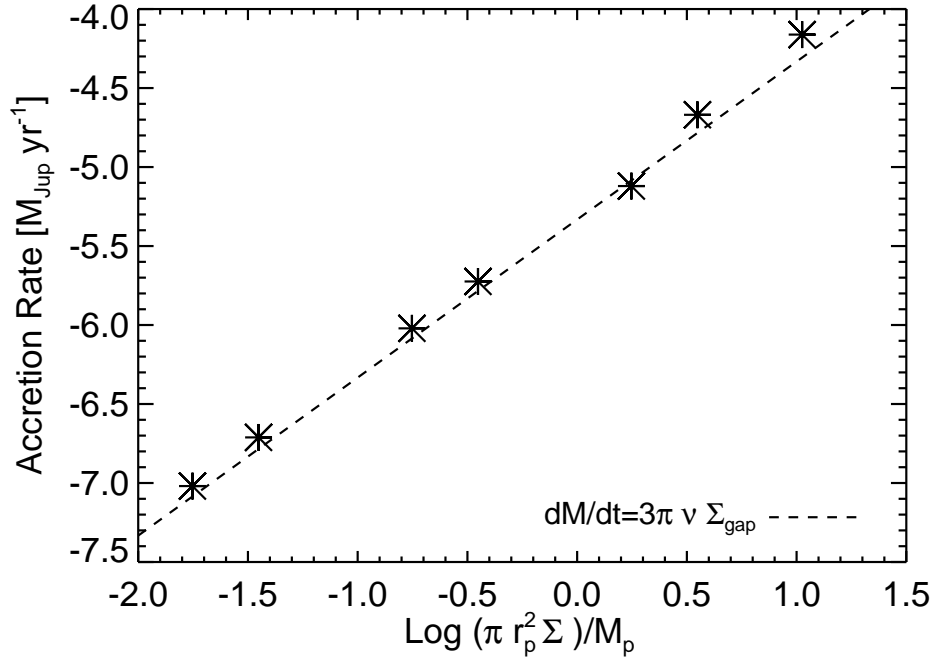


**Figure 3.12:** Accretion rates onto the planet as a function of surface density.

sphere material, does not capture this effect of runaway migration.

The material inside the Hill sphere affects the migration of planets in massive disks considerably. If the Hill sphere is neglected in the calculation of the torque, planets in more

### 3. TYPE II MIGRATION AND GAS ACCRETION ONTO PLANETS IN DISKS WITH UNIFORM CONSTANT MASS ACCRETION

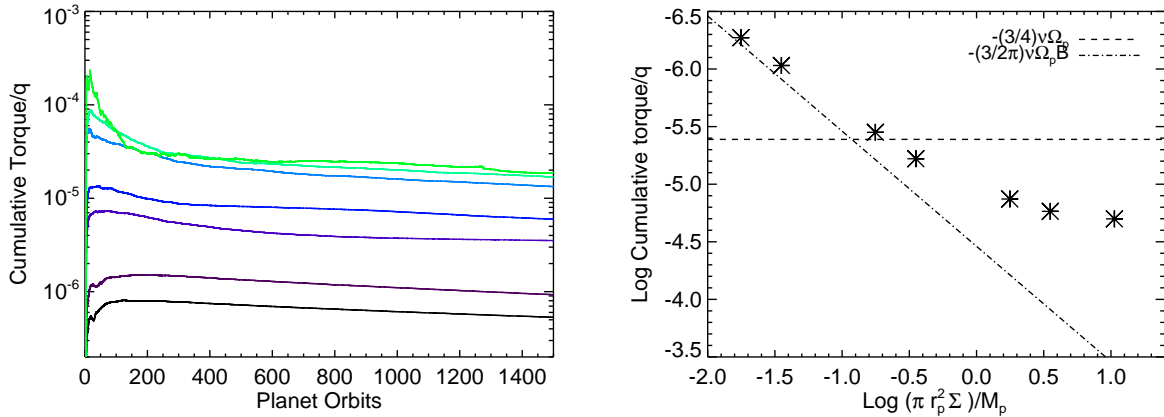


**Figure 3.13:** Left: Cumulative torques vs time for different densities. From dark to light curves,  $\Sigma_0 = 5 \times 10^{-6}$ ,  $1 \times 10^{-5}$ ,  $5 \times 10^{-5}$ ,  $1 \times 10^{-4}$ ,  $5 \times 10^{-4}$ ,  $1 \times 10^{-3}$  and  $3 \times 10^{-3}$ , respectively. Right: Dependence of the cumulative average torque on the  $B = (\pi r_p^2 \Sigma) / M_p$  parameter for an accreting planet. The dashed line shows the analytical expression  $\Gamma = -(3/4)\nu\Omega_p$  (Eq. 3.4). The dash-dotted line shows the analytical expression  $\Gamma = -(3/2\pi)\nu\Omega_p B$  (Eq. 3.6).

massive disks will migrate slower and the torques will be approximately independent of  $\Sigma$ .

Migration rates are also independent of the density profile in the disk. The torques exerted on the planet are constant as a function of surface density exponent up to  $a = 1.5$ . It is not clear if this remains valid for very massive disks. The variation of the torque with disk viscosity showed interesting behavior. For larger viscosities, the torque is no longer given by the analytical estimate that is linear with respect to viscosity. The offset of the simulated torque from the formula grows with larger viscosities. The slower migration in highly viscous disks has been observed also by [Crida and Morbidelli \(2007\)](#). This can be an effect of the corotation torque exerted by material left in the gap. At high viscosities, the corotation torque can be unsaturated and the material orbiting in horseshoe orbits around corotation exerts a positive torque on the planet, therefore slowing migration down ([Masset, 2002](#); [Paardekooper and Papaloizou, 2009a](#)).

During the gap phase of the evolution, planets accrete at a fraction of the viscous mass accretion rate, corrected to take into account the density inside the gap. This is approximately given by  $\dot{M}_p = 3\pi\nu\Sigma_{gap} \approx (0.1)3\pi\nu\Sigma_0$ . It is interesting that for the accreting planet in the most massive disk, we find no runaway migration, as opposed to the case where accretion is switched off.

The estimations of the Type II torque dependence on a wide range of parameters is useful in the modeling of synthetic planet populations that can explain and predict the observed population of extrasolar planets, specially massive planets in the gap opening regime.

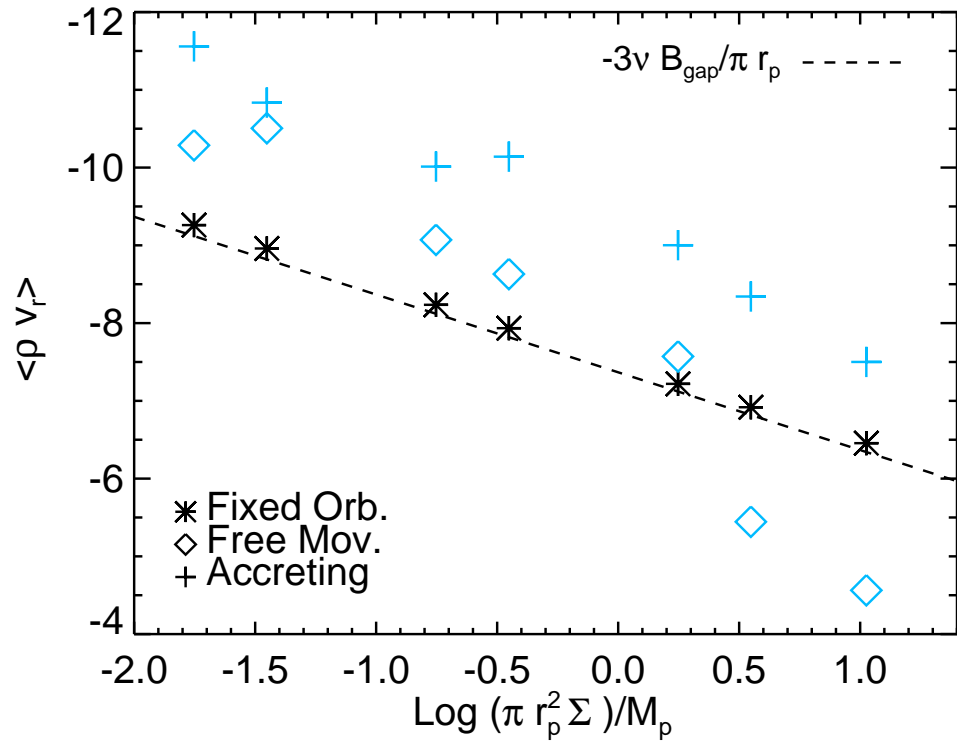


**Figure 3.14:** Mass flux  $\rho(r_p)v_r(r_p)$ , averaged in time and in the azimuthal direction at the position of the planet. The mass flux is shown for simulations with a fixed orbit planet (stars), a free moving planet (diamonds) and a free moving and accreting planet (crosses). The blue symbols denote positive values of the mass flux.

### **3. TYPE II MIGRATION AND GAS ACCRETION ONTO PLANETS IN DISKS WITH UNIFORM CONSTANT MASS ACCRETION**

---

## 4

# 3D MHD Simulations of Planet Migration in Turbulent Stratified Disks

*We performed 3D MHD simulations of planet migration in stratified disks using the Godunov code PLUTO, where the disk is turbulent due to the magnetorotational instability. We study the migration for planets with different planet-star mass ratios  $q = M_p/M_s$ . In agreement with previous studies, for the low-mass planet cases ( $q = 5 \times 10^{-6}$  and  $10^{-5}$ ), migration is dominated by random fluctuations in the torque. For a Jupiter-mass planet ( $q = M_p/M_s = 10^{-3}$  for  $M_s = 1M_\odot$ ), we find a reduction of the magnetic stress inside the orbit of the planet and around the gap region. After an initial stage where the torque on the planet is positive, it reverses and we recover migration rates similar to those found in disks where the turbulent viscosity is modelled by an  $\alpha$  viscosity. For the intermediate-mass planets ( $q = 5 \times 10^{-5}$ ,  $10^{-4}$  and  $2 \times 10^{-4}$ ) we find a new and so far unexpected behavior. In some cases they experience sustained and systematic outwards migration for the entire duration of the simulation. For this case, the horseshoe region is resolved and torques coming from the corotation region can remain unsaturated due to the stresses in the disk. These stresses are generated directly by the magnetic field. The magnitude of the horseshoe drag can overcome the negative Lindblad contribution when the local surface density profile is flat or increasing outwards, which we see in certain locations in our simulations due to the presence of a zonal flow. The intermediate-mass planet is migrating radially outwards in locations where there is a positive gradient of a pressure bump (zonal flow) <sup>a</sup>.*

---

<sup>a</sup>A version of this chapter has been published in The Astrophysical Journal, 736, 85 (2011) (Uribe et al., 2011).

### 4.1 Introduction

Understanding why and how fast planets migrate is fundamental to explaining the observed distribution of exoplanets and constraining planet formation timescales and efficiencies (Alibert et al., 2005). The basic principle behind the migration of planets in protoplanetary disks is the transfer of angular momentum between the planet and its disk. This transport process occurs at Lindblad resonances and, in a locally isothermal disk, typically leads to fast inwards migration. (Goldreich and Tremaine, 1980; Papaloizou and Lin, 1984; Tanaka et al., 2002; Ward, 1986). This is the standard type I migration scenario which applies to low- to intermediate-mass planets where the specific torque is a linear function of the planet mass (Ward, 1997).

If the planet is massive enough (the mass depending on the viscosity and the pressure scale height), the tidal forces on the disk can eventually overcome the pressure gradient and the viscous transport, causing gap opening around the planet orbit. This migration regime, referred to as type II, in which the planet-disk interaction can no longer be described by linear perturbation theory, is then conceptually very different from the type I regime. Due to the gap opening, it is possible for the torques on the planet to cancel in such a way that the evolution of the planet's position is determined by the viscous transport of gas in the disk, making the planet move with the disk on viscous timescales (Bate et al., 2003; Ward, 1997).

Current numerical and analytical calculations estimate migration timescales to be a small fraction of the expected disk lifetime, which creates a problem for the survival of planetary cores. Gas planet cores need to reach a critical mass before the onset of runaway gas accretion (Ida and Lin, 2008). It is well established that planet population synthesis models together with giant planet formation models require a much less efficient type I migration to reproduce the observed distribution of exoplanets (Alibert et al., 2005; Benz et al., 2008; Ida and Lin, 2004, 2007; Mordasini et al., 2009b; Trilling et al., 2002). Nevertheless, core survival mechanisms have also been proposed to solve the timescale problem without resorting to an artificially reduced Type I migration rate (Fromang et al., 2005; Terquem, 2003; Thommes and Murray, 2006).

Deviations from linear theory have been found in a number of three dimensional calculations. Masset (2002) and D'Angelo et al. (2003b) and later Masset et al. (2006a) found that for intermediate-mass planets (around  $M_p = 1 \times 10^{-4} M_s$ ), the torques on the planet can be significantly lower and even reverse sign when the local surface density profile of the disk is flatter ( $\Sigma \sim r^\alpha$  with  $\alpha = 0 - 0.5$ ) than in the usually assumed Minimum Mass Solar Nebula (MMSN) model  $\Sigma \sim r^{-1.5}$ . This is found for a certain range of the disk viscosity. In this case, the torques from the corotation region can become important. The fluid elements that are librating (moving in horseshoe orbits in the corotation region) orbit on a U-turn trajectory at trailing and leading sides of the planet. These

fluid elements exert a torque on the planet at each U-turn, which is a symmetric effect on both sides of the planet in an inviscid disk; therefore there is no net torque coming from this region after a few librating periods. This is referred to as the "saturation" of the corotation torque. In the presence of viscosity, if the viscous crossing timescale across the horseshoe region of accreting disk material is smaller than the libration timescale, the torques exerted by fluid elements around the U-turn are not symmetric at each side of the planet, creating a net positive torque that can be sustained. This is referred to as the "unsaturated" corotation torque, and it can depend on the surface density and on the width of the horseshoe region that in turn depends on the planet mass (Ward, 1992).

So far most numerical studies of migration and/or gap formation have concentrated on the quasi-laminar disk case, where Navier-Stokes shear viscosity is included in order to model the viscous stresses resulting from including turbulence in the disk (e.g. Bate et al. (2003); Bryden et al. (1999); Crida et al. (2006); de Val-Borro et al. (2006); Nelson et al. (2000); Papaloizou and Larwood (2000) and many more). There has been strong interest in simulating planet-disk interactions in turbulent disks, where the turbulence is magnetically generated by the magneto-rotational instability (MRI) (Balbus and Hawley, 1991, 1998). Only ideal MHD has been considered so far in global simulations. The disk is assumed to be fully ionized and the magnetic diffusivity is negligible. Winters et al. (2003) looked at gap formation by intermediate- and large-mass planets in turbulent unstratified disks and the local internal stresses around the planet. In the MHD case, they found the gap to be shallower and wider compared to the laminar HD case; the Maxwell stresses in the disk dropped in the vicinity of the planet's orbit. Papaloizou and Nelson (2003) performed a comprehensive study of protoplanets embedded in MHD-turbulent unstratified disks. They found that for low mass planets, Type I migration is no longer effective due to large fluctuations in the torque. No convergence was reached due to fluctuations of the torque on timescales longer than the orbital period and short simulation timescales. However, the torques for planets more massive than  $30M_{\oplus} = 0.1M_{Jup}$  were found to converge to the standard Type I migration torques after long-time averaging (Nelson and Papaloizou, 2003, 2004; Papaloizou et al., 2004). For low-mass protoplanets, Nelson (2005) studied the long-term evolution of the orbital elements and particularly the excitation of eccentricity by turbulent fluctuations. The evolution of the orbital elements of particles in MHD turbulence has also been studied using shearing unstratified boxes (Yang et al., 2009) and stratified boxes including a dead zone (Oishi et al., 2007). To avoid the expensive MHD simulations, other approaches have been taken, such as modeling the turbulence as a time and space varying forcing in a laminar disk model (Laughlin et al., 2004). In this case, depending on the amplitude of the forcing, type I migration can be overcome by the random fluctuations in the torque, and random walk motion will be superimposed on the smooth inward migration. Baruteau and Lin (2010) used a similar turbulent forcing model and studied the unsaturation of the corotation torque due to turbulence. Depend-

## 4. 3D MHD SIMULATIONS OF PLANET MIGRATION IN TURBULENT STRATIFIED DISKS

---

ing on the amplitude of the turbulence, the corotation torque is found to be unsaturated to a certain level, making the total torque increase accordingly (become less negative), slowing down inwards migration. Other approaches include the analytical description of stochastic migration of low-mass planets using a diffusion-advection equation (Adams and Bloch, 2009; Johnson et al., 2006) and coupling N-body simulations with a random forcing to study the accretion and formation of low-mass planets (Ogihara et al., 2007). Recently, Nelson and Gressel (2010) examined the velocity dispersion of 1 m to 10 km planetesimals embedded in a turbulent disk, using 3D MHD simulations and neglecting stratification, and characterized the stochastic gravitational perturbations felt by planetesimals due to MHD turbulence.

In this chapter, we study planet migration in stratified 3D MHD-turbulent disks for planet masses in the Type I and II mass range. In Section 4.2 we describe the numerical setup of our simulations, and the initial conditions for the disk and the magnetic field, before the addition of a planet. In section 4.3 we present the results of our simulations and finally in section 4.4 we discuss our results.

### 4.2 Simulation Setup

Simulations were performed using the finite volume fluid dynamics code PLUTO (Mignone et al., 2007). In the code, time stepping is done using a second order Runge Kutta scheme, while the spatial integration is performed using linear interpolation through the second order TVD scheme. The Riemann fluxes are computed using the HLLC and HLLD solvers for the HD and MHD cases, respectively. The code uses the Constrained Transport method for preserving a divergence-free magnetic field (Gardiner and Stone, 2005). The numerical setup for the MHD case follows the setup presented in (Flock et al., 2010). The MHD equations in the isothermal approximation (no energy equation) are given by

$$\frac{\partial \rho}{\partial t} + \nabla \cdot (\rho \mathbf{v}) = 0 \quad (4.1)$$

$$\frac{\partial \mathbf{v}}{\partial t} + (\mathbf{v} \cdot \nabla) \mathbf{v} + \frac{1}{\rho} \mathbf{B} \times (\nabla \times \mathbf{B}) = -\frac{1}{\rho} \nabla P - \nabla \Phi_g \quad (4.2)$$

$$\frac{\partial \mathbf{B}}{\partial t} + \mathbf{B}(\nabla \cdot \mathbf{v}) - (\mathbf{B} \cdot \nabla) \mathbf{v} + (\mathbf{v} \cdot \nabla) \mathbf{B} = 0 \quad (4.3)$$

The potential  $\Phi_g$  includes contributions from the star and the planet. We work in spherical coordinates  $(r, \theta, \phi)$ , where the computational domain is given by  $r \in [1, 10]$ ,  $\theta \in [\pi/2 - 0.3, \pi/2 + 0.3]$  and  $\phi \in [0, 2\pi]$ . The grid resolution is  $(N_r, N_\theta, N_\phi) = (256, 128, 256)$  and it is centered in the center of mass of the planet-star system. The boundary conditions for the velocities and magnetic field are periodic in the vertical ( $\theta$  boundary) and azimuthal directions and reflective in the radial direction, except for the transverse

magnetic field component, which reverses its sign at the radial boundary. Buffer zones are defined at the radial boundaries to avoid boundary effects, where for  $1 < r < 2$  the magnetic resistivity is given by  $\eta = 2 \times 10^{-4}(2 - r)$  and for  $9 < r < 10$  the resistivity is  $\eta = 1 \times 10^{-4}(r - 9)$ .

### 4.2.1 Disk and Planet Models

As an initial condition we take a gas disk in sub-Keplerian rotation around a solar mass star. The azimuthal velocity is given by

$$v_\phi = \sqrt{v_k^2 - c_s^2(a - 2b)}, \quad (4.4)$$

where  $v_k$  is the Keplerian velocity and  $a = 3/2$  and  $b = 0.5$  are the exponents of the radial power law distribution of the density  $\rho \propto r^{-a}$  and sound speed  $c_s = c_0(r \sin \theta)^{-b}$ . The initial density distribution is given by

$$\rho(r, \theta) = (r \sin \theta)^{-3/2} \exp\left(\frac{\sin \theta - 1}{c_0^2}\right). \quad (4.5)$$

The disk is described by a locally isothermal equation of state  $P = c_s^2 \rho$ . The ratio of the pressure scale height  $h$  to the radial coordinate of the disk is taken to be a constant such that  $h = H/(r \sin \theta) = 0.07$ .

The gravitational potential of the planet is given by a softened point-mass potential

$$\Phi_p(\mathbf{r}) = -\frac{GM}{(|\mathbf{r} - \mathbf{r}_p|^2 + \epsilon^2)^{1/2}} \quad (4.6)$$

where  $\epsilon$  is the softening parameter, needed to avoid numerical divergence near the position of the planet and

$$|\mathbf{r}_p - \mathbf{r}|^2 = r_p^2 + r^2 - 2r_p r (\sin \theta_p \sin \theta \cos(\phi_p - \phi) + \cos \theta_p \cos \theta) \quad (4.7)$$

is the distance between the planet and a gas particle in the disk. For all the simulations  $\epsilon$  is set to be a fraction of the Hill radius  $\epsilon = kr_p(M_p/3)^{1/3}$  with  $k < 0.5$ . Table 4.1 shows the parameters of our simulations. Distances are given in units of  $r_0 = 1AU$ , density is given in units of  $\rho_0 = 2.6 \times 10^{-10} gcm^{-3}$ , and velocity is given in units of Keplerian speed at  $1AU$ ,  $v_0 = v_k(1AU)$ . The surface density have been scaled such that the total disk mass is  $0.01M_{star}$ . Magnetic fields are given in units of  $B_0 = \sqrt{4\pi\rho_0 v_0^2}$ . In the cases where the planet is not on a fixed orbit (runs see Table 4.1), the equations of motion are integrated with a simple leap frog integrator. For the calculation of the torque, we include

## 4. 3D MHD SIMULATIONS OF PLANET MIGRATION IN TURBULENT STRATIFIED DISKS

---

Name	$q = M_p/M_\star$	$\epsilon(r_h)$	$r_p$	Fixed orbit	Run time (local orbits)
R0	Massless	0.3	3.3	Yes	130
R1	$5 \times 10^{-6}$	0.3	5.0	No	85
R2	$10^{-5}$	0.3	5.0	No	140
R3	$10^{-5}$	0.1	3.3	Yes	89
R4	$5 \times 10^{-5}$	0.3	5.0	No	90
R5	$10^{-4}$	0.3	5.0	No	100
R6	$10^{-4}$	0.1	3.3	Yes	135
R7	$10^{-4}$	0.3	4.0	No	85
R8	$2 \times 10^{-4}$	0.3	5.0	No	95
R9	$10^{-3}$	0.3	5.0	No	100
R10 (HD)	$10^{-3}$	0.3	5.0	No	100

**Table 4.1:** Simulation Parameters

the entire disk in the integration (without Hill sphere tapering, except for simulation R9). The components of the torque vector in cartesian coordinates are given by

$$\Gamma_i = GM_p \int \rho(\mathbf{r}) \frac{(\mathbf{r}_p \times \mathbf{r})_i}{(|\mathbf{r} - \mathbf{r}_p|^2 + \epsilon^2)^{3/2}} dV, \quad (4.8)$$

where  $i \in \{x, y, z\}$  is any of the three cartesian indices and  $(\mathbf{r}_p \times \mathbf{r})_i = (\mathbf{r}_p \times \mathbf{r}) \cdot \hat{e}_i$ , with  $\hat{e}_i$  being the cartesian unit vectors. Of course, for studying migration, we are mostly interested in the  $z$  component of the torque vector. Specific torques are given in units of  $v_k^2(1AU)$ .

### 4.2.2 Magnetic Field Configuration

Before introducing the planet in the simulations, a weak toroidal magnetic field is imposed on the disk given by

$$(B_r, B_\theta, B_\phi) = (0, 0, 2p/25), \quad (4.9)$$

where  $p$  is the initial thermal pressure. This gives an initial azimuthal field with constant plasma beta  $\beta = 25$ . The field is imposed in a subset of the full computational domain given by  $2 < r < 9$  and  $\pi/2 - 0.07 < \theta < \pi/2 + 0.07$ . The simulation is then followed until turbulence generated by the MRI has reached a saturated state. After this stage, we reset the density to the initial condition. This is the initial state in which the potential of the planet is incorporated and where all our runs start. The azimuthally, vertically and time averaged value of the effective  $\alpha$  parameter is shown in Figure 4.1. However, the  $\alpha$  stress is not constant throughout the vertical dimension. The upper layers of the disk are the most active. Figure 4.2 shows the time evolution of  $B_\phi$ ,  $B^2/B_0^2$  and  $\alpha$  for

simulation R0 (see Table 4.1) that does not include a planet. The top figure shows the characteristic butterfly diagram for the azimuthal component of the magnetic field in a turbulent stratified disk.<sup>1</sup>

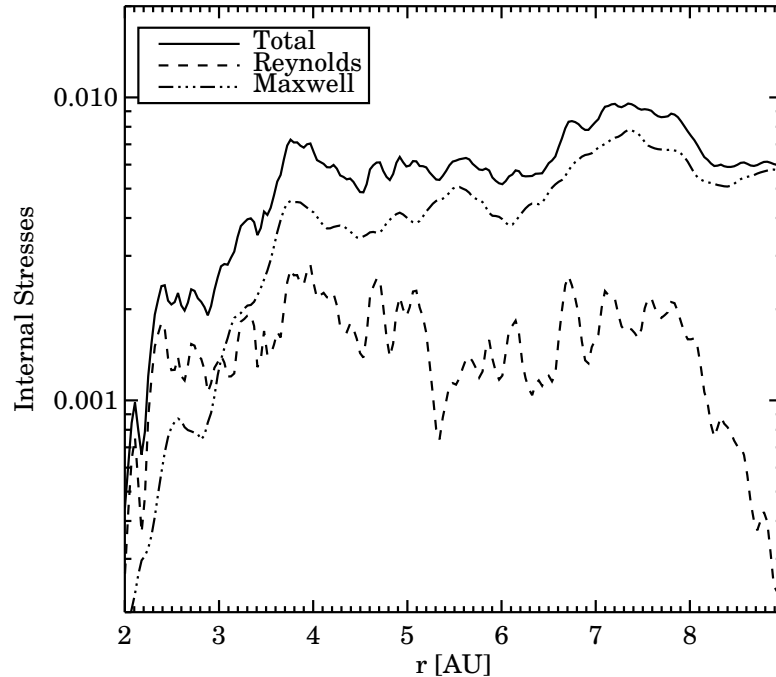


**Figure 4.1:** Initial radial distribution of the time, azimuthally and vertically averaged stress parameter (before the addition of the potential of the planet). The dashed and dashed-dot lines show the Reynolds  $T_{Rey}$  and Maxwell  $T_{Max}$  stresses respectively, normalized by the initial pressure. The solid line shows the total effective  $\alpha$  parameter.

#### 4.2.2.1 Zonal flows and pressure bumps

The time-averaged thermal and magnetic pressure and the perturbed (with respect to Keplerian) azimuthal velocity are plotted in Figure 4.3 for run R0. We plot these quantities in the mid-plane of the disk, and one scale height above the mid-plane, for a simulation without a planet (or, equivalently, a massless planet). The radial gradient of the pressure has been removed and the pressure is averaged in the azimuthal direction. As expected of zonal flows, we see pressure bumps that correlate with bumps in perturbed azimuthal velocity, only phase shifted by one quarter of a period (Johansen et al., 2009). Bumps in thermal pressure correlate with drops in magnetic pressure, a behavior that is seen more

<sup>1</sup>A more complete description of the type of model used in this chapter and a detailed analysis of the MRI, magnetic fields and turbulent spectra can be found in Flock et al. (2011).

## 4. 3D MHD SIMULATIONS OF PLANET MIGRATION IN TURBULENT STRATIFIED DISKS

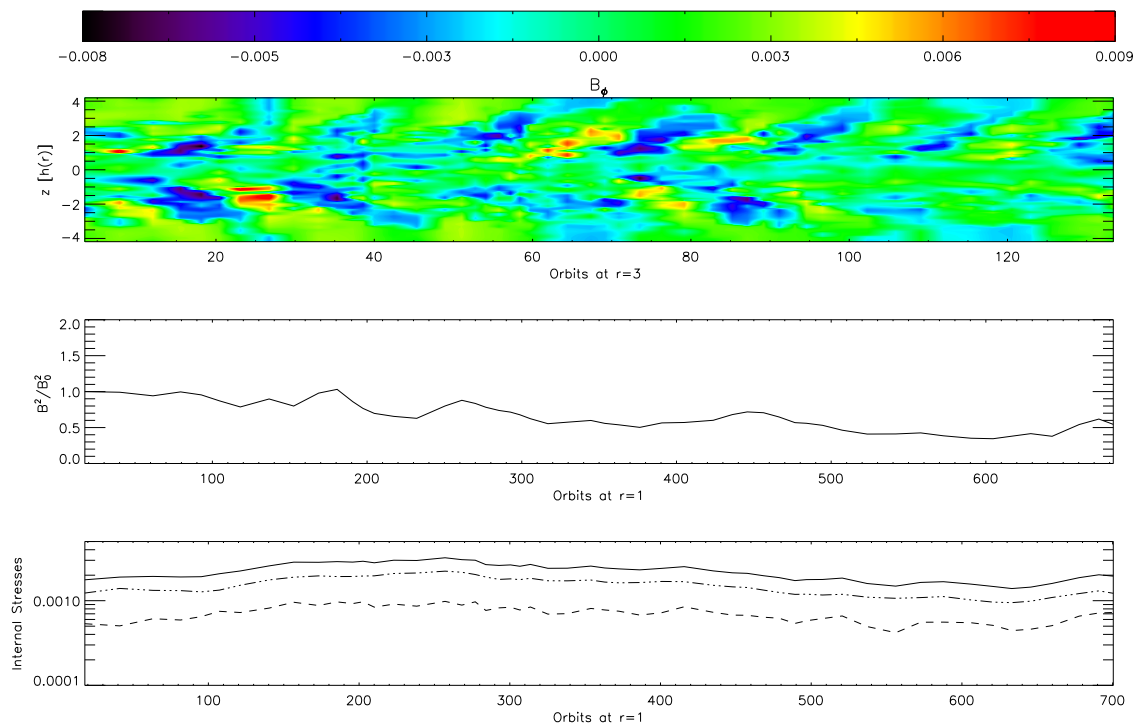


**Figure 4.2:** Time evolution of  $B_\phi$ ,  $B^2/B_0^2$  and  $\alpha$  for a run without a planet. The dashed and dashed-dotted lines show the Reynolds  $T_{Rey}$  and Maxwell  $T_{Max}$  stresses respectively, normalized to the initial pressure. The solid line shows the total effective  $\alpha$  parameter.

clearly above the mid-plane, since the MRI is not resolved in the mid-plane of the disk. Notice also that in the velocity peaks, the azimuthal velocity exceeds the Keplerian value at some radial locations. These structure in the pressure and the velocity lived for the entire duration of our simulations, around 1000 inner orbits. These "zonal flows" result from an inverse cascade of kinetic energy, e.g. a transport of energy from the MRI unstable medium scales, to the largest scales, which is very typical in accretion disks simulations (see for instance [Dzyurkevich et al. \(2010\)](#) and [Lyra et al. \(2008\)](#)).

### 4.3 Results

#### 4.3.1 Disk torques and migration

Table 4.1 summarizes the computational time in local planet orbits for each of the simulations. The torque was calculated by taking into account the entire disk and its value

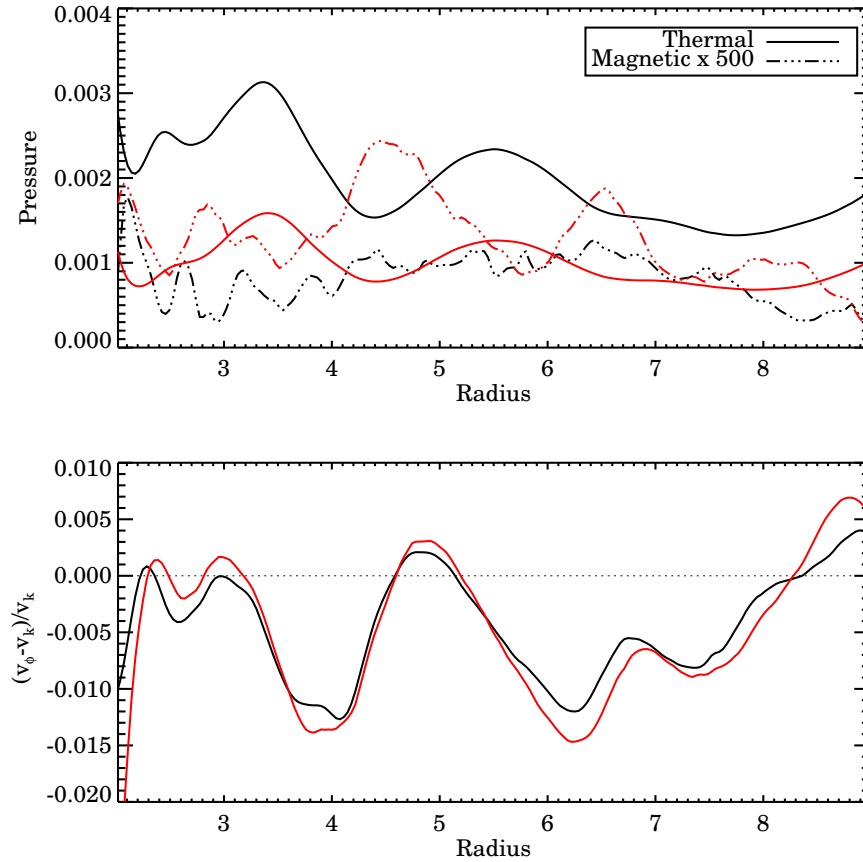


**Figure 4.3:** *Top figure:* Time-averaged thermal and magnetic pressure in the mid-plane (black line) and one scale height above the mid-plane (red line). The profiles have been normalized to take out the radial variation. *Bottom figure:* Azimuthal velocity perturbation (with respect to Keplerian speed) in the mid-plane (black line) and one scale height above the mid-plane (red line). This is from a simulation with no planet included.

was saved at every time step. We calculated the cumulative average specific torque as

$$\Gamma_n = \frac{1}{T_n} \sum_{k=1}^n \Gamma_k \Delta t_k, \quad (4.10)$$

where  $\Gamma_n$  is the cumulative average torque up to timestep  $n$  and  $T_n$  is the total time until timestep  $n$ .

#### 4.3.1.1 Low Mass Planets ( $q = 5 \times 10^{-6}$ and $q = 1 \times 10^{-5}$ )

Figure 4.4 summarizes the density structure of simulations R2, R5 and R9. Runs R1 ( $q = 5 \times 10^{-6}$ ), R2 and R3 ( $q = 10^{-5}$ ) shows no significant perturbation of the density

#### 4. 3D MHD SIMULATIONS OF PLANET MIGRATION IN TURBULENT STRATIFIED DISKS

---

by the planet, and no spiral arms are seen. The turbulent perturbations dominate in this case. Figure 4.5 shows the torque cumulative average torque as a function of local orbits for run R1. Figure 4.6 shows the torque for simulations R2 and R3. The fluctuations in the torque created by the perturbations in the density can, in both cases, be larger than the mean torque expected for standard Type I migration in a laminar disk. Comparing the torque for the planet at different positions in the disk, we see that the local (in time) evolution depends on the location of the planet. Random variations in the torque can be an order of magnitude larger than torques coming from the Lindblad resonances, in addition to the possibility that the spiral waves excited at Lindblad resonances are partly or totally suppressed by density fluctuations coming from the turbulence, such that the magnitude of this torque can be reduced. For the low-mass planet simulations, we find no convergence of the torque on timescale of the runs. For a run with a massless planet orbiting at  $r_p = 3.3$ , a gaussian fit of the time distribution of the torque gives a standard deviation of  $\sigma \approx 1.5e - 5$ . We also calculate the auto-correlation function of the torque and take the correlation time to be given by  $\tau_c = \int_0^{t^{max}} ACF(\tau) d\tau$ . This gives  $\tau_c \approx 2$  local orbits, while the first and second zero crossing of the torque ACF occur at 0.2 and 0.8 local orbits.<sup>1</sup> This is in agreement with results by Nelson (2005) and Fromang and Nelson (2009) and with estimates used by Baruteau and Lin (2010) that are based in previous MHD simulations of turbulent low-mass planet migration. We also calculate the power spectrum of the mid-plane density (see Eq. 3 in Baruteau and Lin (2010)). This is shown in Figure 4.7 and we compare our results from MHD simulations to Figure 1 of Baruteau and Lin (2010), where the spectrum in the result of the forcing model for the turbulence with  $\alpha \sim 10^{-3}$ . This comparison is valuable, since ultimately, a more complete parameter study migration and turbulence will have to be studied in models with forced turbulence. For this  $\alpha$  value, in our simulations we find that the larger scales carry more power than in the random forcing model, while the two spectrum agree for smaller scales for the case that includes the modes with  $m > 6$ . The higher power at larger scales can result from the higher compressibility of stratified disks, especially at large scales, as a vertically stratified disk can respond to compression with vertical expansion. However, the overall shape of the spectrum of the MHD simulation agrees better with the HD simulation without the  $m > 6$  modes included. Therefore with the proper scaling of the amplitude of the turbulence, and a cutoff of these modes, these simulations could reproduce the MHD spectrum. Another possibility is that the power at the small scales in the MHD simulation is lower due to lacking resolution at these scales. Ultimately, there needs to be a physical motivation for the cutoff of the turbulent forcing potential

---

<sup>1</sup>The calculation of the torque standard deviation and the torque correlation time is done as an averaging over a set of massless particles that sample the torque at different locations in the disk. This provides a characterization of the stochastic torque in an unperturbed disk. A more detailed description of this topic is presented in Appendix A

after the first few modes, if this is indeed the model that better matches the global MHD simulations.

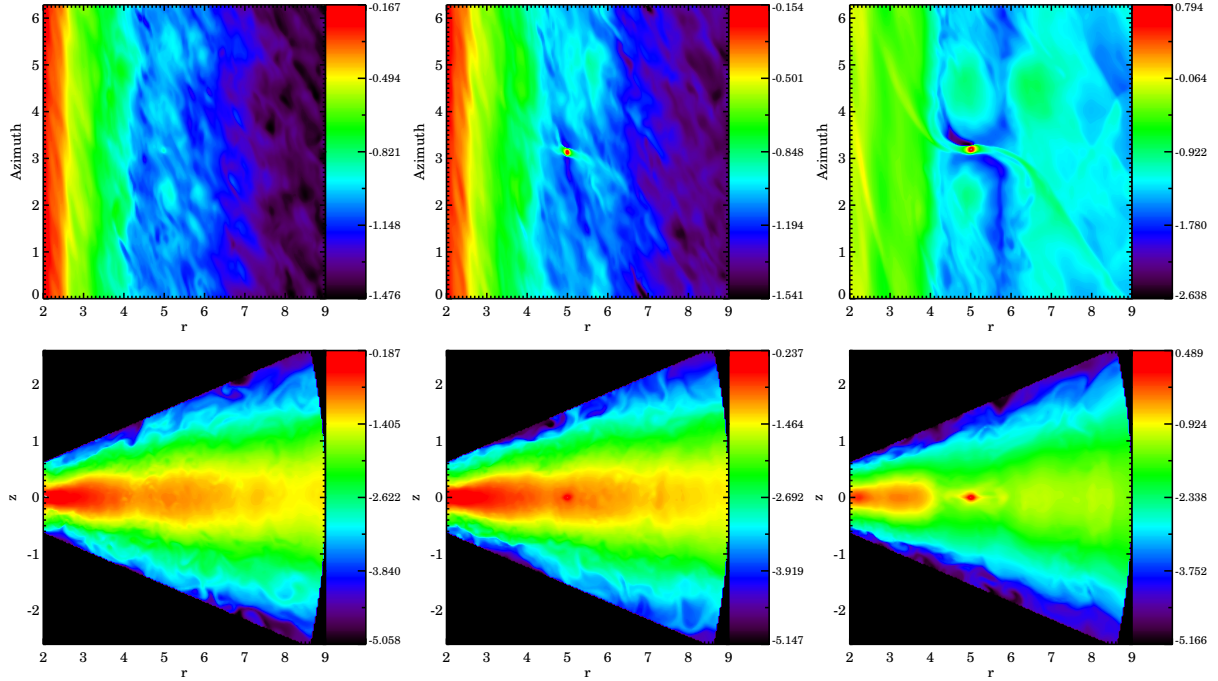


**Figure 4.4:** Logarithm of the disk density in the mid plane (top row) and in an azimuthal cut at the position of the planet (bottom row) for runs R2 (left,  $q = 10^{-5}$ ), R5 (middle,  $q = 10^{-4}$ ) and R9 (right,  $q = 10^{-3}$ ).

#### 4.3.1.2 Intermediate Mass Planets ( $q = 5 \times 10^{-5}$ , $q = 1 \times 10^{-4}$ and $q = 2 \times 10^{-4}$ )

Figure 4.4 shows the log density for run R5. For this simulation ( $q = 10^{-4}$ ), spiral arms are visible and their amplitude is comparable (or larger closer to the planet) to that of the perturbations generated by the turbulence. Figure 4.8 shows the cumulative average specific torque for run R4 and Figure 4.9 shows the torque for simulations R5 and R6. We see that in these three simulations there is an initial stage where the torque is negative followed by a reversal of the direction of the migration where the torque becomes positive and takes a defined value for the rest of the simulation. This happens at different times when we compare two different positions of the planet in the disk (runs R5 and R6). Instead of a random walk variation in semi major axis superimposed on smooth inwards migration, we find that planets of around 30 Earth masses undergo systematic outward migration. This outward migration is sustained for the total duration of the simulation. The simulation times for runs R5 and R6 are around 600 to 1000 orbits at the inner boundary of the disk (1AU). During this time, the density profile in the disk can evolve

#### 4. 3D MHD SIMULATIONS OF PLANET MIGRATION IN TURBULENT STRATIFIED DISKS

---

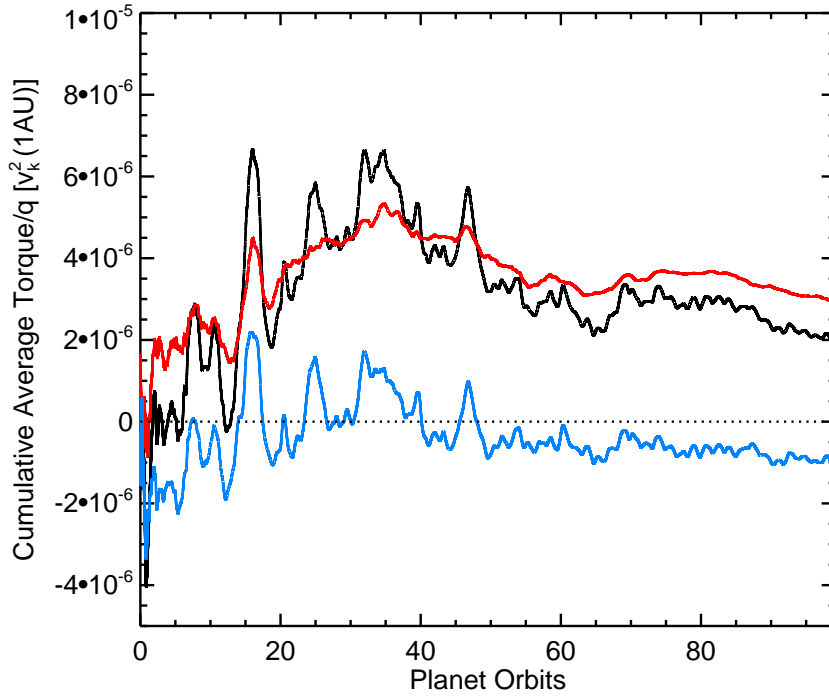


**Figure 4.5:** Cumulative average torque for run R1 for  $q = 5 \times 10^{-6}$ . The red and blue lines show the torque exerted by the inner and outer disk respectively.

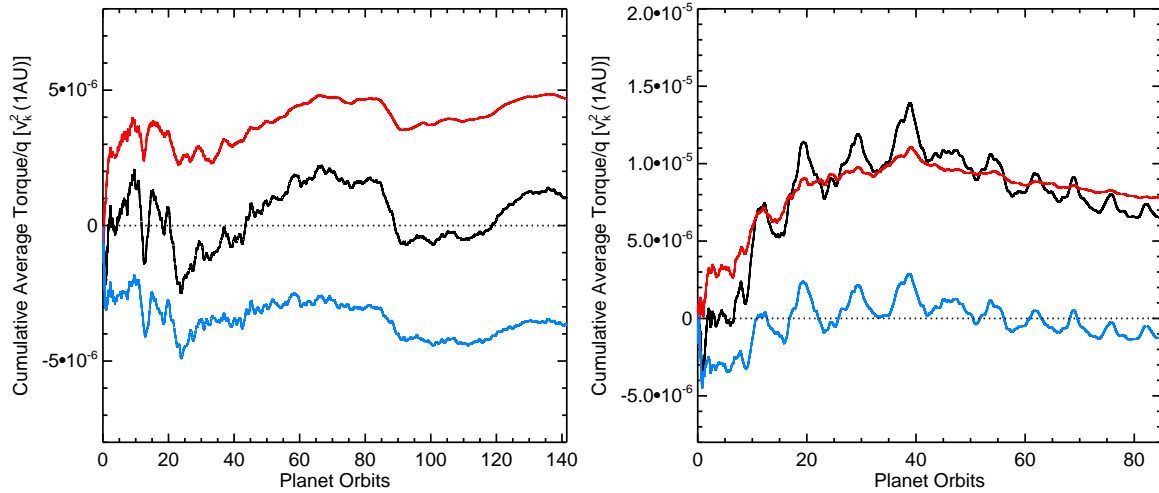


**Figure 4.6:** Cumulative average torque for runs R2 and R3, for  $q = 10^{-5}$ , where the planet is located at  $r_p = 3.3$  and  $r_p = 5.0$  respectively. The red and blue lines show the torque exerted by the inner and outer disk, respectively.

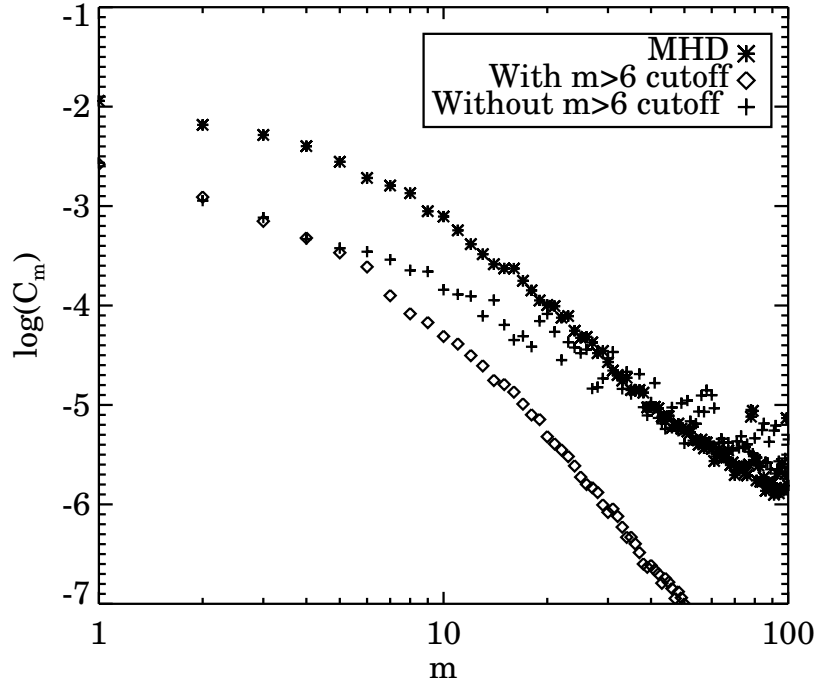


**Figure 4.7:** Power spectrum of the surface density, averaged in time and azimuthally, from MHD simulation (*stars*). We compare with the power spectrum that results from the turbulent model of Baruteau and Lin (2010) used in HD simulations, with (*triangles*) and without (*crosses*) the cutoff of the modes with  $m > 6$ , and with effective  $\alpha \sim 10^{-3}$ .

significantly from the initial state, and although the surface density profile can still be fitted by the initial profile ( $\Sigma \propto r^{-1/2}$ ), there can be changes in the local profile at the position of the planet and accumulation of mass at the disk inside the planet’s orbit due to turbulent stresses. However, for both simulations, the torque is reversed before there is a significant accumulation of mass at the inner boundary and it converges to a constant value for the remaining simulation time. The torque for run R8 is shown in Figure 4.11. In this run the planet mass ( $q = 2 \times 10^{-4}$ ) is now able to modify the density profile around its orbit, and opens a partial gap, which affects the convergence of the torque. We don’t find convergence for the simulation time, but there is still a tendency for outwards migration.

Unlike the simulations for the small-mass planets (R1, R2 and R3), for the simulations R4, R5 and R6, the hill radius of the planet and the horseshoe region are resolved (by approximately 4, 4 and 7 grid cells per half width respectively). In this case, the component of the torque originating from the horseshoe region can dominate if there is a mechanism for keeping the corotation torque unsaturated and the local density profile differs from

#### 4. 3D MHD SIMULATIONS OF PLANET MIGRATION IN TURBULENT STRATIFIED DISKS

---

the global profile, possibly increasing outwards, such that the corotation torque can be larger than the Lindblad torque, making the total torque positive. There are special locations in the disk where it is possible for the surface density to increase outwards, due to the appearance of zonal flows, as seen in Section 4.2.2.1.

Comparing the torque values of the simulations with analytical estimates by [Paardekooper and Papaloizou \(2009a\)](#) or [Masset et al. \(2006a\)](#) is not straightforward. First, the undergoing evolution of the disk can make the surface density profile at the position of the planet and the effective stress resulting from turbulence vary in time, therefore one torque estimate does not apply at all times. On the other hand, the value of the horseshoe drag is very sensitive to the structure of the horseshoe region, and the estimate used in the analytical calculations is based on a 2D model of the flow around the planet. In our case, the horseshoe region is distorted, making the half-width difficult to define. Additionally, the inclusion of magnetic fields can introduce new magnetic resonances that affect the total torque, as seen by [Terquem \(2003\)](#) and [Fromang et al. \(2005\)](#) for a uniform non-turbulent field. For the sake of the comparison and simplicity, we discard this type of contribution. We attempt a comparison with the analytical estimates for the torque, including a contribution of the horseshoe drag. We take the total torque to be composed of the Lindblad torque in a 3D locally isothermal disk ([Tanaka et al., 2002](#))

$$\Gamma_{Lind} = -(2.340 - 0.099a + 0.418b) \left(\frac{q}{h_p}\right)^2 \Sigma_p r_p^4 \Omega_p^2, \quad (4.11)$$

plus the fully unsaturated non-linear horseshoe drag<sup>1</sup> ([Paardekooper and Papaloizou, 2009a](#))

$$\Gamma_{HS} = \frac{3}{4} \left(\frac{3}{2} - a\right) x_s^4 \Sigma_p r_p^4 \Omega_p^2. \quad (4.12)$$

Here  $\Omega_p$  is the angular frequency of the planet and  $\Sigma_p$  is the surface density at the position of the planet. The cumulative average torque at the end of the simulation for run R5 is  $2.0 \times 10^{-5}$  and we take the half width of the horseshoe region to be  $x_s = 0.25$ , as is measured in our simulations (calculated from the analytical expression,  $x_s = 0.24$ ). Assuming the global surface density profile  $\Sigma \propto r^{-d}$ , with  $d = 0.5$ , will always give a negative torque. However, the torque always becomes positive for  $d = 0.3$  and matches the simulation value for  $d = -1.5$ , which is comparable to the local profile observed in the simulations (see middle plot in Figure 4.12). We should also note that already a "close-to-flat" profile can significantly reduce the negative torque or change the sign of the torque. For simulation R6, the cumulative average torque at the end of the simulation

---

<sup>1</sup>We take the expression for an isothermal disk, in the zero gravitational softening limit.

is  $3.7 \times 10^{-6}$  and the measured half width of the horseshoe region is  $x_s = 0.16$ . In this case, a local profile of  $d = 0.1$  is enough to obtain a positive torque, while a local profile of  $d = -0.4$  matches the value of the torque obtained in the simulation. However for this simulation, we only observe a flatter profile (see Figure 4.12). This discrepancy can be due to the fact that these values are very sensitive to the value of  $x_s$ , since the horseshoe drag scales as  $x_s^4$ , and we stress that the streamlines can be very distorted, therefore making the estimation of  $x_s$  difficult. This is a critical parameter, and we find that an increase of 1% to 5% in the simulation value of  $x_s$  with respect to the analytical estimation is enough to reproduce the observed positive torques. Therefore, if one assumes that the observed torque is composed of the wave torque plus the corotation torque and neglects any additional effect, we see that the corotation torque is crucial and able to cancel out or overcome the negative Lindblad contribution for standard disk parameters.

To further test the effect of the local density profile, we performed a simulation with  $q = 10^{-4}$ , for the planet located at  $r_p = 4.0$  (run R7, Figure 4.10), initially at the right side of a pressure bump (where pressure and density decrease with radius). In this case, the cumulative average torque does not clearly converge, and we do not see systematic outwards migration, as the cumulative average torque approaches zero. However there is still a significant reduction of the torque as compared to the Type I Lindblad torque, which cannot be explained only in terms of a locally decreasing radial density profile. This result suggest that even in the absence of a pressure bump, inwards migration can be significantly slowed down for this planet mass. We note also that we used the expression for the horseshoe drag valid for an isothermal disk, so that there is an additional contribution due to the locally isothermal profile that we did not take into account.

To see if the transport of mass in the disk is enough to sustain the unsaturated torque, we take the expression for the minimal  $\alpha$  to maintain the unsaturated corotation torque (Masset et al., 2006a)

$$\alpha_m = 0.035q^{3/2}h^{-7/2}, \quad (4.13)$$

we obtain  $\alpha_m = 0.0003$  for  $q = 10^{-4}$ , which is always smaller than what we observe in our simulations<sup>1</sup> (comparing with the volume average  $\alpha$ ). For run R6 we also observed that in comparison to a purely HD laminar run, in which the planet is able to open a partial gap in the disk, the gap in this case is less deep than in the HD case, and also wider, compared to the narrower gap seen in the laminar simulation. For run R5, there was no gap opening neither in the laminar nor the turbulent runs as the gap opening criterion is not satisfied. We also find that the stresses in the disk are affected by the presence of the planet; the volume averaged stress decreases as the mass of the planet is increased (see top and middle plots in Figure 4.13), which might be a result of numerical dissipation

---

<sup>1</sup>However, this expression for  $\alpha_m$  is derived using a 2D model of the HS region, which determines the viscous crossing time across the region, the libration time and the U-turn time.

#### 4. 3D MHD SIMULATIONS OF PLANET MIGRATION IN TURBULENT STRATIFIED DISKS

---

due to the limited resolution.

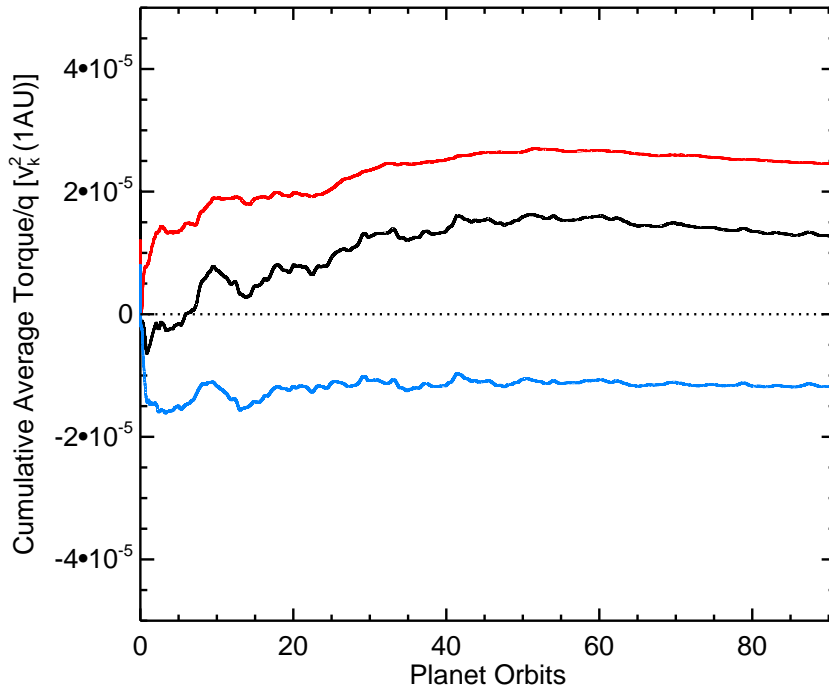


**Figure 4.8:** Cumulative average torque for run R4 for  $q = 5 \times 10^{-5}$ . The red and blue lines show the torque exerted by the inner and outer disk respectively.

##### 4.3.1.3 Large Mass Planet ( $q = 10^{-3}$ )

The density structure and spiral arms induced by the Jupiter mass planet in run R9 ( $q = 10^{-3}$ ) dominate over the turbulent perturbations and influences the entire disk. Figure 4.14 shows the cumulative average torque. We have excluded the torques coming from the Hill sphere for the calculation of the torque, to exclude material bound to the planet which is not properly simulated at this resolution or without including other relevant effects. For these simulations, initially we see the same trend as for runs R5 and R6, where the torque becomes positive, however this is not sustained for this planet mass as torques coming from the corotation region are suppressed due to gap opening (see bottom plot in Figure 4.12 and the right panels in Figure 4.4). Additionally, the planet modifies the stresses in the disk, and therefore, the accretion behavior, as can be seen in the bottom plot in Figure 4.13, that shows the evolution of the stresses for run R9. In this case, the  $\alpha$  stress is progressively suppressed and the Reynolds stress dominates the total stress. The reduction of the Maxwell stress is seen mostly in the part of the

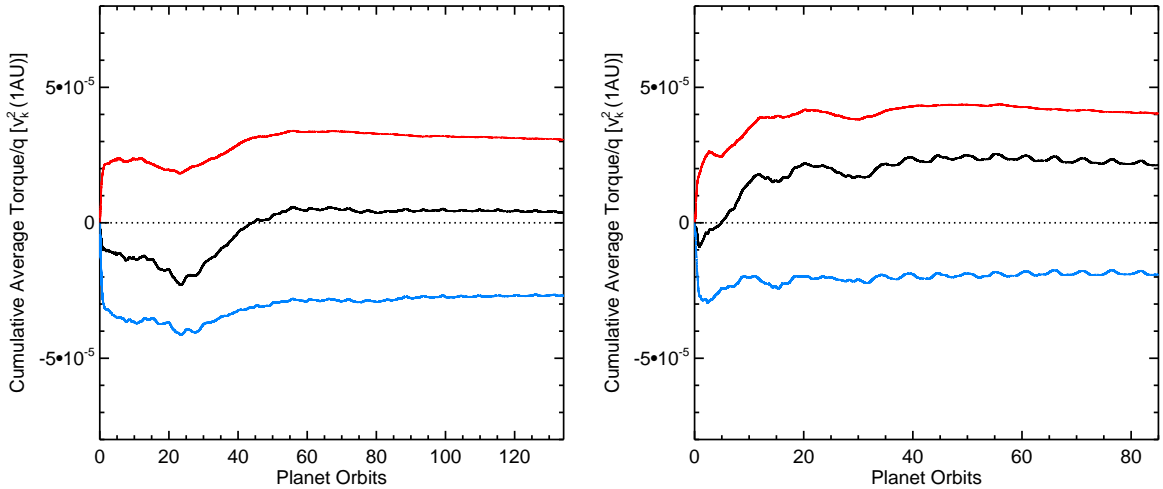


**Figure 4.9:** Cumulative average torque for runs R5 and R6, for  $q = 10^{-4}$ , where the planet is located at  $r_p = 3.3$  and  $r_p = 5.0$  respectively. The red and blue lines show the torque exerted by the inner and outer disk, respectively.

disk inside the planet’s orbit and in the gap region (see Figure 4.15). Is possible that the magnetic stress is suppressed in the gap region due to the modified azimuthal velocity near the planet, which can suppress the MRI locally. Notice that for this run, the density has a more laminar appearance (see Figure 4.4), consistent with a reduction of the stress due to the presence of the planet. This could also be a numerical effect that appears at this resolution, so further studies at higher resolution are needed.

In Figure 4.16 we compare the gap opened by the Jupiter mass planet in a magnetized disk (run R9) with an equivalent HD 3D simulation with  $\alpha$  viscosity where  $\alpha = 2 \times 10^{-3}$  (run R10) and stratification. The time of the snapshots is 100 local orbits. The gap for the hydro case is narrower and slightly deeper than the gap formed in the magnetized turbulent disk. However the gap is not completely cleaned after this time. We observed the same characteristics for lower-mass planets that open only a partial gap in the disk. [Winters et al. \(2003\)](#) studied a similar case of gap opening, but in a unstratified MHD-turbulent disk. In agreement with our results, they found a wider gap when the disk is turbulent, and larger transport of mass from the outer to the inner disk (see our Figure 4.16). In contrast to our findings, they find a deeper gap in the hydro case. This can be due to a different treatment of the gap opening criteria, since the planet mass in their calculations does not satisfy the viscous criterion. In terms of the reduction of the stresses around the planet, we find agreement with their results.

[Nelson and Papaloizou \(2003\)](#) studied gap opening by a giant planet in an MHD-turbulent unstratified disk and compared their results with 2D simulations with an  $\alpha$  viscosity. They

#### 4. 3D MHD SIMULATIONS OF PLANET MIGRATION IN TURBULENT STRATIFIED DISKS

---

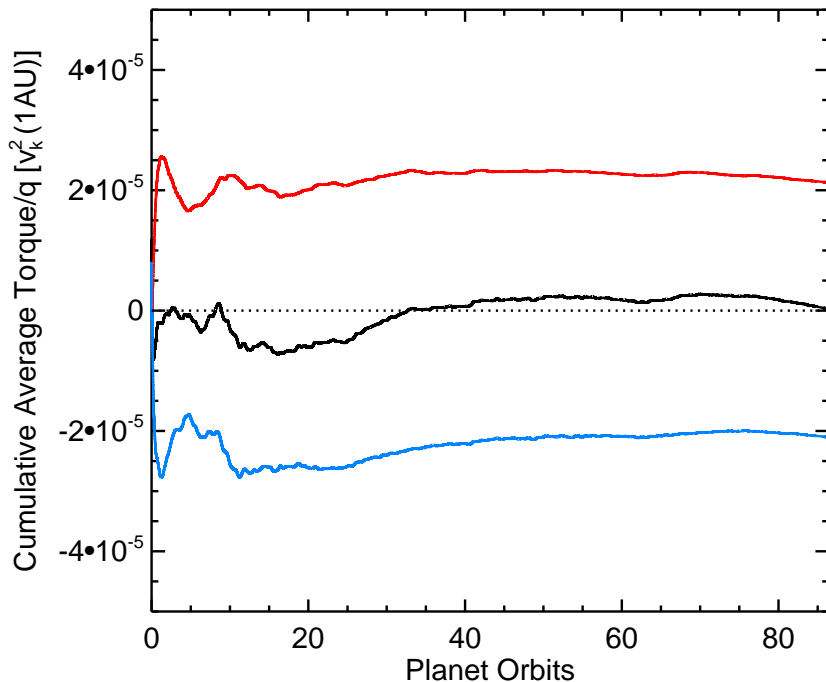


**Figure 4.10:** Cumulative average torque for run R7 for  $q = 10^{-4}$ , for the planet located at  $r_p = 4.0$ , initially at the right side of a pressure bump. The red and blue lines show the torque exerted by the inner and outer disk respectively.

found that a run with an equivalent  $\alpha$  stress to the turbulent run produced a shallower gap. This is different to our own results where we found the same gap depth. However, we should note they only studied how the turbulence affects an already formed gap and did not observe the depletion of the outer disk. The difference to our simulation results could also be due to our choice of  $\alpha$  in the hydro run. We choose an  $\alpha$  matching the global average of the turbulent runs, but this is a quantity that varies vertically. In a non-stratified disk simulation, this averaging is not necessary.

#### 4.4 Discussion and conclusions

For simulations R1, R2 and R3, where  $q = 10^{-5}$ , during the simulated time, migration was dominated by random fluctuations in the torque, that can be orders of magnitude larger than what is expected for the value of the Lindblad or corotation torques for this planet mass. This is in agreement with simulations by Nelson (2005) of migration of low-mass protoplanets in cylindrical disk models, where stratification is neglected. It is unclear if after long term averaging ( $\sim 1000$  orbits), the fluctuations will average out to zero while

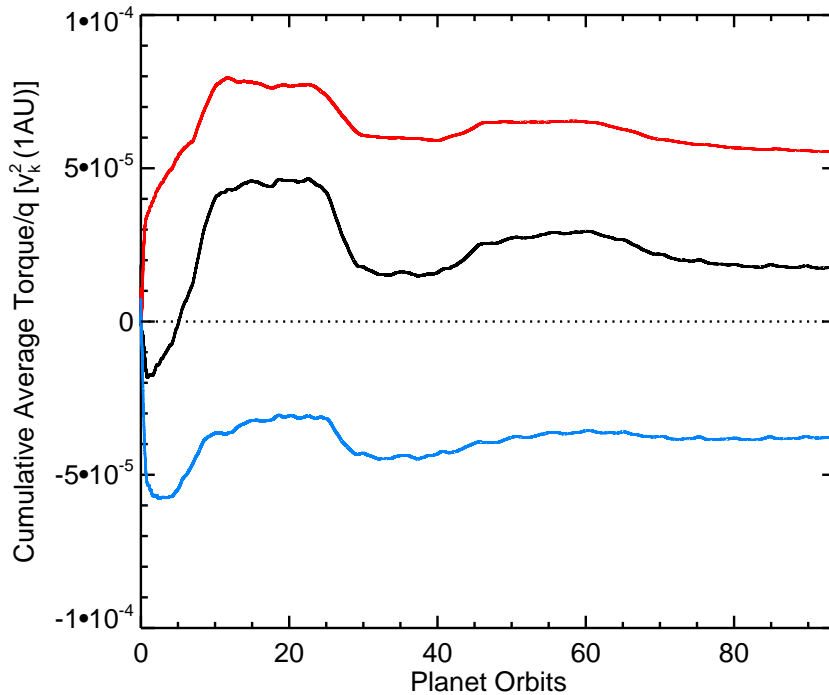


**Figure 4.11:** Cumulative average torque for run R8 for  $q = 2 \times 10^{-4}$ . The red and blue lines show the torque exerted by the inner and outer disk respectively.

some component of the systematic torque will remain. Such a calculation is currently too expensive. It will also be difficult to get a steady state without special prescriptions for correcting the density, due to the accretion evolution of the disk, in addition to the decrease in  $\alpha$  stress for long simulation times due to the limited resolution. Another interesting point for further studies is to investigate this type of migration with enough resolution to resolve the corotation region, to see the impact of the corotation torque in these cases. However, even if this torque is present and well resolved, its magnitude would still be small compared to the amplitude of the fluctuations, since ultimately the torque depends strongly on the width of the corotation region, which approaches zero as the planet mass approaches zero.

As the planet mass is increased by one order of magnitude to  $q = 10^{-4}$ , the hill radius is now properly resolved and the systematic torque is now large enough to dominate over the random component of the torque. Outwards migration in a locally isothermal disk can occur due to the viscosity unsaturating the torque coming from the corotation region (where the viscous timescale across the horseshoe region is smaller than the libration timescale), as was found by [Masset et al. \(2006a\)](#) for planets in the intermediate-mass

#### 4. 3D MHD SIMULATIONS OF PLANET MIGRATION IN TURBULENT STRATIFIED DISKS

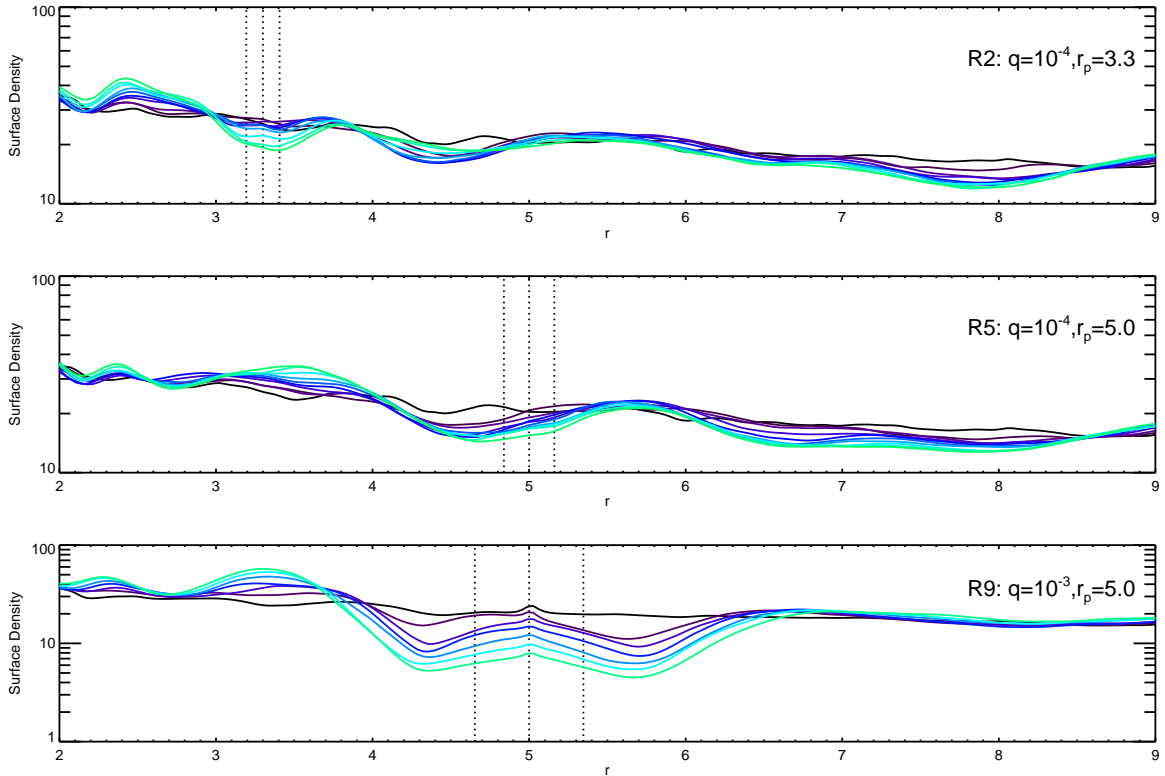


**Figure 4.12:** Surface density at different times in the simulation. Top, middle and bottom plot show the surface density for runs R2, R5 and R9 respectively. The vertical lines shows the position of the planet and the extent of the Hill radius.

range. Specifically, a planet with mass ratio  $q \approx 10^{-4}$  in a disk with  $h = 0.06$  with a flat surface density profile ( $d = 0$ ) and an  $\alpha$  viscosity was found to be the critical mass for which the offset from linear theory was the largest. Additionally, a planet mass of  $q = 10^{-4}$  is within the range of masses for which reversal of migration occurs, if one extrapolates their results to a disk with  $h = 0.07$ . However, this is the first study that observes the effect of the unsaturated corotation torque due to the accretion of mass in the disk provided directly by turbulence that has been self-generated by the MRI. For runs R4, R5 and R6, the planet is in locations in the disk where the local surface density profile is either close to flat or increasing outwards, due to the pressure bumps seen in Section 4.2.2.1. This can make the contribution of the corotation torque dominate over the Lindblad torque, which is usually unexpected in an  $\alpha$  disk, since for realistic density profiles, the Lindblad torque will dominate. This is also consistent with the torque in run R6 being initially negative, since at the beginning of the simulation the local profile is decreasing outwards, but getting shallower as time increases, eventually reaching the point where the torque reverses. For

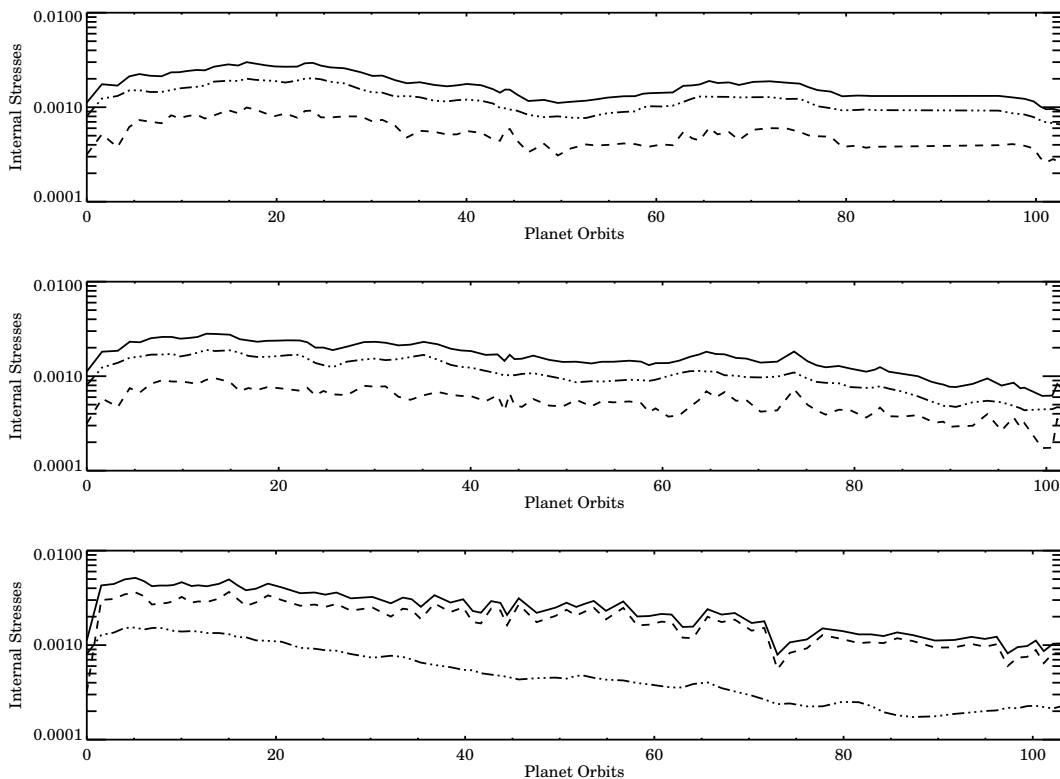


**Figure 4.13:** Time evolution of the stresses in a disk with an embedded planet. Top, middle and bottom plot show the stresses for runs R2, R5 and R9, respectively. The dashed and dashed-dotted lines show the Reynolds  $T_{Rey}$  and Maxwell  $T_{Max}$  stresses, respectively, normalized to the initial pressure. The solid line shows the total effective  $\alpha$  parameter.

run R5, the slope is almost immediately increasing outwards due to the evolution of the disk, which makes the torque positive from the beginning of the simulations. We can only roughly compare our numerical results with analytical estimates, as was done in the previous section, for the reasons described already there. Also in comparing with previous estimates, we also discarded any possible additional contributions to the torque that might arise because of the turbulent magnetic fields. The detailed structure of the horseshoe region in the presence of turbulence and stratification deserves further study. Our results are summarized on Figure 4.17, where the torque dependence on planet mass is shown. For each simulation, we plot the last value of the cumulative average torque. Note however that only for part of the simulations the torque converges to a well defined value. It is possible to see a trend of the torque to reverse, corresponding to the addition of the contribution of the fully unsaturated horseshoe drag ( $\Gamma_{tot} = \Gamma_{Lind} + \Gamma_{HS}$ ). For the plot we assumed values for the width of the horseshoe region that are 5% larger than the analytical estimate given by Paardekooper and Papaloizou (2009a) and we use the

#### 4. 3D MHD SIMULATIONS OF PLANET MIGRATION IN TURBULENT STRATIFIED DISKS

---

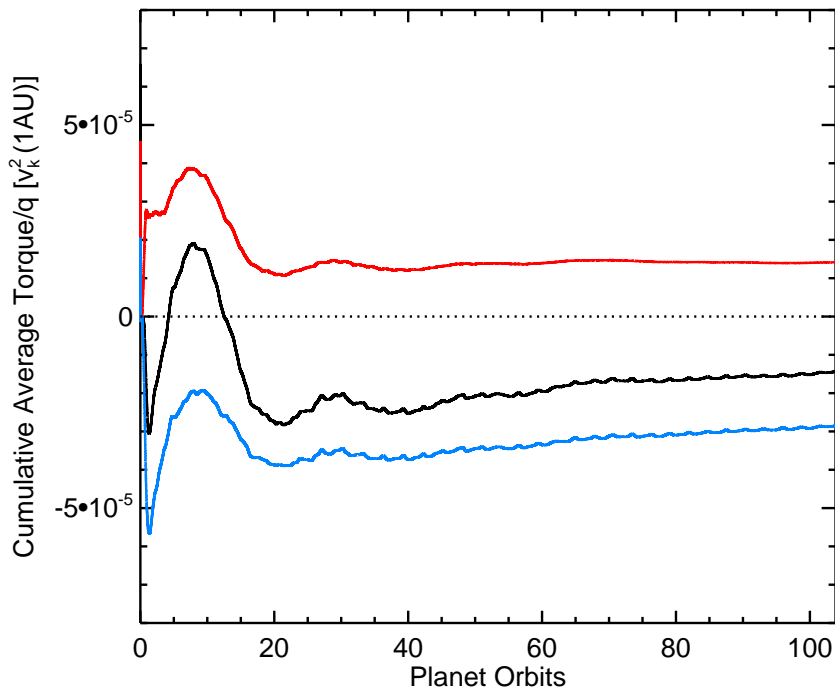


**Figure 4.14:** Cumulative average torque for run R9 for  $q = 10^{-3}$ . The red and blue lines show the torque exerted by the inner and outer disk respectively. The torque coming from the Hill sphere has been excluded from the calculation.

value of the local surface density profile for the calculation of the torque. We see that the trend breaks down already for  $q = 2 \times 10^{-4}$ , where gap opening starts to become important and there is a transition into the Type II regime. Error bars represent the standard deviation of the time distribution of the torque. Note that since the raw torque is a highly oscillating quantity, the standard deviation does not match directly to the amplitude of the turbulent fluctuations, especially in the high-mass planet cases. For run 10, the standard deviation was found to be only 20% lower than in the turbulent run R9. In the Type II range, we plot the torque corresponding to the viscous timescale of the disk, taking  $\alpha = 3 \times 10^{-3}$ . We find reasonable agreement with our simulation, taking into account the short simulation time, and that the value of the torque is still decreasing in the simulation after 100 orbits. Additionally we use the value of the initial, volume averaged  $\alpha$ , while the mid-plane value is smaller.

The question remains about the long term behavior of the torque, and whether this is only a transient behavior lasting for the first few hundred orbits (assuming the same local surface density profile), afterwards saturating and returning to standard negative Type I values. This is still a transient behavior in the sense that the planet can migrate out of the

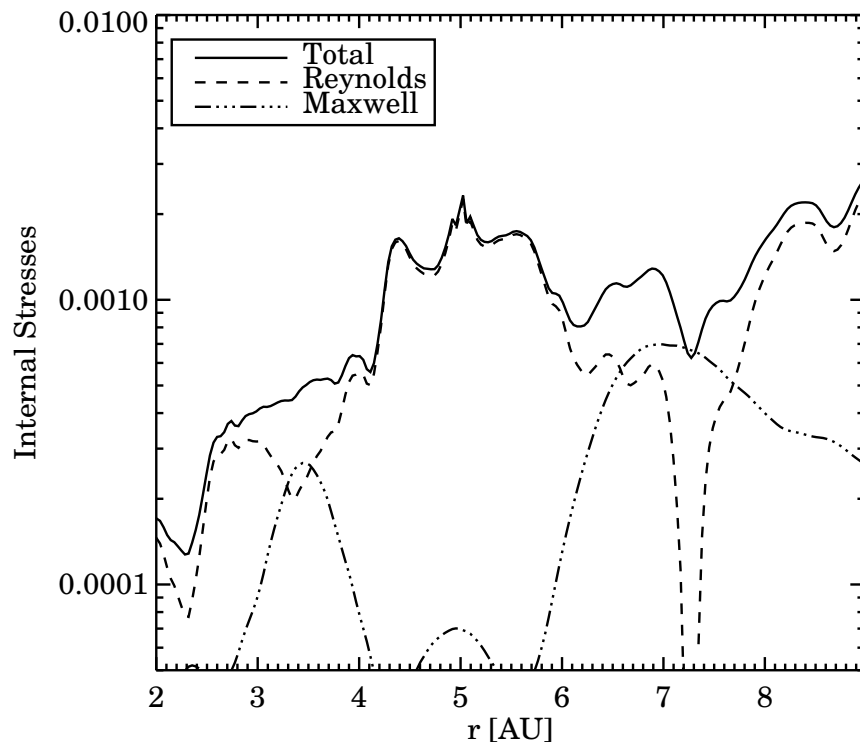


**Figure 4.15:** Radial distribution of the time, azimuthally and vertically averaged stress parameter for run R9. The dashed and dashed-dot lines show the Reynolds  $T_{Rey}$  and Maxwell  $T_{Max}$  stresses respectively, normalized by the initial pressure. The solid line shows the total effective  $\alpha$  parameter.

part of the disk where the local profile allows for outwards migration and enter a region where migration proceeds inwards again. Additionally it is limited by the lifetime of the pressure bumps, which we weren't able to determine. We observe a stable pressure bump through the duration of our simulations. If there are other mechanisms such as the ones discussed in [Masset et al. \(2006b\)](#) that produces this type of locally increasing outwards density profile, then, in the presence of turbulence, these density bumps can also act as a protoplanet trap and halt, slow down or reverse inwards migration. [Dzyurkevich et al. \(2010\)](#) performed non-ideal MHD simulations of accretion disks with spatially varying resistivity. They also find zonal flows/pressure bumps not only at the snow line, e.g. a region with a jump in resistivity, but also inside the more active region. They already suggest that small planets should get trapped at those local pressure maxima (see also [Kretke and Lin \(2007\)](#)).

#### 4. 3D MHD SIMULATIONS OF PLANET MIGRATION IN TURBULENT STRATIFIED DISKS

---

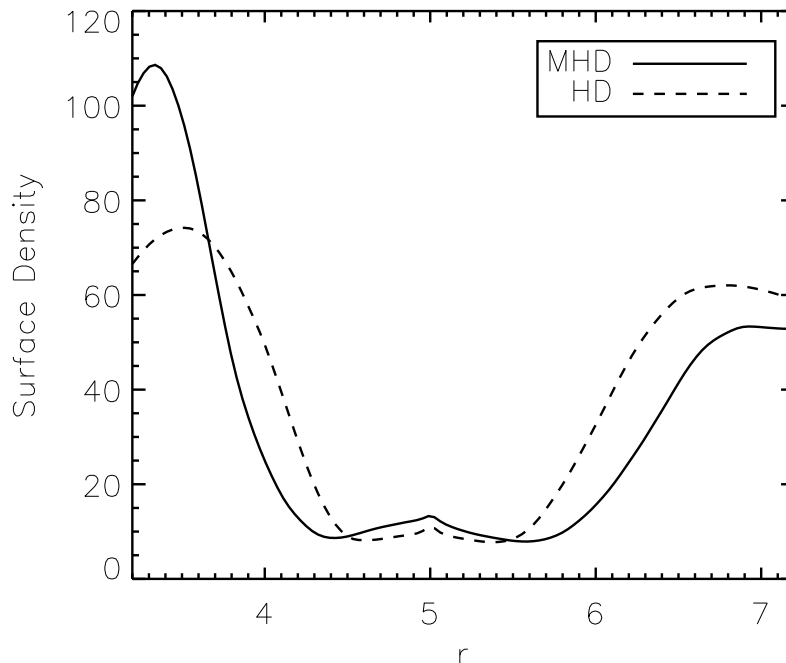


**Figure 4.16:** Gap comparison for run R9 ( $q = 10^{-3}$ ) and run 10, an equivalent HD simulation with  $\alpha = 2 \times 10^{-3}$ .

### 4.5 Summary

We studied the migration of planets under the influence of turbulence that is a result of the magneto-rotational instability. We find that, under the right conditions, planets can undergo systematic outwards migration in a locally isothermal disk. After long term averaging, transient or long term periods of outwards migration can help the survival and influence the mass accretion history of giant planet cores of a certain mass ratio. The contribution of the unsaturated horseshoe drag and the stochastic migration of low-mass planets, which are both consequences of the turbulence, should be incorporated into planet population synthesis models in order to test the influence of this element on the produced populations of planets. On future work we plan on studying low-mass planet migration in detail using similar stratified disk models.

Giant planets significantly decrease the magnetic stresses in the disk (mostly inside its orbit), effectively killing the turbulence, as we observe in our simulations. This is possibly a numerical effect and it will affect the accretion behavior of the disk and possibly the Type II migration rate of the giant planet. This issue deserves further study, with high

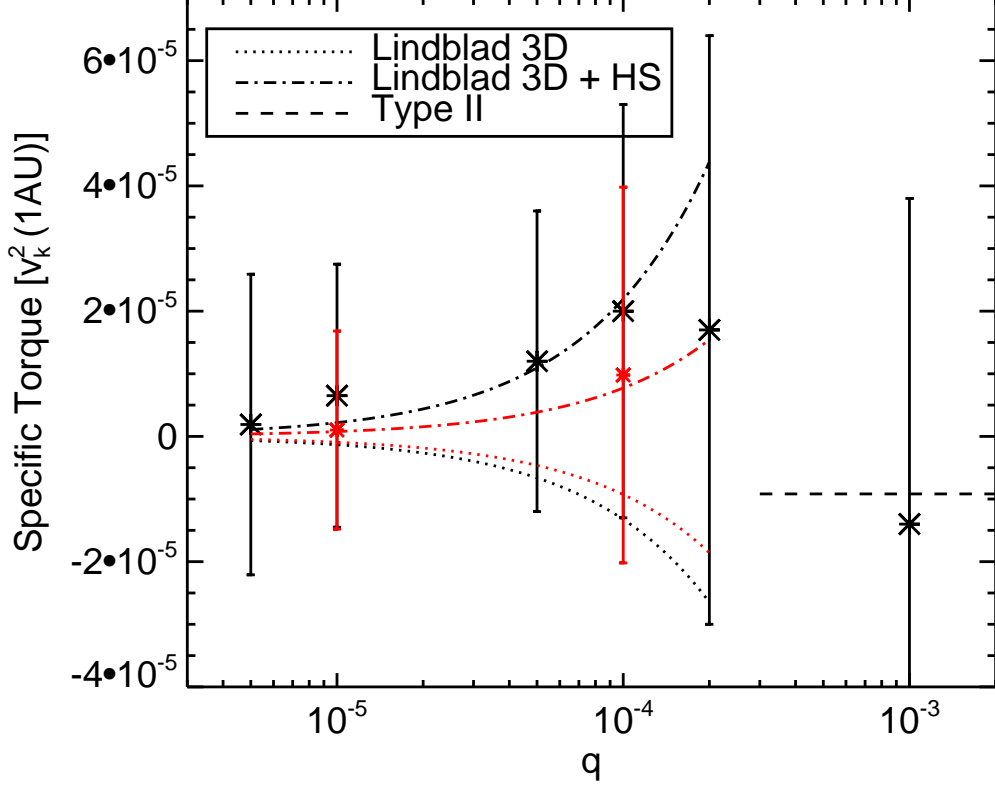


**Figure 4.17:** Specific torque as a function of  $q = M_p/M_s$ . The black symbols correspond to simulations R1, R2, R4, R5, R8 and R9, where the position of the planet is  $r_p = 5.0$ . The red symbols correspond to simulations R3 and R6, where the position of the planet is  $r_p = 3.3$ . In the  $q = 5 \times 10^{-6}$  to  $q = 2 \times 10^{-4}$  mass range, we overplot the analytical estimates for the torque, taking into account only the Lindblad contribution  $\Gamma_{tot} = \Gamma_{Lind}$  (dotted line) and both the Lindblad plus the unsaturated horseshoe drag  $\Gamma_{tot} = \Gamma_{Lind} + \Gamma_{HS}$  (dash-dotted line), for both positions (i.e. local surface density profiles) of the planet,  $r_p = 5.0$  (black line) and  $r_p = 3.3$  (red line). For the analytical expressions of the torque, we take the half-width of the horseshoe region to be 5% larger than its analytical estimate. The dashed line corresponds to the constant Type II migration rate, given by the viscous transport in the disk, using  $\alpha = 2 \times 10^{-3}$ . Error bars represent the standard deviation of the torque time distribution.

resolution simulations to determine any possible effects of numerical dissipation of the magnetic fields induced by the presence of the planet. Additionally, in agreement with previous studies, we find that the gap opened by a planet in the presence of turbulence is wider than the gap produced in a quasi-laminar disk with an equivalent  $\alpha$  viscosity.

#### 4. 3D MHD SIMULATIONS OF PLANET MIGRATION IN TURBULENT STRATIFIED DISKS

---

# Accretion of gas onto giant planets and envelope structure in magnetized turbulent disks

*We have performed three-dimensional magneto-hydrodynamical simulations of accretion disks, using the PLUTO code, and studied the accretion of gas onto a Jupiter-mass planet after opening a gap in the disk. We compare our results with simulations of laminar, yet viscous disks with different levels of an  $\alpha$  viscosity. A Jupiter mass planet is known to reduce the magnetic stress in the disk to around 10% of the unperturbed value. We find that this low levels of MRI-turbulence in protoplanetary disks do not enhance mass accretion onto the planet, and in fact might slightly suppress accretion, as compared to the case of a laminar viscous disk with comparable  $\alpha$  parameter. In all cases, the accretion flow accross the surface of the Hill sphere of the planet is not spherically or azimuthally symmetric, and is predominantly restricted to the mid-plane of the disk. Even in the turbulent case, we find no vertical flow of mass into the Hill sphere. Accretion rates are best approximated analytically by using the reduced density in the gap region. This means that the gap-opening planet never reaches an accretion rate as high as the one given by the unperturbed density of the disk. For a simulation of a magnetized turbulent disk, where the global averaged alpha stress is  $\alpha_{MHD} = 1 \times 10^{-3}$ , we find the accretion rate onto the planet to be  $\dot{M} = 6 \times 10^{-7} M_J yr^{-1}$ .*

## 5. ACCRETION OF GAS ONTO GIANT PLANETS AND ENVELOPE STRUCTURE IN MAGNETIZED TURBULENT DISKS

---

### 5.1 Introduction

Studying how planets accrete gas from circumstellar disks is necessary to estimate a limit on the mass of giant gaseous planets depending on the disk properties such as density and viscosity. It is also necessary to estimate the timescales for gas accretion (Alibert et al., 2004). In general one should take into account the effects of migration, gap formation and the viscous evolution of the disk.

In the inner parts of disks, gas giants can form as a result of core formation by planetesimal accretion followed by formation of the gas envelope by gas accretion from the circumstellar disk. Pollack et al. (1996) distinguished three phases in the formation using numerical simulations of core accretion and envelope evolution. A first phase marked by the fast accretion of solids unto a core until the feeding zone of the planet is mostly evacuated (Stevenson, 1982). A second phase where gas and solids accretion is low and constant. Finally, a third stage when the core mass equals the envelope mass, leading to the contraction of the envelope and the onset of runaway gas accretion (Mizuno, 1980). Migration of the planet might allow for an extension of the feeding zone, while gap formation might lead to a mass limit for gap opening planets (Alibert et al., 2005). In the outer parts of the disk, giant planets could form as a result of the collapse of a gravitationally unstable disk clump. This mechanism requires a very massive disk that can cool effectively on timescales of a few local orbital periods (Boss, 1997; Durisen et al., 2007; Mayer et al., 2002; Rafikov, 2005).

Planet population synthesis models produce synthetic populations of extrasolar planets, with a large diversity of initial conditions. These models have been successful in reproducing key features of the observed distribution of exoplanets (Benz et al., 2008; Ida and Lin, 2008; Mordasini et al., 2009a,b). The calculations usually include one-dimensional disk evolution and core/envelope structure models. The accretion of planetesimals and gas onto an already formed proto-core is included, using a given prescription for the accretion rates of gas and rocky materials onto the planet (Alibert et al., 2004). For this reason, an accurate estimation and parameterization of the accretion rates of gas onto planets for a variety of conditions is necessary to correctly calculate the formation time and the limiting mass of the giant planetary population.

#### 5.1.1 Modeling planet accretion

The accretion of gas onto planets has been modelled using two different approaches. On one side, one dimensional models have been used to calculate the radial structure of the envelope and the accretion onto a rocky core. This models can include effects such as the dust opacity of the envelope, the release of energy of infalling planetesimals into the envelope and the thermal feedback of the planet (Hubickyj et al., 2005; Ikoma et al., 2000).

These models can only include the disk evolution in a restricted way, and assume a certain model of the outer envelope (as a boundary condition) that is spherically symmetric.

On the other hand, two/three-dimensional simulations of accretion disk with accreting planets aim to estimate the structure of the flow around the planet and how much mass is the disk capable of feeding to the planet. However, most of these simulations miss the radiative feedback from the planet and a detailed model of the inner envelope. [D'Angelo et al. \(2003a,b\)](#); [Tanigawa and Watanabe \(2002\)](#) used high resolution two-dimensional simulations to study the detailed flow pattern around the planet, and the circumplanetary disk. They showed that inside the planets Roche lobe, accretion in the circumplanetary disk is powered mainly by energy dissipation of circulating matter at the spiral shock. Outside the Roche lobe, gas flows into the planet through "accretion bands" located between the horseshoe flow and the passing-by flow (although the detailed structure depends strongly on the sound speed). The accretion timescale

$$\tau_{acc} = \frac{M_p}{\dot{M}_p}, \quad (5.1)$$

has been measured to be around  $10^4 - 10^5$  yr, and the accretion rate of a Jupiter-mass planet has been found to be on the order of  $10^{-5} M_J / yr$  on a disk with  $M_d = 0.01 M_\odot$  ([Bate et al., 2003](#); [Bryden et al., 1999](#); [Kley et al., 2001](#); [Lubow et al., 1999](#)). Three-dimensional simulations including radiation transfer have found similar accretion rates and have shown the formation of a thick ( $H/r \approx 0.5$ ) circumplanetary disk ([Klahr and Kley, 2006](#)).

In this chapter we take the second approach and study the accretion rate of gas onto giant gap-opening planets in turbulent magnetized disks using three-dimensional global disk simulations. The turbulence in the disk is generated by the magneto-rotational instability ([Balbus and Hawley, 1991](#)). We compare the accretion rate of a planet in a turbulent disk with that in a viscous laminar disk and we examine the accretion structure and mass inflow into the Hill sphere of the planet, where material is assumed to be gravitationally bound to the planet. The chapter is organized as follows. In Section 2, we describe the computational setup, boundary and initial conditions, and the parameters we use in our simulations. We also describe the prescription for the mass accretion onto the planet. In Section 3.1, we present our results on the three-dimensional structure of the accretion flow into the Hill sphere. Section 3.2 contains the results on the mass accretion rates for the different simulations, while Section 3.3 shows the details of the accretion flow around the planet. Finally, we discuss and summarize our results in Sections 4 and 5.

## 5. ACCRETION OF GAS ONTO GIANT PLANETS AND ENVELOPE STRUCTURE IN MAGNETIZED TURBULENT DISKS

---

### 5.2 Computational setup

Simulations were performed using the finite volume fluid dynamics code PLUTO (Mignone et al., 2007). In the code, time stepping is done using a second order Runge Kutta scheme, while the spatial integration is performed using linear interpolation through the second order TVD scheme. The Riemann fluxes are computed using the HLLC and HLLD solvers for the HD and MHD cases, respectively. The code uses the Constrained Transport method for preserving a divergence-free magnetic field (Gardiner and Stone, 2005). The numerical setup for the MHD case follows the setup presented in (Flock et al., 2010).

We use spherical coordinates  $(r, \theta, \phi)$  and the domain is given by  $r \in [1, 10]$ ,  $\theta \in [\pi/2 - 0.3, \pi/2 + 0.3]$  and  $\phi \in [0, 2\pi]$ . The grid resolution is  $(N_r, N_\theta, N_\phi) = (256, 128, 256)$  and it is centered in the center of mass of the planet-star system.

The gas disk is initially in sub-Keplerian rotation around a solar mass star. The azimuthal velocity is given by

$$v_\phi = \sqrt{v_k^2 - c_s^2(a - 2b)}, \quad (5.2)$$

where  $v_k$  is the Keplerian velocity and  $a = 3/2$  and  $b = 0.5$  are the exponents of the radial power law distribution of the density  $\rho \propto r^{-a}$  and sound speed  $c_s = c_0(r \sin \theta)^{-b}$ . The initial density distribution is given by

$$\rho(r, \theta) = (r \sin \theta)^{-3/2} \exp\left(\frac{\sin \theta - 1}{c_0^2}\right). \quad (5.3)$$

The disk is described by a locally isothermal equation of state  $P = c_s^2 \rho$ . The ratio of the pressure scale height  $h$  to the radial coordinate of the disk is taken to be a constant such that  $h = H/(r \sin \theta) = 0.07$ .

The gravitational potential of the planet is given by a softened point-mass potential

$$\Phi_p(\mathbf{r}) = -\frac{GM}{(|\mathbf{r} - \mathbf{r}_p|^2 + \epsilon^2)^{1/2}} \quad (5.4)$$

where  $\epsilon$  is the softening parameter, needed to avoid numerical divergence near the position of the planet. For all the simulations  $\epsilon$  is set to be a fraction of the Hill radius  $\epsilon = kr_p(M_p/3)^{1/3}$  with  $k = 0.3$ . Distances are given in units of  $r_0 = 1AU$ , density is given in units of  $\rho_0 = 1 \times 10^{-12} gcm^{-3}$ , and velocity is given in units of Keplerian speed at  $1AU$ ,  $v_0 = v_k(1AU)$ . The surface density have been scaled such that the total disk mass is  $0.01M_{star}$ . Magnetic fields are given in units of  $B_0 = \sqrt{4\pi\rho_0 v_0^2}$ . The equations of motion of the planet are solved at each timestep with a leap frog integrator.

The components of the torque vector in cartesian coordinates are given by

$$\Gamma_i = GM_p \int \rho(\mathbf{r}) \frac{(\mathbf{r}_p \times \mathbf{r})_i}{(|\mathbf{r} - \mathbf{r}_p|^2 + \epsilon^2)^{3/2}} dV, \quad (5.5)$$

where  $i \in \{x, y, z\}$  is any of the three cartesian indices and  $(\vec{r}_p \times \vec{r})_i = (\vec{r}_p \times \vec{r}) \cdot \hat{e}_i$ , and  $\hat{e}_i$  are the cartesian unit vectors. Specific torques are given in units of  $v_k^2(1AU)$ .

### 5.2.1 Boundary conditions

The boundary conditions for the velocities and magnetic field are periodic in the vertical ( $\theta$  boundary) and azimuthal directions and reflective in the radial direction, except for the transverse magnetic field component, which reverses its sign at the radial boundary. Buffer zones are defined at the radial boundaries to avoid boundary effects, where for  $1 < r < 2$  the magnetic resistivity is given by  $\eta = 2 \times 10^{-4}(2 - r)$  and for  $9 < r < 10$  the resistivity is  $\eta = 1 \times 10^{-4}(r - 9)$ .

### 5.2.2 Initial conditions, gap opening and viscosity

The planet is allowed to accrete gas after only 100 orbital periods at  $5AU$  have elapsed (see Figure 5.1). At this stage, a gap has been cleared, and the density has been reduced by more than 95%. We refer to Chapter 4 for a detailed description of the initial setup and the study of the migration and the interaction between the planet and the magnetic field. For the hydrodynamical simulations, viscosity is added explicitly as a source term in the momentum equation. We use an  $\alpha$ -type kinematic viscosity give by  $\nu = \alpha c_s^2 H$ , where  $\alpha$  takes values of  $2 \times 10^{-3}$ ,  $2 \times 10^{-4}$  and  $2 \times 10^{-5}$ .

### 5.2.3 Accretion prescription

The accretion is modelled by removing a fraction of the mass inside the Hill sphere at each time step. At each timestep the new density  $\rho'$  is given by

$$\rho'(\mathbf{r}) = \left(1 - \frac{\Delta t}{t_a}\right) \rho(\mathbf{r}). \quad (5.6)$$

The accreted mass in timestep  $\Delta t$  is  $\Delta M = (\rho(\mathbf{r})\Delta t t_a^{-1})r^2 \sin(\theta) dr d\theta d\phi$ . The accretion rate for timestep  $\Delta t$  is calculated as the accreted mass divided by the timestep  $\Delta M/\Delta t$ . The factor  $t_a$  represents the accretion timescale in which the Hill sphere is emptied if there was no gas flowing in from the disk. This is chosen to be  $t_a = 1\Omega_{1AU}^{-1}$  inside the inner half of the Hill sphere and  $t_a = 2\Omega_{1AU}^{-1}$  in the outer half of the Hill sphere (where  $\Omega_{1AU}^{-1}$  is the keplerian angular frequency at  $1AU$ ). A density floor is applied to the simulations with magnetic fields, where the density is not allowed to drop below  $10^{-19} \text{grcm}^{-3}$ . Nevertheless, the density in the simulation never reaches this value. The magnetic field is not modified as the density is reduced inside the Hill sphere in order to preserve a divergence-free field. The accretion rate has been shown to be dependent on the accretion radius (the distance from the planet up to which mass is removed) and on

## 5. ACCRETION OF GAS ONTO GIANT PLANETS AND ENVELOPE STRUCTURE IN MAGNETIZED TURBULENT DISKS

---

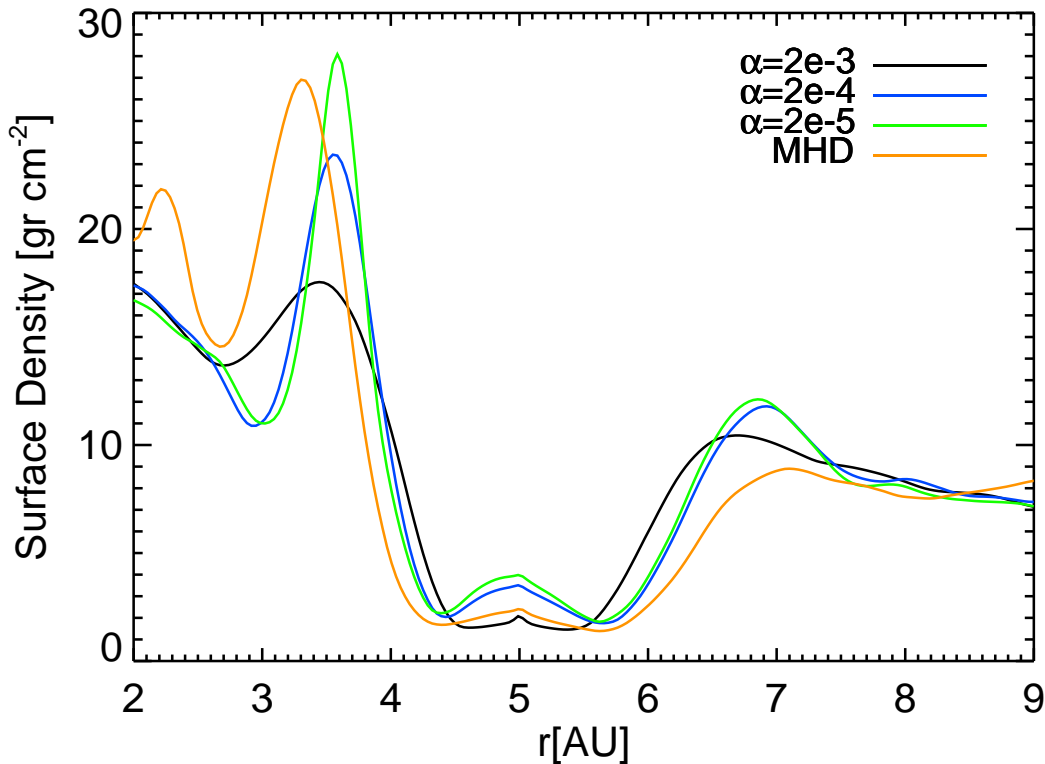


**Figure 5.1:** Initial conditions before the planet starts accreting for the laminar disk simulations and the MHD simulation. The gap in the MHD simulation is found to be wider as compared to all the viscous simulations.

the accretion timescale parameter  $t_a$ . [Tanigawa and Watanabe \(2002\)](#) showed that the accretion radius should be small ( $\approx 0.1r_h$ ) and the accretion timescale should be on the order of the orbital period, in order to obtain converged results. Because of our lower resolution, we take most of the mass from within the inner half of the Hill sphere. This prescription has also been used in previous studies of gas accretion and migration by giant planets ([Kley et al., 2001](#)). We have also check that our results remain valid if one restricts the accretion radius down to  $0.4r_h$ . We have also verified that we obtain the same results if we extend the accretion timescale to  $t_a = 10$ .

## 5.3 Results

### 5.3.1 Structure of the envelope and mass inflow

In this section we study the structure of the density and the inflow of mass in/into the Hill sphere. We calculate the gas density and the mass flux through the surface of the Hill sphere. The mass flux is given by  $\rho v_{inflow} = \rho \mathbf{v} \cdot (\nabla F / |\nabla F|)$ , where  $F(\mathbf{r}) = (\mathbf{r} - \mathbf{r}_p)^2 - r_h^2 = 0$  is the equation describing the surface of the Hill sphere. The density is plotted in Figures 5.2 and 5.3 for all four simulations. The mass flux is plotted in Figures 5.4 and 5.5 for all simulations. These quantities have been averaged in time. We plot the surface of the Hill sphere using an ellipsoidal projection where the three-dimensional structure can be observed. The center of the ellipse corresponds to the point in the Hill sphere that is most distant from the star.

The structure of the spiral arms can be seen in Figures 5.2 and 5.3 in the radial directions (with respect to the star) pointing away from the planet. The arms go into the Hill sphere radially from the inner and outer disk. However, comparing the density plots with the mass flux as is seen in Figures 5.4 and 5.5, the accretion into the Hill sphere is not exactly correlated to the spiral arms in general, meaning that the planet accretes from a more extended region. The density and mass flux are much larger in the case with the higher viscosity ( $\alpha = 2 \times 10^{-3}$ ), and are the lowest in the turbulent magnetized case. In the first high viscosity case, most of the gas accreted is supplied by the disk from the outer disk. In the low viscosity cases and the magnetized case, the mass flux is more extended over the midplane surrounding the planet. In all cases, all the flux through the surface is inflowing, and we see no significant amount gas entering the Hill sphere from the vertical direction above and below the mid-plane. Figure 5.6 shows the vertical structure of the mass flux averaged over the azimuthal direction. Once the gas enters the Hill sphere, we assume it is bounded to the planet and it will be eventually accreted out of the domain.

### 5.3.2 Gas accretion rates

The cumulative mass accreted and the accretion rate are shown in Figures 5.8 and 5.7, for the laminar viscous simulations and the magnetized simulation<sup>1</sup>. We will first discuss the laminar simulations. The largest accretion rate is obtained for the viscous simulation with  $\alpha = 2 \times 10^{-3}$ , as it is expected since the disk accretion rate is proportional to the viscosity. For the case where  $\alpha = 2 \times 10^{-4}$  and  $\alpha = 2 \times 10^{-5}$  the accretion rates are one third lower than the rate for the higher viscosity, but with the  $\alpha = 2 \times 10^{-4}$  being slightly lower than the lowest viscosity case. This means that the limit of the lowest viscosity that the code is able to resolve above numerical dissipation effects is  $\alpha \approx 10^{-4}$ . Additionally,

<sup>1</sup>We will refer to  $\alpha_{MHD}$  to denote the alpha stress that is *measured* in the magnetized simulation, and to  $\alpha$  to denote the [Shakura and Sunyaev \(1973\)](#) viscosity parameter that is *chosen* for the viscous laminar simulations

## 5. ACCRETION OF GAS ONTO GIANT PLANETS AND ENVELOPE STRUCTURE IN MAGNETIZED TURBULENT DISKS

---

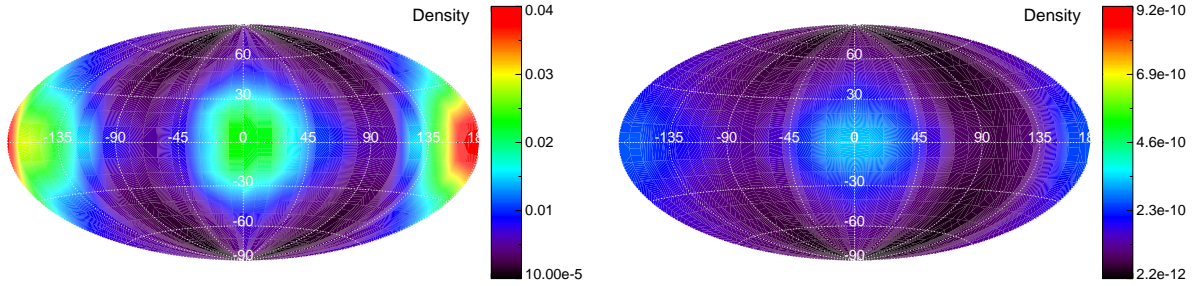


**Figure 5.2:** Density in the surface of the Hill sphere for the viscous laminar runs with  $\alpha = 2 \times 10^{-3}$ (left) and  $\alpha = 2 \times 10^{-4}$ (right). The density is shown in units of  $2 \times 10^{-10} \text{gcm}^{-3}$ . The center of the ellipse corresponds to the point in the Hill sphere that is most distant from the star and points away in the radial direction.

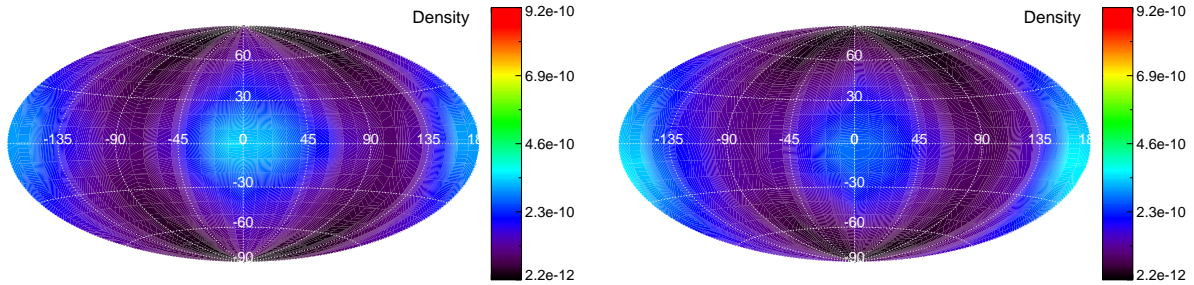


**Figure 5.3:** Density in the surface of the Hill sphere for the viscous laminar run with  $\alpha = 2 \times 10^{-5}$ (left) and for the turbulent run(right). The density is shown in units of  $2 \times 10^{-10} \text{gcm}^{-3}$ . The center of the ellipse corresponds to the point in the Hill sphere that is most distant from the star and points away in the radial direction.

at this low viscosity, our simulation time is not able to cover the viscous evolution, since the viscous timescale is given by  $\tau_{visc} = H^2/\nu = H^2/(\alpha H^2\Omega) = (\alpha\Omega)^{-1}$ .

The magnetic case shows interesting behavior. We find the average accretion rate in the magnetic case to be lower than in all the laminar  $\alpha$  simulations. In this case, the planet accretes gas at a rate which is less than half (40%) the accretion rate in a disk with  $\alpha = 2 \times 10^{-3}$ . This accretion rate is below the rate expected from the numerical dissipation limit. It is also below the value found for the viscous simulation with  $\alpha = 2 \times 10^{-4}$ . For the turbulent magnetized simulation, the global and time-averaged  $\alpha_{MHD}$  is equal to  $\alpha_{MHD} = 1 \times 10^{-3}$ . The global average Maxwell stress is  $\alpha_{MHD,Max} = 2 \times 10^{-4}$ . Due to the presence of the giant planet, the Reynolds stress dominates over the Maxwell stress by a factor of 2 to 3 (see bottom plot of Figure 4.13 of Chapter 4)<sup>1</sup>. However, the effective viscosity provided by the turbulence in the mid-plane is less than in the upper layers of the disk. Small scale turbulent structures in the mid-plane might not be well resolved

---

<sup>1</sup>This results are part of the published work [Uribe et al. \(2011\)](#)

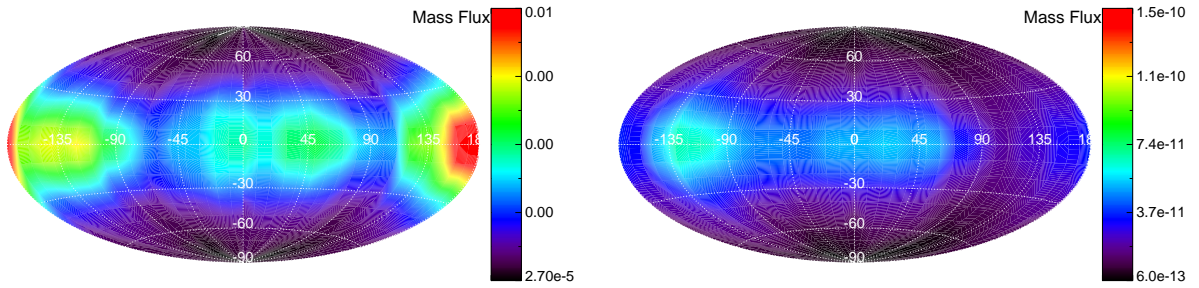


**Figure 5.4:** Mass flux through the surface of the Hill sphere for the viscous laminar runs with  $\alpha = 2 \times 10^{-3}$ (left) and  $\alpha = 2 \times 10^{-4}$ (right). The mass flux is given in units of  $M_{Jyr}^{-1}S^{-1}$ , where quantity  $S$  is the area of the grid cell given by  $S = r_h^2 \Delta\theta_{RH} \Delta\phi_{RH}$ . The center of the ellipse corresponds to the point in the Hill sphere that is most distant from the star and points away in the radial direction.

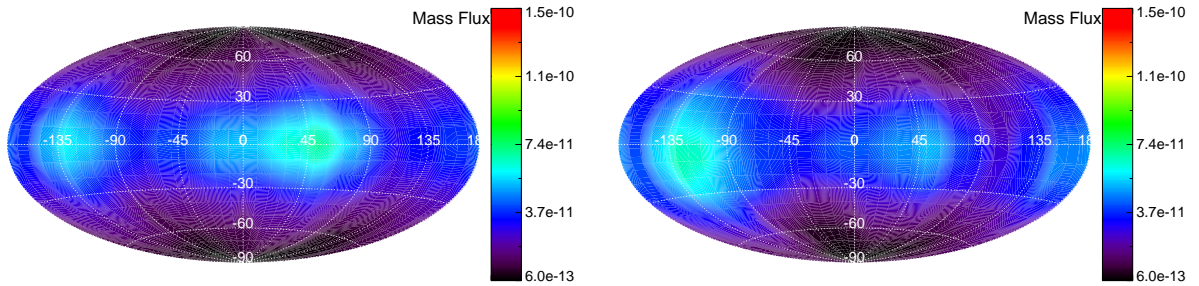


**Figure 5.5:** Mass flux through the surface of the Hill sphere for  $\alpha = 2 \times 10^{-5}$ (left) and for the turbulent run(right). The mass flux is given in units of  $M_{Jyr}^{-1}S^{-1}$ , where quantity  $S$  is the area of the grid cell given by  $S = r_h^2 \Delta\theta_{RH} \Delta\phi_{RH}$ . The center of the ellipse corresponds to the point in the Hill sphere that is most distant from the star and points away in the radial direction.

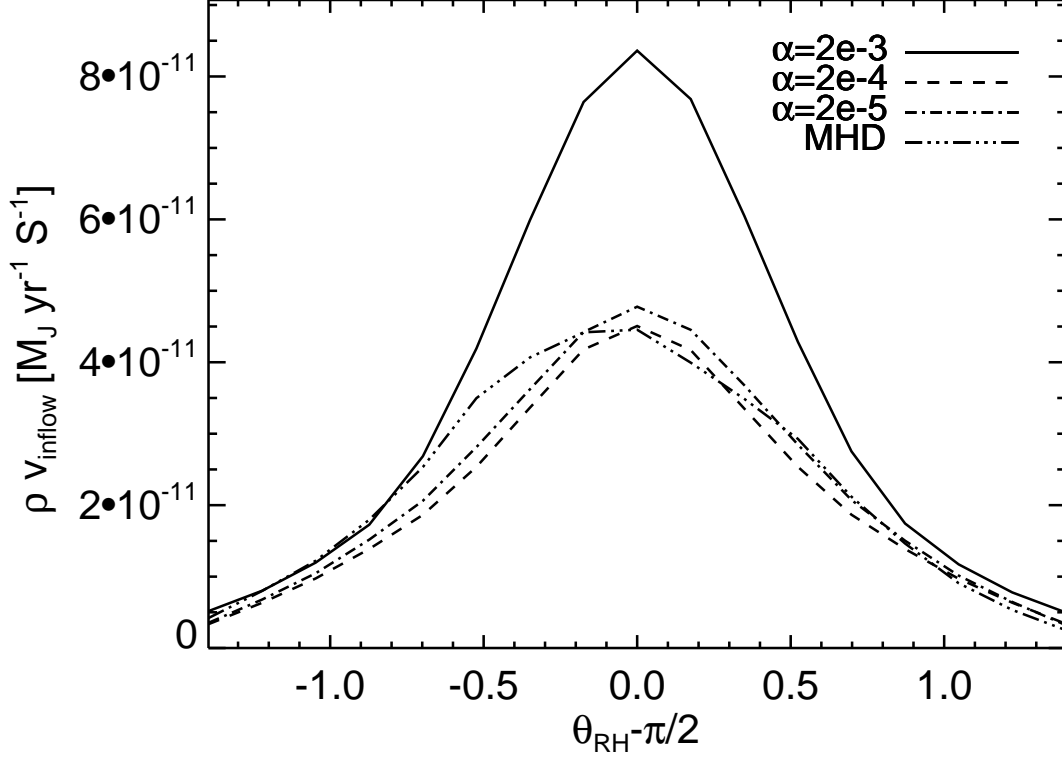
and the  $\alpha$  parameter measured for magnetic turbulence measures large scale transport. Nevertheless, the effective viscosity in the mid-plane should be comparable (or higher) to the one in the viscous laminar simulation with  $\alpha = 2 \times 10^{-5}$ . Since the mean accretion rate in the turbulent run is still lower than in the later case, this suggest an additional effect hindering accretion in the magnetic case.

Figure 5.8 shows the total mass accreted by the planet starting from the time when the accretion is switched on. There is an initial rapid raise due to the material that has accumulated in the Hill sphere during the previous evolution of 100 orbital periods. After this stage, the planet has consumed the "excess" of material, and accretes at a rate in which the disk can provide material. It can be seen in Figure 5.8 that even though the initial conditions are slightly different (some simulations have more gas accumulation around the planet depending on viscosity, as seen in Figure 5.1), after the initial phase is passed, the accretion tends to relax to more or less steady state values.

Previously, [Tanigawa and Watanabe \(2002\)](#) and [Lubow et al. \(1999\)](#) found growth times of

## 5. ACCRETION OF GAS ONTO GIANT PLANETS AND ENVELOPE STRUCTURE IN MAGNETIZED TURBULENT DISKS

---



**Figure 5.6:** Vertical structure of the mass inflow  $\rho v_{inflow}$  into the Hill sphere. The coordinate  $\theta_{RH}$  refers to the polar angle in the frame of the planet. The quantity  $\rho v_{inflow}$  has been azimuthally averaged (with respect to the Hill sphere). The quantity  $S$  is the area of the grid cell given by  $S = r_h^2 \Delta\theta_{RH} \Delta\phi_{RH}$ .

$4 \times 10^4 \text{yr}$  and  $4 \times 10^4 \text{yr}$ . [Kley et al. \(2001\)](#) found gas accretion rates of  $\dot{M} = 6 \times 10^{-5} M_J/\text{yr}$  for Jupiter mass planets, which indicates a growth time of  $2 \times 10^4 \text{yr}$ . We find a mass accretion rate of  $\dot{M} \approx 10^{-6} M_J/\text{yr}$  for the laminar viscous case with  $\alpha = 2 \times 10^{-3}$ . For the magnetized simulation we find  $\dot{M} \approx 6 \times 10^{-7} M_J/\text{yr}$ . These rates are measured only when the planet has already cleared a gap around its orbit, contrary to the previous studies. Therefore we obtain a growth time (after gap opening) one order of magnitude smaller than growth times measured in the absence of a gap.

### 5.3.3 Gas inflow and magnetic pressure

Figure 5.9 shows the radial mass flux and the pressure (and magnetic pressure  $b^2/(8\pi)$ ) at a distance of  $\pm 2r_h$  from the planet position. In the mid-plane, the thermal pressure exceeds the magnetic pressure by a factor of the order of  $10^2$ . There is radial inflow of

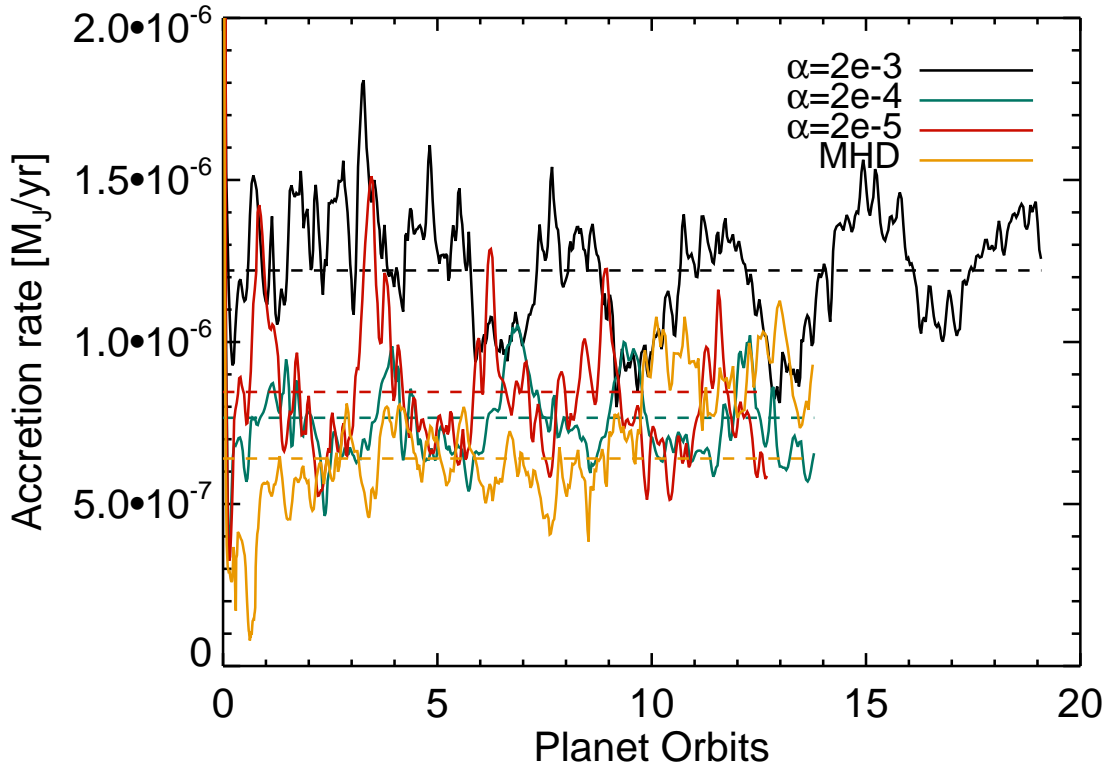


**Figure 5.7:** Mass accretion rate for the three viscous simulations and the magnetized simulation. The red line corresponds to  $\alpha = 2 \times 10^{-5}$ , green line to  $\alpha = 2 \times 10^{-4}$ , and black line to  $\alpha = 2 \times 10^{-3}$ . The yellow line shows the MHD case. The colored dashed lines show the mean value of each simulation.

gas coming from both sides of the planet, and this is dominant in the high viscosity case. As the viscosity gets lower, the density and mass flux decrease. The magnetized case shows radial mass inflow comparable to the two cases with the lower  $\alpha$  viscosity. The radial profile of the thermal pressure is similar for all cases, although the pressure across the Hill sphere decreases with viscosity. At either side of the planet, following the spiral arms, there are bumps of high magnetic pressure.

Figure 5.10 shows the density in the mid plane and the radial velocity for the laminar viscous simulation with  $\alpha = 2 \times 10^{-3}$ . Overplotted is the mid-plane vector field of the velocity. Figure 5.11 shows the same quantities for the magnetized turbulent disk simulation. The mid-plane magnetic pressure for this simulation is plotted in Figure 5.12. In agreement with previous studies (Tanigawa and Watanabe, 2002), we find that the gas accreting into the planet comes from a flow between the open pass-by flow and the gas that is orbiting in horseshoe orbits at corotation. This comes from both sides of the planet,

## 5. ACCRETION OF GAS ONTO GIANT PLANETS AND ENVELOPE STRUCTURE IN MAGNETIZED TURBULENT DISKS

---

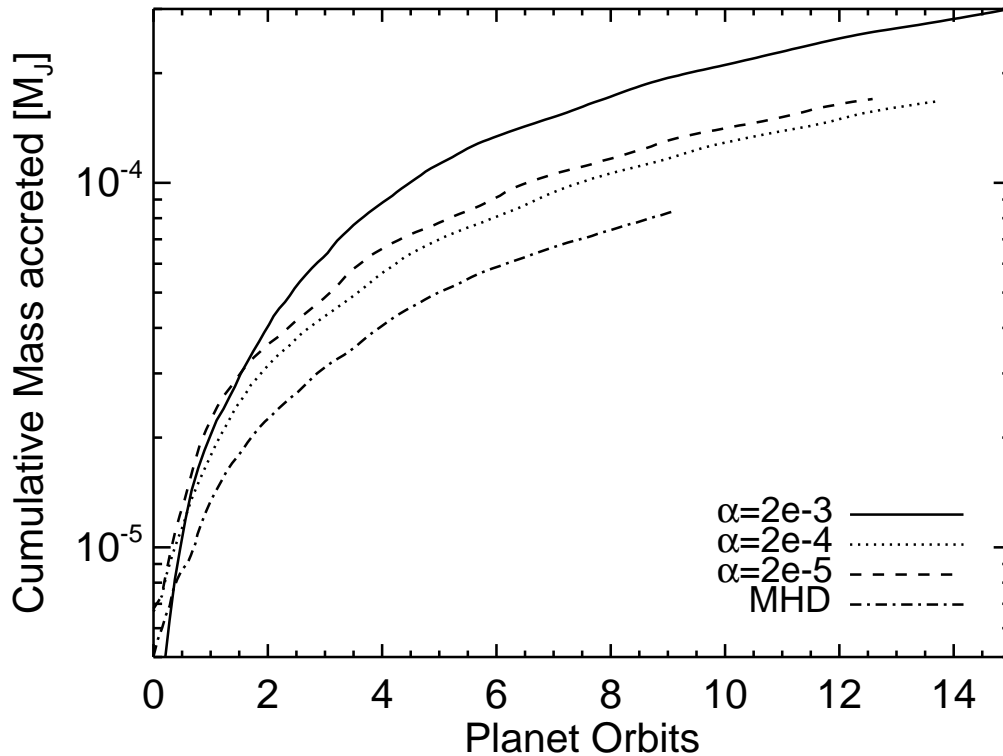


**Figure 5.8:** Cumulative mass accreted by the planet for the three viscous simulations and the magnetized simulation. The solid line corresponds to  $\alpha = 2 \times 10^{-3}$ , dotted line to  $\alpha = 2 \times 10^{-4}$ , and dashed line to  $\alpha = 2 \times 10^{-5}$ . The dash-dotted line shows the MHD case.

as can be seen in the upper right and lower left part of Figures 5.10 and 5.11. Material enters the Hill sphere through these channels, as it is also seen in the mass flux at the surface of the Hill sphere in Figures 5.4 and 5.5. Inside the Hill sphere, the spiral shock and the turbulence allow accretion into the planet through the circumplanetary disk, although in our simulations there is not enough resolution in the Hill sphere to resolve the spiral shock. Outside the Hill sphere, we see the spiral arm structure that forms the bow shock (see D’Angelo et al. (2003b); Tanigawa and Watanabe (2002)), although the shock is diffused by viscosity and turbulence in our simulations.

In the case of the magnetized turbulent run, the velocity structure around the planet is much less uniform (see Figure 5.11) in comparison with the laminar viscous run. This is due to small scale turbulence and the non-uniformity of the magnetic field, seen in Figure 5.12.

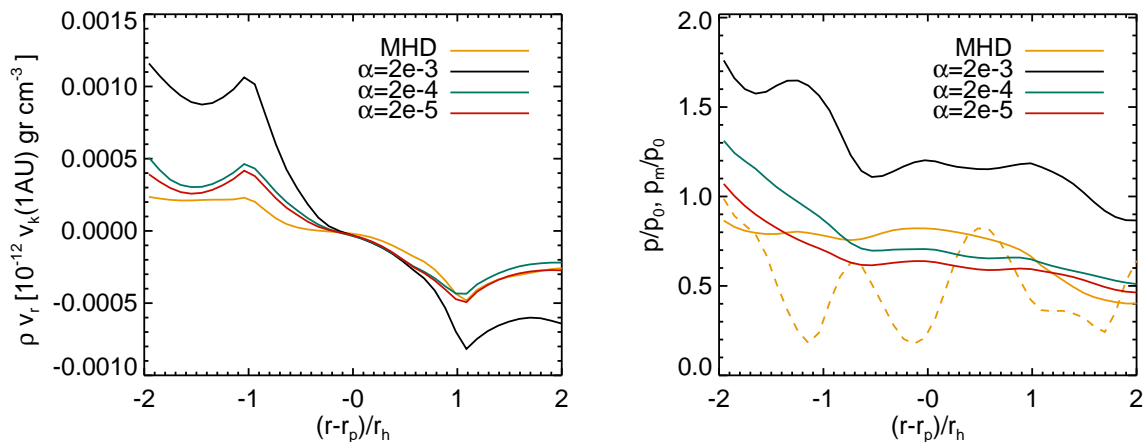


**Figure 5.9:** Left: Radial mass flux for the different runs. Right: Pressure for the different runs. The dashed line shows the magnetic pressure (multiplied by a factor of 150) for the magnetized case.

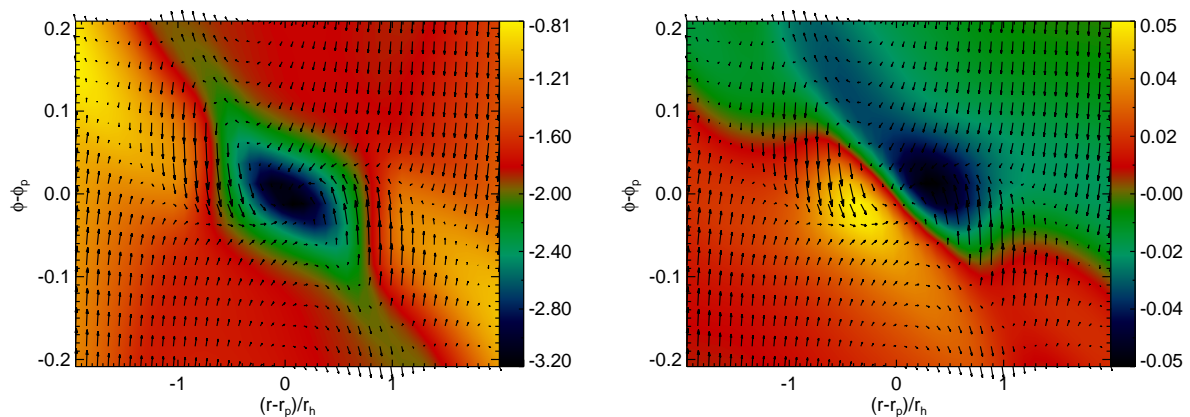


**Figure 5.10:** Left: Density (in units of  $10^{-12} \text{ gr cm}^{-3}$ ) in the mid-plane for the laminar viscous simulation with  $\alpha = 2 \times 10^{-3}$ . Right: Radial velocity (in units of  $v_k(1AU)$ ) in the mid-plane for the same simulation. The overplotted vector field shows the velocity field in the mid-plane.

## 5.4 Discussion and conclusions

Figure 5.13 shows the mass accretion rate as a function of  $\alpha$  for the laminar viscous runs. The rate obtained in the magnetized run is shown in a dotted line, and the square symbol signals the global stress at the beginning of the simulation. We compare this results to the analytical estimate  $\dot{M} = 3\pi\nu\Sigma$ , calculating the surface density inside the gap region and the unperturbed initial density. It is clear that for the lowest value of  $\alpha$ , the numerical dissipation limit at this resolution is reached. The code cannot resolve kinematic viscosities corresponding to less than  $\alpha \approx 10^{-4}$ . For the magnetized case, after 100 orbital periods, the turbulence has decayed as was seen in the simulations presented

## 5. ACCRETION OF GAS ONTO GIANT PLANETS AND ENVELOPE STRUCTURE IN MAGNETIZED TURBULENT DISKS

---

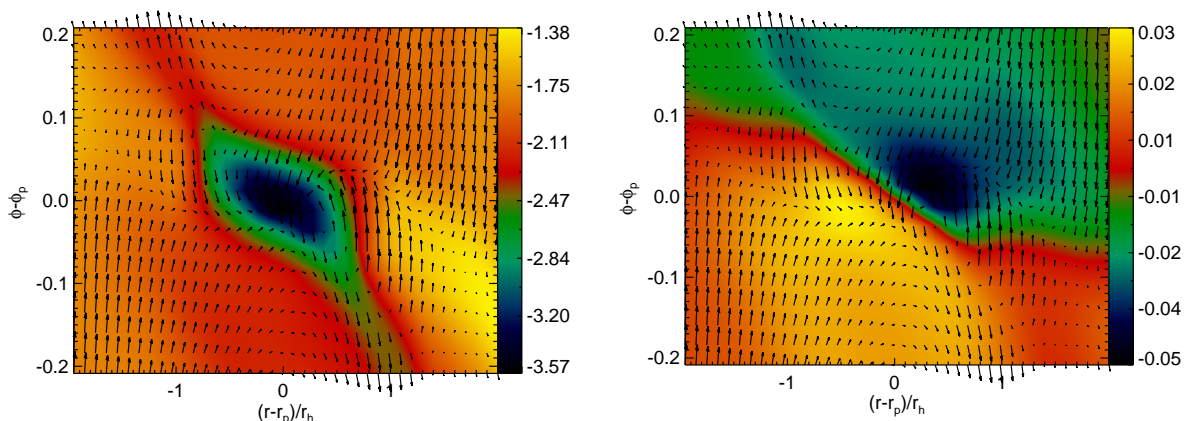


**Figure 5.11:** Left: Density (in units of  $10^{-12} \text{gcm}^{-3}$ ) in the mid-plane for the MHD simulation. Right: Radial velocity (in units of  $v_k(1AU)$ ) in the mid-plane for the MHD simulation. The overplotted vector field shows the velocity field in the mid-plane.

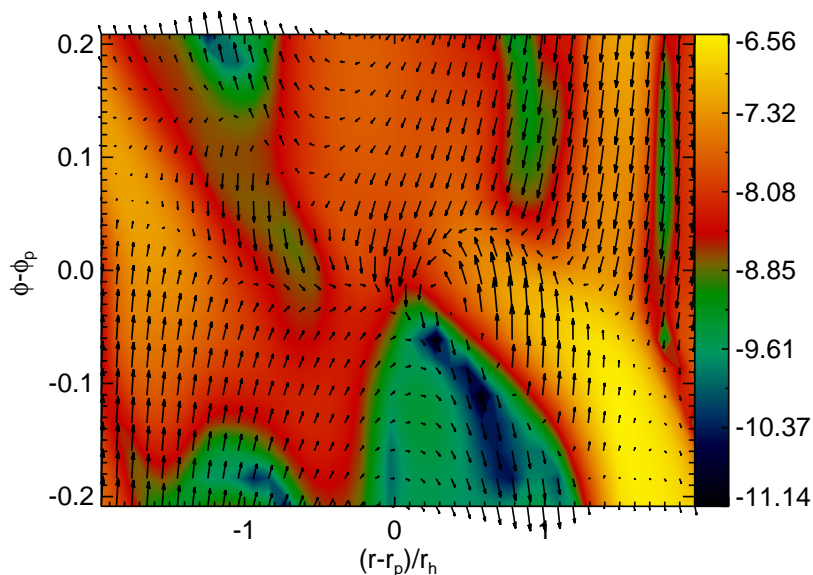


**Figure 5.12:** Magnetic pressure in the mid-plane for the MHD simulation. The overplotted vector field shows the velocity field in the mid-plane.

in Chapter 4. However, the effective global averaged stress coming from the turbulence at the beginning of the simulation (right before accretion starts) is  $\alpha_{MHD} = 1 \times 10^{-3}$ . The Maxwell stress at the beginning of the run is  $\alpha_{MHD,Max} = 2 \times 10^{-4}$ . In the magnetic case, the measured accretion rate is comparable to a laminar viscous run with  $\alpha \approx 10^{-4}$ . It is also significant that the accretion rate measured is below the limit of numerical viscosity, since this points directly to a negative effect on accretion by the magnetic field. This

could be attributed to the fact that turbulent transport is achieved mainly at the large scales, while the effective viscosity provided by the turbulence at the small scales is not represented by the global value of the measured  $\alpha_{MHD}$ . There is also the question of how well resolved is small scale turbulence in our simulations. Additionally, a steady uniform flow into the Hill sphere is seen in the laminar viscous simulation, while in the magnetic case the velocity field is not uniform.

The mass accretion into the Hill sphere happens along two channels located at each side of the planet. Closer to the radial location of the planet, material can't flow in, and instead executes a U-turn, since it loses its angular momentum rapidly as it approaches the planet. Radially away from the planet, the gravitational torque of the planet is not strong enough to pull the material in fast enough, and instead gas orbits passing the planet. The accretion flow lies between these two regions. In all cases, the accretion of gas into the Hill sphere is not spherically symmetric, nor azimuthally symmetric. However, in all cases, the flow through the vertical direction is negligible and the flow is restrained to the disk scale height. In our simulations, the Hill radius is approximately equal to the pressure scale height of the disk. Compared to the analytical estimates of the accretion rate, the value of the rate using the value of the reduced density in the gap region gives a better agreement with our results, although for  $\alpha = 2 \times 10^{-3}$  the simulation accretion rate is around half the analytical value.

Further study needs to be carried out to verify the results presented in this chapter. In order to test the convergence of the obtained accretion rates, it is necessary to perform additional simulations at higher resolutions. Furthermore, one needs to test the effect of the numerical parameters used in the accretion prescription and to achieve longer integration times.

## 5.5 Summary

We find that low levels of MRI-turbulence in protoplanetary disks do not encourage mass accretion, and in fact might slightly hinder accretion as compared to the case of a laminar viscous disk with comparable  $\alpha$  parameter. In all cases, the accretion flow into the Hill sphere of the planet is not spherically or azimuthally symmetric, and is predominantly restricted to the mid-plane of the disk. Even in the turbulent case, we find no vertical flow of mass into the Hill sphere. Accretion rates are most closely approximated analytically by using the reduced density in the gap region. This means that the gap-opening planet never reaches an accretion rate as high as the one given by the unperturbed density of the disk. In a turbulent magnetized disk with global stress parameter of  $\alpha_{MHD} = 1 \times 10^{-3}$ , we find lower accretion rates than those found in a laminar viscous disk with  $\alpha = 10^{-4}$ .

## 5. ACCRETION OF GAS ONTO GIANT PLANETS AND ENVELOPE STRUCTURE IN MAGNETIZED TURBULENT DISKS

---

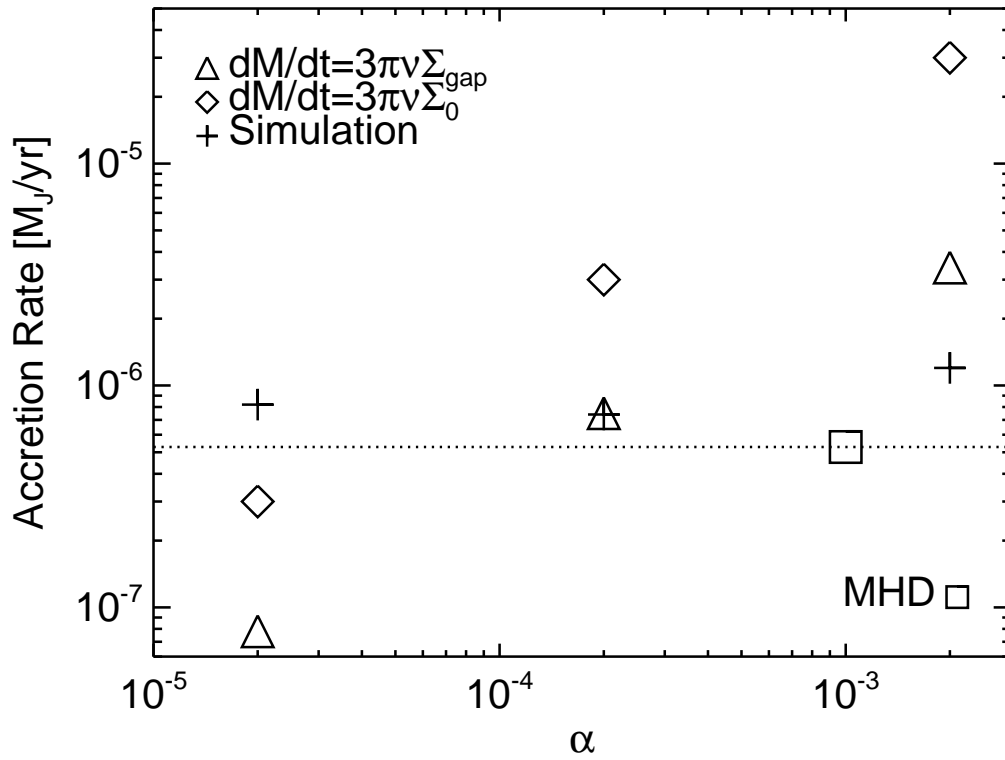


**Figure 5.13:** Mass accretion rates by the planet for different values of  $\alpha$  (crosses) and the turbulent run (square and dotted line). The diamond symbols show the accretion rate  $\dot{M} = 3\pi\nu\Sigma$  calculated using the unperturbed density, while the triangle symbols show the accretion rate calculated using the mean density inside the gap region.

## 6

# Conclusions

This thesis presents a study on different aspects of the interaction between a forming planet and a circumstellar accretion disk of gas and dust. The focus points of this work are the migration behavior of planets due to disk gravitational torques and the accretion of gas onto giant planets. The accretion disk is modelled using hydro and magneto-hydrodynamical simulations with the PLUTO code (Mignone et al., 2007). The planet contribution and modeling was incorporated into the code. The planet module allows for a free moving planet (using a simple leap frog integrator), accretion of gas onto the planet (using the accretion prescription proposed by Kley et al. (2001)) and the presence of multiple planets (which was used in this work as a particle integrator). The main conclusions of this work are the following.

Chapter 3 deals with the migration and gas accretion of Jupiter mass planets in the evolutionary phase when a gap has been opened in the disk. The dependence of the torque was studied as a function of disk surface density, viscosity, steepness of density profile and numerical parameters such as the gravitational softening. The accretion rate onto planets was studied as a function of surface density. We improve over previous results and include migration and accretion, and study the interplay between these two factors. We find that migration is affected by accretion of gas by the planet and very fast inwards migration is suppressed when the planet is accreting material from the disk. Our results can be summarized in more detail as follows.

- The linear estimate of the torque for Type II migration given by Eq. 3.6 is only fully realized when the planet is artificially fixed on a given orbit at constant separation. When the local disk mass is larger than the planet mass, the motion and accretion of the planet affects the migration rate.
- When the local disk mass is larger than the planet mass, the migration rate is highly dependent on the material inside the Hill sphere of the planet. If the Hill sphere is not included in the motion of the planet, the mean cumulative torque is lower than the analytical estimate. For  $M_{disk} \approx \pi r_p^2 \Sigma = 10M_p$ , the mean cumulative torque is

## 6. CONCLUSIONS

---

lower by one order of magnitude. As a result, the migration timescale increases by the same amount.

- When the local disk mass is larger than the planet mass, the mean cumulative torque is lower than the analytical estimate when the planet is accreting gas from the disk (due to the depletion of the Hill sphere). For  $M_{disk} \approx \pi r_p^2 \Sigma = 10M_p$ , the mean cumulative torque is lower by one order of magnitude. As a result, the migration timescale increases by the same amount.
- When the local disk mass is about 10 times the planet mass, the planet undergoes runaway (Type III) migration. Runaway migration is *triggered* by the initial fast migration due to the Hill sphere material, but it is *caused* by gas passing by the planet in open orbits from the inner to the outer disk. Runaway migration is completely suppressed when the Hill sphere is depleted by planetary accretion.
- In a disk with uniform and constant mass accretion, there is no dependence of Type II migration on the power law exponent of the surface density, so that a giant planet will migrate equally fast in a disk with flat or rapidly decreasing density profile

The results of this chapter can be directly implemented in planet population synthesis models, to better model the evolution of massive planets.

Chapter 4 deals with the migration of planets with masses from  $M_p = 3M_{Earth}$  to  $M_p = M_{Jup}$  in magnetized turbulent disks. We improve over previous studies that assume a parametrized form of the turbulent viscosity or that use a forcing potential to simulate turbulence. In our simulations, we study a global disk and turbulence is self-consistently generated by magnetic fields. We find new migration behavior for intermediate-mass planets (Neptunes and Saturns) that might reduce the effectiveness of fast Type I inwards migration. In this case, further study needs to be carried out to directly apply our results in population synthesis simulations. Our results are summarized in more detail as follows.

- For low-mass planets that don't significantly perturb the disk, the stochastic torque resulting from the density perturbations is characterized in terms of the density spectra, the autocorrelation time of the torque and the torque standard deviation. These quantities allow for modeling of the turbulent torque through a forcing potential or as a diffusion process, that are tuned to match the characteristics of MRI turbulence. The parameters found can be directly used in planet population synthesis modeling.
- Due to positive corotation torques, the migration of intermediate-mass planets (in the Neptune/Saturn mass range) can be slowed down or even reverse in parts of the disk where the density increases locally. These type of structures in the disk can be a result of un-uniformities in the internal stresses (i.e the magnetic field). Zonal flows are excited by the magnetic turbulence and have amplitudes of  $\approx 20 - 25\%$

the unperturbed density value. Planets with mass ratios of around  $q = 10^{-4}$  can be temporarily trapped in these locations in the disk.

- Jupiter mass planets strongly decrease the magnetic stress in the disk, and the Reynolds stress dominates the angular momentum transport. This can potentially have an impact on the overall mass accretion rate in the disk. The shape of the gap is also influenced by turbulence, being wider in a magnetized turbulent disk as compared to a viscous laminar disk.

Chapter 5 deals with the accretion rate of gas onto Jupiter-mass planets in a turbulent magnetized disk. This is the first study to investigate how accretion is affected by turbulence and turbulent magnetic fields. Our results suggest that accretion in turbulent magnetized disks cannot be directly modelled by assuming a laminar disk with a parametrized form of the viscosity. We find that accretion rates are smaller than previously calculated. Further work is required to understand the interplay between turbulence, magnetic fields and accretion. Our results are summarized as follows.

- Accretion rates are lower in the presence of magnetic turbulence as compared to the accretion rate in a viscous laminar disk that has an  $\alpha = \nu/H\Omega$  equal to the global average stress measured in the turbulent disk.
- The accretion flow structure is very similar to the one obtained in two-dimensional simulations of laminar viscous disks. The accretion flow is constrained to specific regions in the mid-plane of the disk and it is not azimuthally or spherically symmetric. The mean vertical structure of the accretion flow is gaussian, following the density distribution, and its vertical dimension is constrained to one scale height of the disk. The flow in the vertical direction is negligible as compared to the mid-plane flow, in both the turbulent and the laminar cases.
- In general, the accretion rate of gas onto the planet is best approximated by  $\dot{M} = 3\pi\nu\Sigma_{gap}$ . However we do not find an exact match for the high  $\alpha = 10^{-2}$  case. This could possibly be a result of the numerical parameters that we used for the accretion prescription.

## 6.1 Future research

Many aspects that were not explored in this work pose interesting questions for future investigations. One aspect that has not been explored in the literature is the migration of planets in turbulent disks with thermal effects included. In all the simulations presented in this work, the disk is locally isothermal, such that its temperature profile is constant. This assumes an infinitely short cooling time. It is well known that including heating and cooling effects or a full treatment of radiation transport affects the migration rates observed in simulations (Klahr and Kley, 2006; Kley et al., 2009; Paardekooper et al.,

## 6. CONCLUSIONS

---

2010). This is due to contributions to the torque from the corotation region, that behave in a similar manner as the viscosity-induced corotation torques in isothermal disks. Studying thermal effects in magnetized turbulent disks will provide a more complete and comprehensive understanding of the impact of corotation torques and of the migration rates of embedded planets. An interesting option to tackle this problem is to include thermal effects in two-dimensional simulations with forced turbulence. This greatly simplifies the numerical problem and makes the simulations practical. The forced turbulence can be tuned to resemble MRI turbulence using the parameters found in this work. This would allow a practical study of different parameters without the prohibiting limitations of three-dimensional MHD simulations.

Another aspect that deserves attention is the numerical modeling of the gas accretion by planets in hydrodynamical simulations. Improving the prescription for modeling the gas accretion is necessary to understand the full formation process. A better model for accretion must include physical elements that tie the disk modeling to the formation of the planet and its envelope. One such element is the radiation feedback unto the disk from the forming protoplanet, such that the contraction of the envelope can be followed. Furthermore, it is necessary to implement a sub-grid model for the inner envelope of the planet that provides a boundary condition for the disk simulations. The treatment of the magnetic field when the planet is accreting also needs to be revised. In this work, mass is removed from the grid to simulate accretion and the magnetic field is not modified. As before, ultimately there needs to be a treatment of the magnetic field based on physical arguments. The implementation of these elements will be possible as higher resolution simulations become practical, and allow for the circumplanetary disk to be properly resolved.

Higher resolution simulations are also required to establish the convergence of the results with increasing resolution. Longer integration times are necessary to cover the longer physical timescales associated with the viscous evolution of the disk, gap opening and the evolution of zonal flow structures. Covering these timescales is not yet practically possible for three-dimensional magneto-hydrodynamics simulations.

An important application of this work is related to observations of the dust in the outer parts of protoplanetary disks at sub-milimeter and millimeter wavelengths. Telescopes like ALMA will be able to probe and spatially resolve the outer regions of protoplanetary disks at these wavelengths. A very interesting question is whether the structures in the disk resulting from planet-disk interactions or from magnetic turbulence can be observed and under what conditions. The results of this work can be incorporated into dust growth and evolution models or radiative transfer codes in order to model observed disk structures like gaps or density inhomogeneities.

## Appendix A

# Stochastic gravitational torque on low-mass planets

In this Appendix we present results about the characterization of the turbulent torque exerted on low mass planets in turbulent disks. This subject has been covered extensively using two-dimensional hydrodynamical simulations of planet-disk interaction (Baruteau and Lin, 2010; Laughlin et al., 2004; Ogihara et al., 2007), and using a semi-analytical model to describe the migration (Adams and Bloch, 2009). In hydrodynamical simulations, turbulence in the disk is not consistently generated by disk instabilities. Instead it is modelled as a turbulent perturbation in the form of a potential that appears a source term in the momentum equation. The potential is taken to be a sum over a certain number of modes, each with a different amplitude and lifetime. Laughlin et al. (2004) proposed the following form of the potential (for mode  $m$ )

$$\Phi_m = \eta_m r^{-0.5} e^{(r-r_c)^2/\sigma^2} \cos(m\theta - \phi - \Omega_c \tilde{t}) \sin\left(\pi \frac{\tilde{t}}{\Delta t}\right). \quad (\text{A.1})$$

Here,  $\eta_m$  is the amplitude of mode  $m$ ,  $(r_c, \phi_c)$  are parameters sampled from a uniform distribution covering the computational domain, the mode  $m$  is sampled from a log-random distribution, and the time  $\tilde{t} = t - t_{m,c}$ , where  $t_{m,c}$  is the starting time of mode  $m$ . At any given time, a given number of modes are alive in the disk. The amplitude and lifetime of the mode are tuned in order to obtain a density amplitudes spectrum that resembles a turbulent disk spectrum with well characterized magnetic turbulence.

In order to have estimations the amplitude and lifetime of modes in the turbulent potential, one needs to characterize the stochastic *gravitational* torque exerted by the disk on test massless particles. We performed simulations of massless particles embedded in a turbulent disk. The computational setup is identical to the one described in Chapter 4, except that instead of a planet orbiting the disk, we follow the orbital evolution of 50 massless particles at different positions in the disk. These particles have no feedback on

## A. STOCHASTIC GRAVITATIONAL TORQUE ON LOW-MASS PLANETS

---

the disk. In Chapter 3, we already present the resulting density spectrum and discuss its implications. Here, we focus on the calculation of the lifetime of the modes and of the turbulent torque variance. The particles sample the perturbations throughout the disk. We average quantities over the number of particles.

Figure A.1 shows the evolution of the semi-major axis for the 50 particles. The color signals the position of the particles for the following figures. On the right plot, we show the normalized variation in semi-major axis for all particles. The variation in semi-major axis is very small, and particles approximately follow their initial orbits. The density in this case is very low so that the fractional changes are small. The right plot shows the fractional variation in the small scales. Here it is possible to see why a statistical approach is necessary. Some particles drift in, some out. The purely turbulent perturbations act as a diffusion process. The cumulative torques exerted on the particles are shown in Figure A.2. The right plot shows the distribution of the mean torque at the end of the simulated time. We can see that the torque distribution is approximately gaussian. The standard deviation of the fitted gaussian profile provides an estimate of the range of torques (and migration directions) experienced by particles. For this case we obtain

$$\sigma_{tor} \approx 1.5 \times 10^{-5} v_k^2 (1AU). \quad (\text{A.2})$$

The lifetime of the modes is estimated as the autocorrelation time of the torque  $\Gamma(t)$  (Baruteau and Lin, 2010). This is calculated using the autocorrelation function given by

$$ACF(\tau) = \frac{\int_{\tau}^{t_{max}} \Gamma(t)\Gamma(t-\tau)dt}{\int_{\tau}^{t_{max}} \Gamma(t)^2 dt}. \quad (\text{A.3})$$

The autocorrelation timescale is given by

$$\tau_c = \int_0^{t_{max}} ACF(\tau) d\tau. \quad (\text{A.4})$$

For our simulation, we obtain  $\tau_c \approx 2$  local orbits. The first and second zero crossings of the torque autocorrelation function occur at 0.2 and 0.8 local orbits. The lifetime of the modes in the turbulent potential should be taken to be one of these values.

In the semi-analytical approach of modeling turbulent migration using a diffusion equation for the particle distribution, the diffusion coefficient is given by (Adams and Bloch, 2009)

$$D = \frac{(\Delta L)^2}{\tau_c}, \quad (\text{A.5})$$

where  $(\Delta L)$  is the fluctuation amplitude of the angular momentum of the particles (that can be obtained from the standard deviation of the torque calculations), and  $\tau_c$  is again the timescale over which the perturbations are independent from each other, given by the autocorrelation time calculated above.

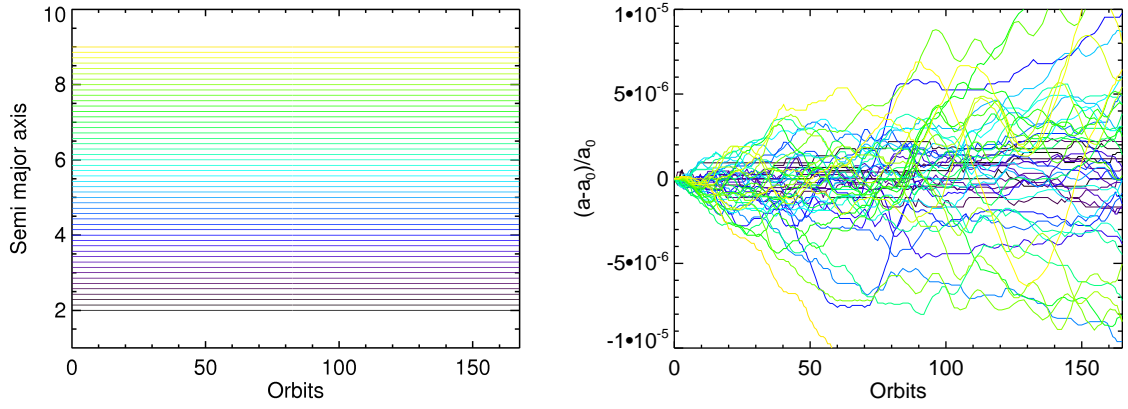


**Figure A.1:** Left: Semi-major axis vs time for 50 massless particles (position signaled by color). Right: Fractional change in semi-major axis vs time. Particles undergo a diffusion process in small scales.

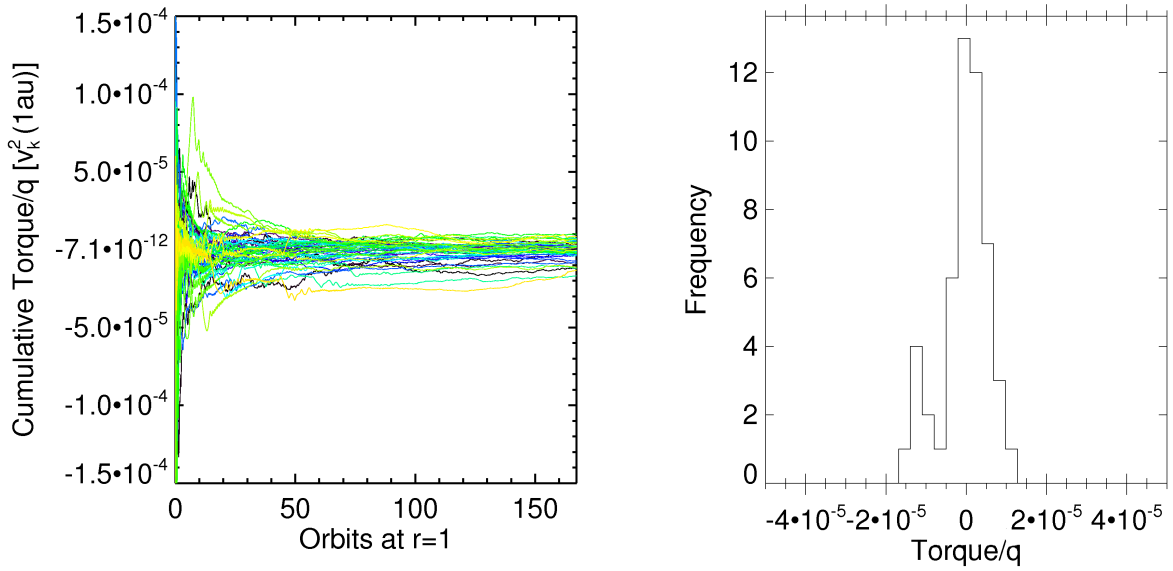


**Figure A.2:** Left: Cumulative torque on the 50 massless particles. Right: Histogram of the cumulative torque at the end of the simulation (after 150 orbits).

## A. STOCHASTIC GRAVITATIONAL TORQUE ON LOW-MASS PLANETS

---

# Bibliography

- Adams, F. C. and Bloch, A. M.: 2009, ApJ **701**, 1381 [10](#), [40](#), [83](#), [84](#)
- Alexander, R.: 2008, *New Astronomy Reviews* **52**, 60 [4](#)
- Alibert, Y., Mordasini, C., and Benz, W.: 2004, A&A **417**, L25 [8](#), [18](#), [64](#)
- Alibert, Y., Mordasini, C., Benz, W., and Winisdoerffer, C.: 2005, A&A **434**, 343 [5](#), [18](#), [38](#), [64](#)
- Angel, J. R. P.: 1994, Nature **368**, 203 [8](#)
- Armitage, P. J.: 2007a, *ArXiv Astrophysics e-prints* [19](#)
- Armitage, P. J.: 2007b, ApJ **665**, 1381 [19](#)
- Baines, M. J. and Williams, I. P.: 1965, Nature **205**, 59 [4](#)
- Balbus, S. A. and Hawley, J. F.: 1991, ApJ **376**, 214 [5](#), [39](#), [65](#)
- Balbus, S. A. and Hawley, J. F.: 1998, *Reviews of Modern Physics* **70**, 1 [6](#), [39](#)
- Ballester, G. E., Sing, D. K., and Herbert, F.: 2007, Nature **445**, 511 [7](#)
- Baruteau, C. and Lin, D. N. C.: 2010, ApJ **709**, 759 [ix](#), [10](#), [39](#), [46](#), [49](#), [83](#), [84](#)
- Baruteau, C. and Masset, F.: 2008, ApJ **672**, 1054 [14](#)
- Batalha, N. M., Borucki, W. J., Bryson, S. T., Buchhave, L. A., Caldwell, D. A., Christensen-Dalsgaard, J., Ciardi, D., Dunham, E. W., Fressin, F., Gautier, III, T. N., Gilliland, R. L., Haas, M. R., Howell, S. B., Jenkins, J. M., Kjeldsen, H., Koch, D. G., Latham, D. W., Lissauer, J. J., Marcy, G. W., Rowe, J. F., Sasselov, D. D., Seager, S., Steffen, J. H., Torres, G., Basri, G. S., Brown, T. M., Charbonneau, D., Christiansen, J., Clarke, B., Cochran, W. D., Dupree, A., Fabrycky, D. C., Fischer, D., Ford, E. B., Fortney, J., Girouard, F. R., Holman, M. J., Johnson, J., Isaacson, H., Klaus, T. C., Machalek, P., Moorehead, A. V., Morehead, R. C., Ragozzine, D., Tenenbaum, P.,

## BIBLIOGRAPHY

---

- Twicken, J., Quinn, S., VanCleve, J., Walkowicz, L. M., Welsh, W. F., Devore, E., and Gould, A.: 2011, *ApJ* **729**, 27 [7](#)
- Bate, M. R., Lubow, S. H., Ogilvie, G. I., and Miller, K. A.: 2003, *MNRAS* **341**, 213 [vii](#), [6](#), [9](#), [19](#), [38](#), [39](#), [65](#)
- Batygin, K. and Stevenson, D. J.: 2010, *ApJ* **714**, L238 [8](#)
- Beaulieu, J.-P., Bennett, D. P., Fouqué, P., Williams, A., Dominik, M., Jørgensen, U. G., Kubas, D., Cassan, A., Coutures, C., Greenhill, J., Hill, K., Menzies, J., Sackett, P. D., Albrow, M., Brilliant, S., Caldwell, J. A. R., Calitz, J. J., Cook, K. H., Corrales, E., Desort, M., Dieters, S., Dominis, D., Donatowicz, J., Hoffman, M., Kane, S., Marquette, J.-B., Martin, R., Meintjes, P., Pollard, K., Sahu, K., Vinter, C., Wambsganss, J., Woller, K., Horne, K., Steele, I., Bramich, D. M., Burgdorf, M., Snodgrass, C., Bode, M., Udalski, A., Szymański, M. K., Kubiak, M., Więckowski, T., Pietrzyński, G., Soszyński, I., Szewczyk, O., Wyrzykowski, L., Paczyński, B., Abe, F., Bond, I. A., Britton, T. R., Gilmore, A. C., Hearnshaw, J. B., Itow, Y., Kamiya, K., Kilmartin, P. M., Korpela, A. V., Masuda, K., Matsubara, Y., Motomura, M., Muraki, Y., Nakamura, S., Okada, C., Ohnishi, K., Rattenbury, N. J., Sako, T., Sato, S., Sasaki, M., Sekiguchi, T., Sullivan, D. J., Tristram, P. J., Yock, P. C. M., and Yoshioka, T.: 2006, *Nature* **439**, 437 [8](#)
- Bennett, D. P. and Rhie, S. H.: 1996, *ApJ* **472**, 660 [8](#)
- Benz, W., Mordasini, C., Alibert, Y., and Naef, D.: 2008, *Physica Scripta Volume T* **130(1)**, 014022 [8](#), [9](#), [18](#), [38](#), [64](#)
- Berlage, H. P.: 1968, *The origin of the solar system* [2](#)
- Birnstiel, T., Dullemond, C. P., and Brauer, F.: 2010, *A&A* **513**, A79+ [4](#)
- Birnstiel, T., Ormel, C. W., and Dullemond, C. P.: 2011, *A&A* **525**, A11+ [4](#)
- Bodenheimer, P., Hubickyj, O., and Lissauer, J. J.: 2000, *Icarus* **143**, 2 [7](#)
- Borucki, W. J. and Summers, A. L.: 1984, *Icarus* **58**, 121 [7](#)
- Boss, A. P.: 1997, *Science* **276**, 1836 [5](#), [64](#)
- Bouwman, J., Henning, T., Hillenbrand, L. A., Meyer, M. R., Pascucci, I., Carpenter, J., Hines, D., Kim, J. S., Silverstone, M. D., Hollenbach, D., and Wolf, S.: 2008, *ApJ* **683**, 479 [4](#)
- Brauer, F., Dullemond, C. P., and Henning, T.: 2008, *A&A* **480**, 859 [4](#), [5](#)

## BIBLIOGRAPHY

---

- Bryden, G., Chen, X., Lin, D. N. C., Nelson, R. P., and Papaloizou, J. C. B.: 1999, *ApJ* **514**, 344 [14](#), [19](#), [39](#), [65](#)
- Cameron, A. G. W.: 1962, *Icarus* **1**, 13 [3](#)
- Chamberlin, T. C.: 1901, *ApJ* **14**, 17 [2](#)
- Charbonneau, D., Allen, L. E., Megeath, S. T., Torres, G., Alonso, R., Brown, T. M., Gilliland, R. L., Latham, D. W., Mandushev, G., O'Donovan, F. T., and Sozzetti, A.: 2005, *ApJ* **626**, 523 [7](#)
- Crida, A. and Morbidelli, A.: 2007, *MNRAS* **377**, 1324 [18](#), [19](#), [20](#), [34](#)
- Crida, A., Morbidelli, A., and Masset, F.: 2006, *Icarus* **181**, 587 [14](#), [18](#), [39](#)
- Cumming, A., Marcy, G. W., and Butler, R. P.: 1999, *ApJ* **526**, 890 [7](#)
- Currie, T.: 2009, *ApJ* **694**, L171 [18](#)
- D'Angelo, G., Bate, M. R., and Lubow, S. H.: 2005, *MNRAS* **358**, 316 [19](#)
- D'Angelo, G., Kley, W., and Henning, T.: 2003a, in D. Deming & S. Seager (ed.), *Scientific Frontiers in Research on Extrasolar Planets*, Vol. 294 of *Astronomical Society of the Pacific Conference Series*, pp 323–326 [65](#)
- D'Angelo, G., Kley, W., and Henning, T.: 2003b, *ApJ* **586**, 540 [38](#), [65](#), [74](#)
- Davis, S. W., Stone, J. M., and Pessah, M. E.: 2010, *ApJ* **713**, 52 [6](#)
- de Val-Borro, M., Edgar, R. G., Artymowicz, P., Cieliegl, P., Cresswell, P., D'Angelo, G., Delgado-Donate, E. J., Dirksen, G., Fromang, S., Gawryszczak, A., Klahr, H., Kley, W., Lyra, W., Masset, F., Mellema, G., Nelson, R. P., Paardekooper, S., Peplinski, A., Pierens, A., Plewa, T., Rice, K., Schäfer, C., and Speith, R.: 2006, *MNRAS* **370**, 529 [18](#), [39](#)
- Dominik, C. and Tielens, A. G. G. M.: 1997, *ApJ* **480**, 647 [4](#)
- Donn, B. and Sears, G. W.: 1963, *Science* **140**, 1208 [4](#)
- Dullemond, C. P. and Dominik, C.: 2005, *A&A* **434**, 971 [4](#)
- Dullemond, C. P. and Monnier, J. D.: 2010, *ARA&A* **48**, 205 [4](#)
- Durisen, R. H., Boss, A. P., Mayer, L., Nelson, A. F., Quinn, T., and Rice, W. K. M.: 2007, *Protostars and Planets V* pp 607–622 [5](#), [64](#)

## BIBLIOGRAPHY

---

- Dzyurkevich, N., Flock, M., Turner, N. J., Klahr, H., and Henning, T.: 2010, *A&A* **515**, A70+ 6, 44, 59
- Edgar, R. G.: 2007, *ApJ* **663**, 1325 10, 19
- Edgeworth, K. E.: 1949, *MNRAS* **109**, 600 4
- Edgeworth, K. E.: 1962, *The Observatory* **82**, 219 4
- Fabrycky, D. C. and Winn, J. N.: 2009, *ApJ* **696**, 1230 7
- Fleming, T. and Stone, J. M.: 2003, *ApJ* **585**, 908 6
- Flock, M., Dzyurkevich, N., Klahr, H., and Mignone, A.: 2010, *A&A* **516**, A26+ 40, 66
- Flock, M., Dzyurkevich, N., Klahr, H., Turner, N. J., and Henning, T.: 2011, *ApJ* **735**, 122 6, 43
- Ford, E. B. and Rasio, F. A.: 2008, *ApJ* **686**, 621 7
- Fromang, S. and Nelson, R. P.: 2009, *A&A* **496**, 597 46
- Fromang, S. and Papaloizou, J.: 2007, *A&A* **476**, 1113 6
- Fromang, S., Papaloizou, J., Lesur, G., and Heinemann, T.: 2007, *A&A* **476**, 1123 6
- Fromang, S., Terquem, C., and Nelson, R. P.: 2005, *MNRAS* **363**, 943 38, 50
- Gardiner, T. A. and Stone, J. M.: 2005, *Journal of Computational Physics* **205**, 509 40, 66
- Gaudi, B. S. and Winn, J. N.: 2007, *ApJ* **655**, 550 7
- Geisel, S. L.: 1970, *ApJ* **161**, L105+ 4
- Gilliland, R. L., Jenkins, J. M., Borucki, W. J., Bryson, S. T., Caldwell, D. A., Clarke, B. D., Dotson, J. L., Haas, M. R., Hall, J., Klaus, T., Koch, D., McCauliff, S., Quintana, E. V., Twicken, J. D., and van Cleve, J. E.: 2010, *ApJ* **713**, L160 7
- Goldreich, P. and Lynden-Bell, D.: 1965, *MNRAS* **130**, 97 5
- Goldreich, P. and Tremaine, S.: 1979, *ApJ* **233**, 857 6
- Goldreich, P. and Tremaine, S.: 1980, *ApJ* **241**, 425 38
- Gould, A. and Loeb, A.: 1992, *ApJ* **396**, 104 8
- Guan, X., Gammie, C. F., Simon, J. B., and Johnson, B. M.: 2009, *ApJ* **694**, 1010 6

## BIBLIOGRAPHY

---

- Güttler, C., Blum, J., Zsom, A., Ormel, C. W., and Dullemond, C. P.: 2010, *A&A* **513**, A56+ [4](#)
- Haisch, Jr., K. E., Lada, E. A., and Lada, C. J.: 2001, *ApJ* **553**, L153 [vii](#), [9](#)
- Hawley, J. F., Gammie, C. F., and Balbus, S. A.: 1995, *ApJ* **440**, 742 [6](#)
- Hawley, J. F., Gammie, C. F., and Balbus, S. A.: 1996, *ApJ* **464**, 690 [6](#)
- Henning, T. and Meeus, G.: 2009, *ArXiv e-prints* [4](#)
- Henning, T. and Stognienko, R.: 1996, *A&A* **311**, 291 [4](#)
- Howard, A. W., Marcy, G. W., Johnson, J. A., Fischer, D. A., Wright, J. T., Isaacson, H., Valenti, J. A., Anderson, J., Lin, D. N. C., and Ida, S.: 2010, *Science* **330**, 653 [7](#), [8](#)
- Hoyle, F.: 1960, *QJRAS* **1**, 28 [3](#)
- Hubickyj, O., Bodenheimer, P., and Lissauer, J. J.: 2005, *Icarus* **179**, 415 [64](#)
- Hughes, A. L. H. and Armitage, P. J.: 2010, *ApJ* **719**, 1633 [4](#)
- Ibgui, L. and Burrows, A.: 2009, *ApJ* **700**, 1921 [8](#)
- Ida, S. and Lin, D. N. C.: 2004, *ApJ* **604**, 388 [8](#), [38](#)
- Ida, S. and Lin, D. N. C.: 2007, *ArXiv e-prints* [38](#)
- Ida, S. and Lin, D. N. C.: 2008, in Y.-S. Sun, S. Ferraz-Mello, & J.-L. Zhou (ed.), *IAU Symposium*, Vol. 249 of *IAU Symposium*, pp 223–232 [9](#), [18](#), [38](#), [64](#)
- Ikoma, M., Nakazawa, K., and Emori, H.: 2000, *ApJ* **537**, 1013 [64](#)
- Jeans, J.: 1931, *Nature* **128**, 432 [2](#)
- Jeffreys, H. and Moulton, F. R.: 1929, *Science* **69**, 245 [2](#)
- Ji, H., Burin, M., Schartman, E., and Goodman, J.: 2006, *Nature* **444**, 343 [5](#)
- Johansen, A. and Klahr, H.: 2005, *ApJ* **634**, 1353 [6](#)
- Johansen, A., Klahr, H., and Henning, T.: 2006, *ApJ* **636**, 1121 [6](#)
- Johansen, A., Oishi, J. S., Mac Low, M.-M., Klahr, H., Henning, T., and Youdin, A.: 2007, *Nature* **448**, 1022 [6](#)
- Johansen, A., Youdin, A., and Klahr, H.: 2009, *ApJ* **697**, 1269 [6](#), [43](#)

## BIBLIOGRAPHY

---

- Johnson, E. T., Goodman, J., and Menou, K.: 2006, *ApJ* **647**, 1413 [40](#)
- Johnson, J. A., Aller, K. M., Howard, A. W., and Crepp, J. R.: 2010, *PASP* **122**, 905 [7](#)
- Juhász, A., Bouwman, J., Henning, T., Acke, B., van den Ancker, M. E., Meeus, G., Dominik, C., Min, M., Tielens, A. G. G. M., and Waters, L. B. F. M.: 2010, *ApJ* **721**, 431 [4](#)
- Juhász, A., Henning, T., Bouwman, J., Dullemond, C. P., Pascucci, I., and Apai, D.: 2009, *ApJ* **695**, 1024 [4](#)
- Jurić, M. and Tremaine, S.: 2008, *ApJ* **686**, 603 [7](#)
- Kalas, P., Graham, J. R., and Clampin, M.: 2005, *Nature* **435**, 1067 [8](#)
- Klahr, H. and Kley, W.: 2006, *A&A* **445**, 747 [65](#), [81](#)
- Klahr, H. H. and Bodenheimer, P.: 2003, *ApJ* **582**, 869 [5](#)
- Kley, W., Bitsch, B., and Klahr, H.: 2009, *A&A* **506**, 971 [14](#), [81](#)
- Kley, W., D’Angelo, G., and Henning, T.: 2001, *ApJ* **547**, 457 [29](#), [65](#), [68](#), [72](#), [79](#)
- Koch, D. G., Borucki, W., Webster, L., Dunham, E., Jenkins, J., Marriott, J., and Reitsema, H. J.: 1998, in P. Y. Bely & J. B. Breckinridge (ed.), *Society of Photo-Optical Instrumentation Engineers (SPIE) Conference Series*, Vol. 3356 of *Society of Photo-Optical Instrumentation Engineers (SPIE) Conference Series*, pp 599–607 [7](#)
- Kretke, K. A. and Lin, D. N. C.: 2007, *ApJ* **664**, L55 [6](#), [59](#)
- Lada, C. J. and Adams, F. C.: 1992, *ApJ* **393**, 278 [4](#)
- Lafrenière, D., Jayawardhana, R., and van Kerkwijk, M. H.: 2008, *ApJ* **689**, L153 [8](#)
- Laughlin, G., Steinacker, A., and Adams, F. C.: 2004, *ApJ* **608**, 489 [10](#), [39](#), [83](#)
- Leconte, J., Chabrier, G., Baraffe, I., and Levrard, B.: 2010, *A&A* **516**, A64+ [8](#)
- Léger, A., Rouan, D., Schneider, J., Barge, P., Fridlund, M., Samuel, B., Ollivier, M., Guenther, E., Deleuil, M., Deeg, H. J., Auvergne, M., Alonso, R., Aigrain, S., Alapini, A., Almenara, J. M., Baglin, A., Barbieri, M., Bruntt, H., Bordé, P., Bouchy, F., Cabrera, J., Catala, C., Carone, L., Carpano, S., Csizmadia, S., Dvorak, R., Erikson, A., Ferraz-Mello, S., Foing, B., Fressin, F., Gandolfi, D., Gillon, M., Gondoin, P., Grasset, O., Guillot, T., Hatzes, A., Hébrard, G., Jorda, L., Lammer, H., Llebaria, A., Loeillet, B., Mayor, M., Mazeh, T., Moutou, C., Pätzold, M., Pont, F., Queloz, D., Rauer, H., Renner, S., Samadi, R., Shporer, A., Sotin, C., Tingley, B., Wuchterl, G.,

## BIBLIOGRAPHY

---

- Adda, M., Agogu, P., Appourchaux, T., Ballans, H., Baron, P., Beaufort, T., Bellenger, R., Berlin, R., Bernardi, P., Blouin, D., Baudin, F., Bodin, P., Boissard, L., Boit, L., Bonneau, F., Borzeix, S., Briet, R., Buey, J.-T., Butler, B., Cailleau, D., Cautain, R., Chabaud, P.-Y., Chaintreuil, S., Chiavassa, F., Costes, V., Cuna Parrho, V., de Oliveira Fialho, F., Decaudin, M., Defise, J.-M., Djalal, S., Epstein, G., Exil, G.-E., Fauré, C., Fenouillet, T., Gaboriaud, A., Gallic, A., Gamet, P., Gavalda, P., Grolleau, E., Gruneisen, R., Gueguen, L., Guis, V., Guivarc'h, V., Guterman, P., Hallouard, D., Hasiba, J., Heuripeau, F., Huntzinger, G., Hustaix, H., Imad, C., Imbert, C., Johlander, B., Jouret, M., Journoud, P., Karioty, F., Kerjean, L., Lafaille, V., Lafond, L., Lam-Trong, T., Landiech, P., Lapeyrere, V., Larqué, T., Laudet, P., Lautier, N., Lecann, H., Lefevre, L., Leruyet, B., Levacher, P., Magnan, A., Mazy, E., Mertens, F., Mesnager, J.-M., Meunier, J.-C., Michel, J.-P., Monjoin, W., Naudet, D., Nguyen-Kim, K., Orcesi, J.-L., Ottacher, H., Perez, R., Peter, G., Plasson, P., Plessier, J.-Y., Pontet, B., Pradines, A., Quentin, C., Reynaud, J.-L., Rolland, G., Rollenhagen, F., Romagnan, R., Russ, N., Schmidt, R., Schwartz, N., Sebbag, I., Sedes, G., Smit, H., Steller, M. B., Sunter, W., Surace, C., Tello, M., Tiphène, D., Toulouse, P., Ulmer, B., Vandermarcq, O., Vergnault, E., Vuillemin, A., and Zanatta, P.: 2009, *A&A* **506**, 287 [7](#)
- Lin, C. C. and Shu, F. H.: 1966, *Proceedings of the National Academy of Science* **55**, 229 [6](#)
- Lin, D. N. C. and Papaloizou, J.: 1986, *ApJ* **309**, 846 [12](#), [18](#), [20](#)
- Lin, M.-K. and Papaloizou, J. C. B.: 2010, *MNRAS* **405**, 1473 [32](#)
- Lissauer, J. J.: 1993, *ARA&A* **31**, 129 [2](#)
- Lubow, S. H., Seibert, M., and Artymowicz, P.: 1999, *ApJ* **526**, 1001 [19](#), [65](#), [71](#)
- Lynden-Bell, D. and Pringle, J. E.: 1974, *MNRAS* **168**, 603 [18](#), [20](#)
- Lyra, W., Johansen, A., Klahr, H., and Piskunov, N.: 2008, *A&A* **479**, 883 [44](#)
- Lyttleton, R. A.: 1940, *MNRAS* **100**, 546 [2](#)
- Machida, M., Hayashi, M. R., and Matsumoto, R.: 2000, *ApJ* **532**, L67 [6](#)
- Mannings, V. and Emerson, J. P.: 1994, *MNRAS* **267**, 361 [4](#)
- Mao, S. and Paczynski, B.: 1991, *ApJ* **374**, L37 [8](#)
- Marcy, G., Butler, R. P., Fischer, D., Vogt, S., Wright, J. T., Tinney, C. G., and Jones, H. R. A.: 2005, *Progress of Theoretical Physics Supplement* **158**, 24 [7](#)

## BIBLIOGRAPHY

---

- Masset, F. S.: 2002, *A&A* **387**, 605 [6](#), [15](#), [28](#), [34](#), [38](#)
- Masset, F. S., D'Angelo, G., and Kley, W.: 2006a, *ApJ* **652**, 730 [18](#), [38](#), [50](#), [51](#), [55](#)
- Masset, F. S., Morbidelli, A., Crida, A., and Ferreira, J.: 2006b, *ApJ* **642**, 478 [6](#), [59](#)
- Masset, F. S. and Papaloizou, J. C. B.: 2003, *ApJ* **588**, 494 [10](#), [14](#), [32](#)
- Mayer, L., Quinn, T., Wadsley, J., and Stadel, J.: 2002, *Science* **298**, 1756 [5](#), [64](#)
- McCrea, W. H. and Williams, I. P.: 1965, *Royal Society of London Proceedings Series A* **287**, 143 [4](#)
- Mendoza V., E. E.: 1968, *ApJ* **151**, 977 [4](#)
- Mignone, A., Bodo, G., Massaglia, S., Matsakos, T., Tesileanu, O., Zanni, C., and Ferrari, A.: 2007, *ApJS* **170**, 228 [iii](#), [6](#), [20](#), [40](#), [66](#), [79](#)
- Miller, N., Fortney, J. J., and Jackson, B.: 2009, *ApJ* **702**, 1413 [8](#)
- Mizuno, H.: 1980, *Progress of Theoretical Physics* **64**, 544 [5](#), [64](#)
- Mordasini, C., Alibert, Y., and Benz, W.: 2009a, *A&A* **501**, 1139 [8](#), [9](#), [64](#)
- Mordasini, C., Alibert, Y., Benz, W., and Naef, D.: 2009b, *A&A* **501**, 1161 [8](#), [9](#), [18](#), [38](#), [64](#)
- Moulton, F. R.: 1905, *ApJ* **22**, 165 [2](#)
- Nagasawa, M., Ida, S., and Bessho, T.: 2008, *ApJ* **678**, 498 [7](#)
- Nelson, R. P.: 2005, *A&A* **443**, 1067 [39](#), [46](#), [54](#)
- Nelson, R. P. and Gressel, O.: 2010, *MNRAS* **409**, 639 [40](#)
- Nelson, R. P. and Papaloizou, J. C. B.: 2003, *MNRAS* **339**, 993 [10](#), [39](#), [53](#)
- Nelson, R. P. and Papaloizou, J. C. B.: 2004, *MNRAS* **350**, 849 [10](#), [39](#)
- Nelson, R. P., Papaloizou, J. C. B., Masset, F., and Kley, W.: 2000, *MNRAS* **318**, 18 [18](#), [39](#)
- Nölke, F.: 1932, *MNRAS* **93**, 159 [2](#)
- Ogihara, M., Ida, S., and Morbidelli, A.: 2007, *Icarus* **188**, 522 [40](#), [83](#)
- Ogilvie, G. I. and Lin, D. N. C.: 2004, *ApJ* **610**, 477 [8](#)

## BIBLIOGRAPHY

---

- Oishi, J. S., Mac Low, M., and Menou, K.: 2007, *ApJ* **670**, 805 [10](#), [39](#)
- Okuzumi, S.: 2009, *ApJ* **698**, 1122 [4](#)
- Paardekooper, S., Baruteau, C., Crida, A., and Kley, W.: 2010, *MNRAS* **401**, 1950 [81](#)
- Paardekooper, S. and Papaloizou, J. C. B.: 2009a, *MNRAS* **394**, 2283 [6](#), [15](#), [34](#), [50](#), [57](#)
- Paardekooper, S. and Papaloizou, J. C. B.: 2009b, *MNRAS* **394**, 2297 [15](#)
- Papaloizou, J. and Lin, D. N. C.: 1984, *ApJ* **285**, 818 [6](#), [38](#)
- Papaloizou, J. C. B. and Larwood, J. D.: 2000, *MNRAS* **315**, 823 [39](#)
- Papaloizou, J. C. B. and Nelson, R. P.: 2003, *MNRAS* **339**, 983 [10](#), [39](#)
- Papaloizou, J. C. B., Nelson, R. P., and Snellgrove, M. D.: 2004, *MNRAS* **350**, 829 [10](#), [39](#)
- Papaloizou, J. C. B. and Pringle, J. E.: 1984, *MNRAS* **208**, 721 [5](#)
- Papaloizou, J. C. B. and Pringle, J. E.: 1985, *MNRAS* **213**, 799 [5](#)
- Pepliński, A., Artymowicz, P., and Mellema, G.: 2008, *MNRAS* **386**, 179 [32](#)
- Pollack, J. B., Hubickyj, O., Bodenheimer, P., Lissauer, J. J., Podolak, M., and Greenzweig, Y.: 1996, *Icarus* **124**, 62 [5](#), [64](#)
- Pont, F., Knutson, H., Gilliland, R. L., Moutou, C., and Charbonneau, D.: 2008, *MNRAS* **385**, 109 [7](#)
- Rafikov, R. R.: 2005, *ApJ* **621**, L69 [5](#), [64](#)
- Rasio, F. A. and Ford, E. B.: 1996, *Science* **274**, 954 [7](#)
- Richardson, L. J., Deming, D., Horning, K., Seager, S., and Harrington, J.: 2007, *Nature* **445**, 892 [7](#)
- Sano, T., Inutsuka, S.-i., Turner, N. J., and Stone, J. M.: 2004, *ApJ* **605**, 321 [6](#)
- Sano, T., Miyama, S. M., Umebayashi, T., and Nakano, T.: 2000, *ApJ* **543**, 486 [6](#)
- Santos, N. C., Israelian, G., Mayor, M., Rebolo, R., and Udry, S.: 2003, *A&A* **398**, 363 [7](#)
- Schräpler, R. and Henning, T.: 2004, *ApJ* **614**, 960 [4](#), [5](#)
- Shakura, N. I. and Sunyaev, R. A.: 1973, *A&A* **24**, 337 [69](#)

## BIBLIOGRAPHY

---

- Sharma, P., Hammett, G. W., Quataert, E., and Stone, J. M.: 2006, *ApJ* **637**, 952 [6](#)
- Shen, Y. and Turner, E. L.: 2008, *ApJ* **685**, 553 [7](#)
- Shu, F. H.: 1970, *ApJ* **160**, 99 [6](#)
- Sicilia-Aguilar, A., Hartmann, L. W., Watson, D., Bohac, C., Henning, T., and Bouwman, J.: 2007, *ApJ* **659**, 1637 [4](#)
- Spitzer, Jr., L.: 1939, *ApJ* **90**, 675 [2](#)
- Stevenson, D. J.: 1982, *Planet. Space Sci.* **30**, 755 [5](#), [64](#)
- Stone, J. M., Gardiner, T. A., Teuben, P., Hawley, J. F., and Simon, J. B.: 2008, *ApJS* **178**, 137 [6](#)
- Stone, J. M., Hawley, J. F., Gammie, C. F., and Balbus, S. A.: 1996, *ApJ* **463**, 656 [6](#)
- Stone, J. M. and Norman, M. L.: 1992, *ApJS* **80**, 753 [6](#)
- Stone, J. M. and Pringle, J. E.: 2001, *MNRAS* **322**, 461 [6](#)
- Syer, D. and Clarke, C. J.: 1995, *MNRAS* **277**, 758 [19](#)
- Tanaka, H., Takeuchi, T., and Ward, W. R.: 2002, *ApJ* **565**, 1257 [6](#), [12](#), [13](#), [38](#), [50](#)
- Tanigawa, T. and Watanabe, S.-i.: 2002, *ApJ* **580**, 506 [28](#), [65](#), [68](#), [71](#), [73](#), [74](#)
- Ter Haar, D.: 1948, *Science* **107**, 405 [3](#)
- Ter Haar, D.: 1950, *ApJ* **111**, 179 [3](#)
- Ter Haar, D.: 1967, *ARA&A* **5**, 267 [2](#)
- Terebey, S., Shu, F. H., and Cassen, P.: 1984, *ApJ* **286**, 529 [4](#)
- Terquem, C. E. J. M. L. J.: 2003, *MNRAS* **341**, 1157 [38](#), [50](#)
- Thalmann, C., Carson, J., Janson, M., Goto, M., McElwain, M., Egner, S., Feldt, M., Hashimoto, J., Hayano, Y., Henning, T., Hodapp, K. W., Kandori, R., Klahr, H., Kudo, T., Kusakabe, N., Mordasini, C., Morino, J.-I., Suto, H., Suzuki, R., and Tamura, M.: 2009, *ApJ* **707**, L123 [8](#)
- Thommes, E. W. and Murray, N.: 2006, *ApJ* **644**, 1214 [6](#), [38](#)
- Throop, H. B., Bally, J., Esposito, L. W., and McCaughrean, M. J.: 2001, *Science* **292**, 1686 [4](#)

- Trilling, D. E., Lunine, J. I., and Benz, W.: 2002, *A&A* **394**, 241 [38](#)
- Turner, N. J., Carballido, A., and Sano, T.: 2010, *ApJ* **708**, 188 [6](#)
- Turner, N. J. and Sano, T.: 2008, *ApJ* **679**, L131 [6](#)
- Turner, N. J., Sano, T., and Dziourkevitch, N.: 2007, *ApJ* **659**, 729 [6](#)
- Udry, S., Mayor, M., and Santos, N. C.: 2003, *A&A* **407**, 369 [7](#)
- Udry, S. and Santos, N. C.: 2007, *ARA&A* **45**, 397 [7](#)
- Uribe, A. L., Klahr, H., Flock, M., and Henning, T.: 2011, *ApJ* **736**, 85 [37](#), [70](#)
- Vauclair, S.: 2004, *ApJ* **605**, 874 [7](#)
- Veras, D., Crepp, J. R., and Ford, E. B.: 2009, *ApJ* **696**, 1600 [8](#)
- Ward, W. R.: 1986, *Icarus* **67**, 164 [38](#)
- Ward, W. R.: 1992, in S. F. Dermott, J. H. Hunter Jr., & R. E. Wilson (ed.), *Astrophysical Disks*, Vol. 675 of *Annals of the New York Academy of Sciences*, pp 314–323 [39](#)
- Ward, W. R.: 1997, *Icarus* **126**, 261 [6](#), [12](#), [18](#), [38](#)
- Wardle, M.: 1999, *MNRAS* **307**, 849 [6](#)
- Weidenschilling, S. J.: 1984, *Icarus* **60**, 553 [4](#)
- Wetherill, G. W.: 1980, *ARA&A* **18**, 77 [5](#)
- Williams, I. P. and Cremin, A. W.: 1968, *QJRAS* **9**, 40 [2](#)
- Williams, J. P. and Cieza, L. A.: 2011, *ArXiv e-prints* [4](#)
- Winters, W. F., Balbus, S. A., and Hawley, J. F.: 2003, *ApJ* **589**, 543 [39](#), [53](#)
- Yang, C., Mac Low, M., and Menou, K.: 2009, *ApJ* **707**, 1233 [39](#)
- Youdin, A. N. and Shu, F. H.: 2002, *ApJ* **580**, 494 [5](#)
- Zsom, A., Ormel, C. W., Güttler, C., Blum, J., and Dullemond, C. P.: 2010, *A&A* **513**, A57+ [4](#)

## Acknowledgements

### Agradecimientos

Quiero agradecerle a mis amigos por mantenerme cuerda durante estos tres años. Gracias a Maxito por ser como eres, a Paolilla por ser tan loquita, y a Carolina y Ulrich por ser tan hermosos. Gracias a mis amigos que estuvieron lejos pero siempre en mi mente, Peter y Olga. A las personas con las que compartí muchos buenos momentos durante este tiempo; Juan, Camila, Julio, Natasha, Sareh, Somayeh, Dading, Matucci, Lavinia, Leonard. En especial, le agradezco a mi amigo Mauricio por los infinitos cafés, las sesiones de quejas y de nostalgia, por hacerme reír y sacarme la piedra de vez en cuando. Estos tres años no hubieran sido lo mismo sin él en Heidelberg.

Un agradecimiento especial a Mario por toda su ayuda al comienzo (y en la mitad, y al final) del proyecto, fue muy bacano poder trabajar con él. También le quiero agradecer a mis supervisores, Hubert y Thomas, por todo su apoyo, discusiones y consejos. Le agradezco a Hubert por su amabilidad constante y por todas sus ideas y sugerencias que siempre mejoraron mi trabajo.

Mis queridos padres son los que han hecho posible que yo tenga esta oportunidad en primer lugar. Gracias a mi mamá por siempre estar ahí para mí y por no dejarme olvidar todo lo que siempre estará ahí para mí. Gracias a mi papá por su apoyo, su generosidad y sus locuras. Le agradezco también a mi querida hermana Luisa, por sus correos de apoyo y de distracción :P.

Finalmente, mis últimas gracias son para Joe, el mejor descubrimiento que pude haber hecho en este tiempo. Gracias por caminar este camino al lado mío, por ser una persona tan increíble y por hacerme feliz. Los momentos que compartí contigo (y con Harper) durante este tiempo estarán siempre en mi corazón.

#### *English Version*

I would like to thank my friends for keeping me sane during these three years. Thanks to Maxito for being how you are, to Paolilla for being a crazy girl, and to Carolina and Ulrich for being so beautiful people. Thanks to my friends who were far away but were always on my mind, Peter and Olga. To the people

who shared this years with me at some point and with whom I spent many good times; Juan, Camila, Julio, Natasha, Sareh, Somayeh, Dading, Matucci, Lavinia, Leonard. Specially, I want to thank my friend Mauricio for the infinite coffees, the complaining and nostalgia sessions, for always making me laugh and very mad sometimes. These three years would not have been the same without him in Heidelberg.

A special thanks to Mario for all his help in the early (and not so early) days of the project, it was great to get to work with you. I also want to thank my supervisors, Hubert and Thomas, for all their support, discussions and advice. I thank Hubert for his constant kindness and for all his suggestions and ideas that always improved my work.

My dear parents have made it possible for me to be here in the first place. Thanks to my mom for being always there for me and for not letting me forget all that was always there for me. Thanks to my dad for his constant support, his generosity and his craziness. Thanks to my dear sister Luisa for her support and distraction emails :P.

Finally, my last thanks are for Joe, the best discovery I could have made in this time. Thank you for walking this path next to me, for being so wonderful and for making me happy. The moments I spent with you (and Harper) during this time will be forever in my heart.

## Declaration

I herewith declare that I have produced this paper without the prohibited assistance of third parties and without making use of aids other than those specified; notions taken over directly or indirectly from other sources have been identified as such. This paper has not previously been presented in identical or similar form to any other German or foreign examination board.

The thesis work was conducted from 2008 to 2011 under the supervision of Dr. Hubert Klahr and Prof. Dr. Thomas Henning at Max-Planck-Institute for Astronomy (MPIA).

Heidelberg, November 21, 2011.